UNIVERSIDADE ESTADUAL PAULISTA
"JÚLIO DE MESQUITA FILHO"
Câmpus Bauru

Leonardo Francisco Gonçalves Dias

Immobilization of bisphosphonates on nanostructured films of TiO_2 and hydroxyapatite

Bauru
2022

Leonardo Francisco Gonçalves Dias

Immobilization of bisphosphonates on nanostructured films of TiO_2 and hydroxyapatite

Tese apresentada como requisito à obtenção do título de Doutor à Universidade Estadual Paulista "Júlio de Mesquita Filho" – Programa de Pós-graduação em Ciência e Tecnologia de Materiais, sob orientação do Prof. Dr. Paulo Noronha Lisboa-Filho

Financiadora: FAPESP - Proc. 2018/07520-3

Orientador: Prof. Dr. Paulo Noronha Lisboa-Filho

Coorientadora: Drª. Erika Soares Bronze-Uhle

Faculdade de Ciências

Bauru
2022

Dias, Leonardo Francisco Gonçalves.
Immobilization of bisphosphonates on nanostructured films of TiO_2 and hydroxyapatite / Leonardo Francisco Gonçalves Dias. – Bauru, 2022
135 f. : il., tabs.

Supervisor: Prof. Dr. Paulo Noronha Lisboa-Filho
Tese (doutorado) - Universidade Estadual Paulista “Júlio de Mesquita Filho", Faculdade de Ciências.

1. bisphosphonates. 2. titanium dioxide. 3. hydroxyapatite. I. Lisboa-Filho, Paulo Noronha II. Universidade Estadual Paulista “Júlio de Mesquita Filho", Faculdade de Ciências. III. Título.

CDU – 518.72:76

Leonardo Francisco Gonçalves Dias

Immobilization of bisphosphonates on nanostructured films of TiO_2 and hydroxyapatite

Tese apresentada como requisito à obtenção do título de Doutor à Universidade Estadual Paulista "Júlio de Mesquita Filho" – Programa de Pós-graduação em Ciência e Tecnologia de Materiais, sob orientação do Prof. Dr. Paulo Noronha Lisboa-Filho

Financiadora: FAPESP - Proc. 2018/07520-3

Bauru
31 de outubro de 2022

UNIVERSIDADE ESTADUAL PAULISTA

Câmpus de Bauru

Faculdade de Ciências

ATA DA DEFESA PÚBLICA DA TESE DE DOUTORADO DE LEONARDO FRANCISCO GONÇALVES DIAS, DISCENTE DO PROGRAMA DE PÓS-GRADUAÇÃO EM CIÊNCIA E TECNOLOGIA DE MATERIAIS, DA FACULDADE DE CIÊNCIAS - CÂMPUS DE BAURU.

Aos 18 dias do mês de novembro do ano de 2022, às 14:00 horas, no(a) Anfiteatro do Departamento de Química - FC/Bauru, realizou-se a defesa de TESE DE DOUTORADO de LEONARDO FRANCISCO GONÇALVES DIAS, intitulada **Immobilization of bisphosphonates on nanostructured films of TiO2 and hydroxyapatite**. A Comissão Examinadora foi constituida pelos seguintes membros: Prof. Dr. PAULO NORONHA LISBOA FILHO (Orientador(a) - Participação Presencial) do(a) Departamento de Fisica / Faculdade de Ciencias de Bauru/ UNESP, Prof. Dr. UBIRAJARA PEREIRA RODRIGUES FILHO (Participação Presencial) do(a) Departamento de Química e Física Molecular / Instituto de Química - USP - São Carlos, Prof. Dr. ABNER DE SIERVO (Participação Presencial) do(a) Instituto de Física / UNIVERSIDADE ESTADUAL DE CAMPINAS, Profª Drª ANA PAULA RAMOS (Participação Presencial) do(a) Departamento de Química / Faculdade de Filosofia, Ciências e Letras de Ribeirão Preto da Universidade de São Paulo - FFCLRP, Prof. Dr. NILSON CRISTINO DA CRUZ (Participação Virtual) do(a) Curso de Engenharia de Controle e Automação / Instituto de Ciência e Tecnologia/ UNESP/ Sorocaba. Após a exposição pelo doutorando e arguição pelos membros da Comissão Examinadora que participaram do ato, de forma presencial e/ou virtual, o discente recebeu o conceito final: APROVADO. Nada mais havendo, foi lavrada a presente ata, que após lida e aprovada, foi assinada pelo(a) Presidente(a) da Comissão Examinadora.

Prof. Dr. PAULO NORONHA LISBOA FILHO

Dedico este trabalho aos meus pais Israel e Valda, minha esposa Marina e minha filha Mariana.

Agradecimentos

Gostaria de agradecer à minha companheira e esposa Marina, a pessoa que esteve mais próxima de mim durante toda essa caminhanda. Aos momentos de conversa, carinho e acolhimento que você sempre proporcionou. Ao seu lado sinto que sou capaz de fazer tudo.

Aos meus pais, Israel e Valda por desde sempre me apoairem a seguir os meus sonhos, mesmo as vezes não os entendendo completamente. O apoio de vocês não só para este trabalho, mas para tudo o que fiz e farei é fundamental para mim.

À minha filha Mariana, que com seu jeito doce e empático de ver a vida sempre fez com que eu me sentisse especial.

À minha amiga Maithe por sempre acreditar nas minhas capacidades.

À minha terapeuta Bárbara Campos pelu auxílio fundamental nessa jornada.

Aos meus orientadores Prof. Dr. Paulo Noronha e Drª. Erika Soares pelos ensinamentos não só sobre ciência de materiais como também sobre a vida e vinhos, além dos incontáveis cafés. Vocês sempre me apoiaram, mesmo na época em que eu era apenas um calouro na universidade e me acolheram com muito carinho nos momentos de dificuldade.

Aos meus amigos de laboratório pelas conversas e apoio.

Por último, mas não menos importante aos técnicos e servidores da universidade. Ao programa de pós-graduação em ciência e tecnologia de materiais, a Coordenação de Aperfeiçoamento de Pessoal de Nível Superior (CAPES), a Fundação de Amparo à Pesquisa do Estado de São Paulo - FAPESP pelo financiamento através dos projetos 2018/07520-3 e 2019/13100-0.

Pouca saúde, muita saúva, os males do Brasil são.

*(*Macunaíma - *Mário de Andrade)*

Abstract

Bisphosphonates are a class of organic molecules used for bone growth, however, the prolonged use of these molecules is related to mandibular osteonecrosis. To maintain the ability to promote bone growth, the immobilization of these molecules on the surface of implants is an alternative to increasing the biocompatibility of implants without presenting the side effects of prolonged exposu re. This thesis aims to collaborate with data and discussions of bisphosphonates immobilized on TiO_2 surfaces of hydroxyapatite (HA), based mainly on measurements of X-ray photoelectron spectroscopy, zeta potential, and atomic force microscopy. First, layers of octadecylphosphonic acid on TiO_2 obtained by sputtering were investigated, then bisphosphonates on different surfaces, such as TiO_2 by sol-gel and hydroxyapatite. Data obtained from computer simulation were used and discussed together with the experimental data. The results indicate that bisphosphonates adsorb on the surface exposing the phosphonate groups, and promoting a hydrophilic surface. Furthermore, changes in pH alter the surface charge due to the presence of P-OH and -N^+ species. On titanium dioxide surfaces, adsorption can be enhanced by the hydroxylation process, as shown in the adsorption curves of bisphosphonates. No cytotoxic effec was observed on prepared samples. The applied strategy is a suitable strategy for the investigation of bioactive molecules and can be used as a basis for other compounds.

Keywords: bisphosphonate, titanium dioxide, hydroxyapatite, surface characterization.

Resumo

Os bisfosfonatos são uma classe de moléculas orgânicas utilizadas para o crescimento ósseo, porém, o uso prolongado desses dessas moléculas está relacionado à osteonecrose mandibular. Para manter a capacidade de promover o crescimento ósseo, a imobilização dessas moléculas na superfície dos implantes é uma alternativa para aumentar a biocompatibilidade dos implantes sem apresentar os efeitos colaterais da exposição prolongada a essas moléculas. Esta tese visa colaborar com dados e discussões de bifosfonatos imobilizados em superfícies de TiO_2 de hidroxiapatita (HA), com base principalmente em medidas de espectroscopia de fotoelétrons excitados por raios X, potencial zeta e microscopia de força atômica. Primeiramente, foram investigadas camadas de ácido octadecilfosfônico sobre TiO_2 obtidas por *sputtering*, depois bifosfonatos em diferentes superfícies, como TiO_2 por sol-gel e hidroxiapatita. Os dados obtidos a partir de simulação computacional foram utilizados e discutidos juntamente com os dados experimentais. Os resultados indicam que os bisfosfonatos adsorvem na superfície expondo os grupos fosfonatos e promovendo uma superfície hidrofílica. Além disso, mudanças no pH alteram a carga superficial devido à presença de espécies P-OH e $-N^+$. Em superfícies de dióxido de titânio, a adsorção pode ser potencializada pelo processo de hidroxilação, como mostrado nas curvas de adsorção dos bifosfonatos. Nenhum efeito citotóxico foi observado nas amostras preparadas. A estratégia aplicada é se mostrou adequada para a investigação de moléculas bioativas e pode ser utilizada como base para outros compostos.

Palavras-chaves: bisfosfonato, dióxido de titânio, hidroxiapatita, caracterização de superfícies.

Resumo expandido

O tecido ósseo é um dos principais componentes do esqueleto humano. Entre as suas funções, destacam-se a proteção dos órgãos vitais, suporte para os músculos, além de ser um reservatório de íons de cálcio e fósforo. A manutenção adequada desse tecido depende do equilíbrio da atividade de células chamadas osteoblastos e osteoclastos. Os osteoblastos estão diretamente relacionados com crescimento e renovação óssea, enquanto os osteoclastos são responsáveis por reabsorver o tecido ósseo. Um desequilíbrio da atividade dessas células pode resultar em perda óssea, característica comum da osteoporose. Outro fator que pode causar um desequilíbrio são traumas causados em acidentes de trânsito, por exemplo. Em alguns casos é necessária a substituição total ou parcial de alguns ossos, que em geral são substituídos por implantes metálicos, compostos principalmente por titânio.

Ao ser colocado dentro do organismo, um implante sofre uma reação de corpo estranho que em casos graves pode levar a sua rejeição completa, sendo necessário novos procedimentos cirúrgicos. Com o objetivo de reduzir as falhas dos implantes e/ou acelerar a integração entre o tecido vivo e o implante, pesquisadores têm se dedicado a modificar a superfície desses materiais para atingir esse objetivo.

Dentre as modificações de superfície destacam-se a deposição de filmes finos e a funcionalização. A primeira opção consiste na deposição de finas camadas de outros materiais como por exemplo o dióxido de titânio, hidroxiapatita e compósitos dos dois materiais. O TiO_2 devido à presença de hidroxilas em sua superfície favorece adsorção de proteínas que auxiliam no processo de integração tecido-implante. A hidroxiapatita, devido a sua presença no tecido ósseo é um dos recobrimentos que maior favorece a biocompatibilidade, entretanto possui uma baixa adesão em superfícies metálicas. O compósito dos dois materiais alia a biocompatibilidade com adesão implante-filme. O segundo processo, chamado funcionalização consiste na adição de grupos funcionais sobre a superfícies. Dentre as moléculas utilizadas para isso destacam-se os bisfosfonatos.

Bisfosfonatos são uma família de moléculas orgânicas análogos ao pirofosfato, inibidores de mineralização, que são utilizadas principalmente para o tratamento de problemas ósseos como osteoporose e doença de Paget, promovendo principalmente um crescimento ósseo além da diminuição da atividade dos osteoclastos. Entretanto, o uso contínuo desse composto está associado a osteonecrose mandibular. Dessa forma o uso dessas moléculas como modificadores de superfície, pode aliar a capacidade de crescimento ósseo reduzindo os efeitos indesejados.

Diante disso, a presente tese tem como objetivo contribuir com dados e discussões sobre su-

perfícies de TiO_2, HA e TiO_2+HA, recobertas com bisfosfonatos, especificamente etidronato, alendronato e risedronato. Para isso técnicas como espectroscopia de fotoelétrons de raio-X foram amplamente utilizadas, bem como potencial zeta, ângulo de contato e microscopia de força atômica. Os resultados deste trabalho foram apresentados em quatro capítulos em formato de artigos.

A primeira publicação intitulada "*New details of assembling bioactive films from dispersions of amphiphilic molecules on titania surfaces*", consiste na intestigação de filmes finos de um silano e um fosfonato, respectivamente, cloreto de dimetiloctadecil (3-trimetoxissililpropil) amônio (DMOAP) e ácido octadecilfosfônico (ODPA), sobre dióxido de titânio. As investigações mostraram uma relação entre a estrutura dos filmes e a atividade bactericida, especialmente para o DMOAP. Os resultados de potencial zeta juntamente com espectroscopia de fotoelétrons de raio-X demostraram que as mudanças na carga superficial de filmes de ODPA ocorre devido à presença de grupos P-OH não ligados. Os resultados obtidos, principalmente para as monocamadas de ODPA servem como base para a interpretação e discussão de dados envolvendo bisfosfonatos.

A segunda publicação nomeada "*Bisphosphonates on smooth TiO_2: modeling and characterization*", utiliza principalmente dados de simulação computacional, potencial zeta e espectroscopia de fotoelétrons de raio-X para discutir as características físico-químicas de filmes de etidronato, alendronato e risedronato sobre dióxido de titânio. Os resultados demonstram mais uma vez a influência de grupos P-OH na superfície, bem como do alendronato e risedronato, que contêm nitrogênio. Além disso, artigo indica que os bisfosfonatos adsorvem na superfície através da condensação das hidroxilas do TiO_2 e dos grupos P-OH, formando ligações do tipo Ti-O-P. Bisfosfonatos que contêm nitrogênio apresentam ligações de hidrogênio entre as hidroxilas e os grupos nitrogenados.

A terceira publicação, "*Adsorption and X-ray photoelectron spectroscopy investigation of bisphosphonates on titania and hydroxyapatite surfaces*", apresenta a curva de adsorção dos bisfosfonatos em TiO_2 junto com uma investigação da adsorção dessas moléculas em TiO_2, hidroxiapatita e superfícies mistas. Os resultados mostraram que a hidroxilação do TiO_2 aumenta a quantidade de bisfosfonato adsorvida, esse efeito foi atribuído a um aumento da deprotonação das moléculas causas pelos grupos OH terminais. Os resultados de espectroscopia de fotoelétrons de raios-X mostram uma adsorção competitiva entre os bisfosfonatos e grupos carboxilas, que é menor em superfícies contendo hidroxiapatita. Por fim observou-se que as moléculas adsorvem no TiO_2 seguindo a topografia da superfíce enquanto na hidroxiapatita os bisfosfonatos acumulam ao redor dos íons de cálcio, isso se reflete em um aumento da rugosidade apenas para a superfície de hidroxiapatita.

O Capítulo 6 apresenta os resultados microbiológicos obtidos até a conclusão dessa tese. Os resultados indicam uma tendência de superfícies contendo risedronato em limitar o crescimento de *S. aureus*, essa tendência foi associada a um efeito sinergético entre a camada adsorvida e a rugosidade do material. Por fim, não foram observados efeitos citotóxicos em células mesenquimais ósseas humanas.

As publicações apresentadas estão de acordo com os objetivos propostos nessa tese. A estratégia proposta mostrou-se eficaz para evidenciar os aspectos da adsorção dos bisfosfonatos, bem como as propriedades de suas camadas. A estratégia aqui apresentada pode ser aplicada em outras moléculas bioativas.

Palavras-chaves: bisfosfonato, dióxido de titânio, hidroxiapatita, caracterização de superfícies.

List of Figures

Figure 1 – Schematic representation of mineralization in bone matrix 23
Figure 2 – Synthesis mechanism of titanium dioxide by sol-gel route using titanium isopropoxide as precursor. 25
Figure 3 – a) General structure of bisphosphonates, b) etidronate, c) alendronate and d) risedronate linear structure. 26
Figure 4 – Effects of BPs on bone metabolism. A) Transformation of non-N-BPs into cytotoxic ATP analogs prompts osteoclast apoptosis, while N-BPs induce osteoclast apoptosis by inhibiting FPPS. B) BPs modulate the expression of osteoclast-related genes and promote the expression of osteogenicrelated genes. C) BPs restrain BMSC adipogenic differentiation and promote their osteogenic differentiation. D) BPs inhibit apoptosis of osteoblasts and osteocytes. 28
Figure 5 – Linear structure of (a) DMOAP and (b) ODPA. 33
Figure 6 – XPS high resolution spectra for investigated bulk sample ODPA, (a) C1s, (b) O1s and (c) P2p signal. 42
Figure 7 – XPS C1s high-resolution spectra for DMOAP, (a) bulk, (b) water exposed, and (c) heated blot 44
Figure 8 – XPS high-resolution spectra for sputtered titanium dioxide, (a) Ti2p, (b) O1s, (c) C1s and (d) N1s signal. 46
Figure 9 – High-resolution C1s and O1s XPS spectra obtained for ODPA layers on titania after immersion in ODPA solution for 4 h (a) and (c); 24 h (b) and (d). 47
Figure 10 – XPS high-resolution spectra for DMOAP layer on titania, (a) C1s, (b) O1s, (c) N1s and (d) Si2p signals. 50
Figure 11 – Zeta potential results for the studied layers on smooth titanium dioxide. . 54
Figure 12 – AFM height and adhesion force image for the investigated layers. 55
Figure 13 – AFM height profile of (a) sputtered titanium dioxide and (b) ODPA monolayer. 56
Figure 14 – *S. mutans* growth after exposition to different samples during three different periods. 57
Figure 15 – a) General structure of bisphosphonic acids and linear structure of b) etidronic acid, c) alendronic acid and d) risedronic acid. 61
Figure 16 – Structure, Fukui indices, and map of electrostatic potential (MEP) of studied molecules when dissolved in water. The number of asterisks (*) in each molecule is used to indicate the scale of the map of the electrostatic potential, because the protonated/deprotonated states of the molecule are unbalance in the charge. 64

Figure 17 – C1s, O1s, and N1s high-resolution spectra for sputtered-deposited titania; C1s high-resolution spectra of etidronic acid (ETI), alendronic acid (ALE), and risedronic acid (RIS) layers adsorbed on titania. 66
Figure 18 – O1s and N1s XPS signals for etidronic acid (ETI), alendronic acid (ALE), and risedronic (RIS) adsorbed on titania. 68
Figure 19 – Representation of I) etidronic acid, II) alendronic acid, and III) risedronic acid molecules adsorbed on titania surface. Hidrogen atoms are represented in white, carbon in grey, oxygen in red, nitrogen in blue, and phosphorous in yellow. 70
Figure 20 – Zeta potential measurements of bisphosphonates adsorbed on TiO_2. . . 72
Figure 21 – AFM images of bisphosphonates adsorbed on smooth titania. 73
Figure 22 – Linear structures of BPs, etidronate, alendronate, and risedronate. . . . 76
Figure 23 – Adsorption curves of BP adsorbed on titania particles. Dotted lines represent theoretical curves. 81
Figure 24 – XRD patterns of dried dispersions. 82
Figure 25 – SEM images of prepared samples. 83
Figure 26 – C 1s high-resolution XPS spectra of prepared films. BP (4 mM) was employed for functionalization. 86
Figure 27 – O 1s high-resolution XPS spectra of prepared films. BP (4 mM) was employed for functionalization. 87
Figure 28 – AFM images of prepared samples. BP (4 mM) was used for functionalization. 88
Figure 29 – *In vitro* antibacterial activity of bisphosphonate-based coatings. (A) Schematic representation of *Staphylococcus aureus* biofilm model used (B) Colony-forming units count (Log10 CFU/mL) of *S. aureus* after 24 h of biofilm formation. (b') Percentage of bacterial reduction (%) of treated surfaces to control. Data are expressed as mean ± standard deviation. Statistically, significant differences are indicated as *p < 0.05 (HSD Tukey and Bonferroni t-test). 94
Figure 30 – Determination of the minimum inhibitory concentration of risedronate. (A) MIC of risedronate from 1 mg/mL to 0.001 mg/mL. (B) Agar diffusion test with *S. aureus*. NS = no statistically significant differences among the groups. 95
Figure 31 – MTT assay. Absorbance is expressed as a measure of cell metabolism for hBMSC cells cultured on control and bisphosphonate-based coatings for each deposition process (different colors) in 3 (A) and 7 (B) days of culture. *p < 0.05 (HSD Tukey and Bonferroni t-test). 95
Figure 32 – High-resolution spectra a) Si 2p and b) P 2p for investigated bulk ODPA on a silicon wafer 119

Figure 33 – O 1s, N 1s, Si 2p and Cl 2p high-resolution spectra for the investigated bulk DMOAP samples 120
Figure 34 – C1s and O1s high-resolution spectra for octadecylphosphonic acid adsorbed on titanium dioxide. 121
Figure 35 – P2p high-resolution spectra for octadecylphosphonic acid adsorbed on titanium dioxide. 122
Figure 36 – Si 2p high-resolution spectra for DMOAP adsorbed on titania. Where "A" represent addition of aqueous HCl on the solution and "N" is the solution without the addition of HCl. 123
Figure 37 – MODA plot of the computational methods employed. 125
Figure 38 – Characterization data (CHADA) documentation was applied for XPS measurements. 127
Figure 39 – Structure, f^+, f^- and the MEP of all the structures simulated in vacuum. . 128
Figure 40 – Structure, f^+, f^- and the MEP of all the structures simulated in aqueous medium. 129
Figure 41 – C 1s high-resolution spectra of bulk etidronate. 130
Figure 42 – XRD of TiO_2 particles. 131
Figure 43 – Confocal images of prepared samples. 132
Figure 44 – Map of chemical composition of TiO_2 film. 132
Figure 45 – Map of chemical composition of TiO_2:HA 1:1 film. 133
Figure 46 – Map of chemical composition of TiO_2:HA 1:2 film. 134
Figure 47 – Map of chemical composition of HA film. 135
Figure 48 – N 1s high-resolution spectra of samples containing nitrogen. 135

List of Tables

Table 1 – Parameters of immersion, drying method, and sample name for DMOAP/titania films prepared from two different DMOAP solutions: DMOAP-N (without acid addition) and DMOAP-A (with acid addition) 38
Table 2 – Comparison between expected for homogeneous solid ODPA and obtained values from the XPS-based evaluations of atomic concentration 42
Table 3 – Ratios between the atomic concentrations of carbon [C], phosphorous [P], and oxygen [O] species, as expected from stoichiometry and found in XPS investigations 42
Table 4 – Atomic concentration in at% of the distinct surface species by XPS investigations, compared to stoichiometrically expected values. 43
Table 5 – Concentration ratios obtained from fitting C1s signals of DMOAP bulk samples prepared following different processes. 44
Table 6 – Normalized XPS signal intensity ratios for ODPA samples adsorbed on titania, based on the sample immersed for 24 h in ethanolic ODPA solution and then rinsed with ethanol (subsequently labelled “SAM”), and estimated layer thickness 48
Table 7 – Atomic concentration in at% of the distinct surface species from XPS investigations of DMOAP/titania films 49
Table 8 – Normalized atomic concentration ratios for freshly prepared DMOAP films on titania surfaces as obtained by XPS and referencing the findings for the DMOAP-N/titania films obtained after 24 h immersion (labelled “DMOAP-N 24 h” here) 51
Table 9 – Contact angle results for DMOAP and ODPA films on smooth titania (freshly prepared 52
Table 10 – Mean (SD) findings of *E. coli* growth attached to sample surface in 24 h^{a} . 58
Table 11 – Changes of water contact angles obtained for thick and thin DMOAP films on titania substrates and for ODPA/titania after 24 h exposure to bacterial medium containing *S. mutans* and subsequent rinsing with alcohol 58
Table 12 – Normalized XPS signal intensity ratios for bisphosphonate samples adsorbed on TiO_2, based on an octadecylphosphonic acid monolayer (ODPA SAM) previously published. 69
Table 13 – Water contact angle (WCA) for the studied layers. 70
Table 14 – BET measurements of prepared samples. 80
Table 15 – Freundlich adsorption parameters obtained from experimental data. . . . 80
Table 16 – Mean surface roughness of prepared samples. 83
Table 17 – Elements in atomic% measured by EDS. 83

Table 18 – Water contact angle (WCA) for pristine and samples prepared with 4 mM BP solutions. 84
Table 19 – Surface elementary composition from XPS measurements. 85
Table 20 – FWHM for the contributions of XPS analyses. 130
Table 21 – Water contact angle (WCA) for samples functionalized with 0.2 mM solutions 132

List of abbreviations and acronyms

pH	potential of hydrogen
TiO_2	titanium dioxide
HA	hydroxyapatite
BPs	bisphosphonates
BP	bisphosphonate
ATP	adenosine triphosphate
XPS	X-ray photoelectron spectroscopy
AFM	atomic force microscopy
ICP-MS	inductively coupled plasma-mass spectroscopy
DFT	density functional theory
QACs	quaternary ammonium compounds
DMOAP	dimethyloctadecyl (3-trimethoxysilylpropyl) ammoniumchloride
ODPA	octadecylphosphonic acid
AMC	antimicrobial coatings
SAMs	self-assembled monolayers
CAS	chemical abstracts service
sccm	standard cubic centimeter per minute
HPLC	high performance liquid chromatography
ETI	etidronate
ALE	alendronate
RIS	risedronate

Contents

1 INTRODUCTION 22

2 GENERAL AND SPECIFIC GOALS 31

3 NEW DETAILS OF ASSEMBLING BIOACTIVE FILMS FROM DISPERSIONS OF AMPHIPHILIC MOLECULES ON TITANIA SURFACES . . . 32

3.1 Introduction 32

3.2 Materials and methods 36

3.2.1 Materials 36

3.2.2 Preparation of bulk DMOAP and ODPA for XPS investigation 36

3.2.3 Surface preparation – film deposition 36

3.2.4 Solution preparation 37

3.2.5 Layer formation on TiO_2 37

3.2.6 DMOAP adsorption 37

3.2.7 ODPA adsorption 37

3.2.8 Atomic force microscopy 38

3.2.9 Contact angle measurements 38

3.2.10 XPS characterization 39

3.2.11 Zeta potential measurements 40

3.2.12 Antibacterial assays 40

3.3 Results and discussion 41

3.3.1 XPS characterization 41

3.3.1.1 Bulk sample 41

3.3.1.2 Adsorbed layers on smooth titania substrates 45

3.3.1.2.1 ODPA/titania films 46

3.3.1.2.2 DMOAP/titania films 49

3.3.1.2.3 Comparing ODPA/titania DMOAP/titania films 51

3.3.2 Contact angle measurements 51

3.3.3 Zeta potential measurements 53

3.3.4 AFM investigations 53

3.3.5 Antibacterial assays 56

3.4 Conclusions 59

3.5 Conflicts of interest 60

3.6 Acknowledgements 60

4 BISPHOSPHONATES ON SMOOTH TIO_2: MODELING AND CHARACTERIZATION . . . 61
4.1 Introduction . . . 61
4.2 Results and discussion . . . 63
4.2.1 Theoretical modeling . . . 63
4.2.2 XPS characterization . . . 65
4.2.3 Contact angle . . . 69
4.2.4 Zeta potential measurements . . . 71
4.2.5 Atomic force microscopy . . . 72
4.3 Conclusion . . . 73
4.4 Supporting Information Summary . . . 74
4.5 Acknowledgments . . . 74

5 ADSORPTION AND X-RAY PHOTOELECTRON SPECTROSCOPY INVESTIGATION OF BISPHOSPHONATES ON TITANIA AND HYDROXYAPATITE SURFACES . . . 75
5.1 Introduction . . . 75
5.2 Materials and methods . . . 76
5.2.1 Materials . . . 76
5.2.2 Synthesis of TiO_2 solution, HA, and TiO_2 particles . . . 77
5.2.3 Preparation of Ti substrates and film deposition . . . 77
5.2.4 BP adsorption . . . 78
5.2.5 Characterizations . . . 78
5.3 Results and discussion . . . 79
5.3.1 Effects of BP adsorption on TiO_2 particles . . . 80
5.3.2 Structures and morphologies of prepared films . . . 81
5.3.3 Effects of BPs adsorption on TiO_2, HA, and TiO_2+HA films . . . 83
5.4 Conclusions . . . 88
5.5 Acknowledgments . . . 89

6 MICROBIOLOGICAL ACTIVITY OF BISPHOSPHONATES ON TITANIA, HYDROXYAPATITE AND COMPOSITE SURFACES . . . 90
6.1 Introduction . . . 90
6.2 Materials an methods . . . 91
6.2.1 Antibacterial activity . . . 91
6.2.2 Minimum inhibitory concentration (MIC) . . . 91
6.2.3 Cell culture experiments . . . 92
6.2.4 MTT assay . . . 92
6.2.5 Statistical analysis . . . 92
6.3 Results and discussion . . . 93

6.4 Conclusions **96**

7 CONCLUSIONS **97**

BIBLIOGRAPHY **100**

APPENDIX 118

APPENDIX A – *SUPPLEMENTARY INFORMATION CHAPTER 3* . . . **119**

APPENDIX B – *SUPPLEMENTARY INFORMATION CHAPTER 4* . . . **124**

B.1 Materials and Methods **124**

B.1.1 Materials 124

B.1.2 Modeling 124

B.1.3 Sputter deposition 125

B.1.4 Layer preparation 126

B.1.5 Atomic force microscopy measurements (AFM) 126

B.1.6 Contact angle measurements 126

B.1.7 XPS characterization 127

B.1.8 Zeta potential measurements 127

B.2 Results **128**

B.3 X-ray photoelectron spectroscopy **130**

APPENDIX C – *SUPPLEMENTARY INFORMATION CHAPTER 5* . . . **131**

1 Introduction

Among the specialized connective tissues, bone tissue is the main component of the human skeleton. It protects the vital organs, produces blood cells, provides support to our body, and acts as levers for muscles. Additionally, bone tissue acts as a reservoir for ions such as calcium and phosphates, thus regulating the internal pH through homeostasis. Its structure is formed by an inorganic part, which mainly comprises phosphorus, calcium, and an organic matrix formed by collagen (mainly type I), proteins and proteoglycans (MAFFULLI; VIA, 2019).

From a biological perspective, bone tissue is formed by three types of cells: osteoblasts, osteocytes, and osteoclasts (MESCHER, 2018). Osteoblasts originate from mesenchymal stem cells, and are responsible for producing organic matrix and depositing inorganic components for new bone formation. Osteocytes are former osteoblasts that help to control the levels of calcium and phosphorus ions; furthermore, they comprise 90% of the cells of a healthy skeleton. The main function of osteoclasts, multinucleated cells originating from macrophages, is bone resorption (MAFFULLI; VIA, 2019; MESCHER, 2018). These three cells are the main cells responsible for bone tissue physiology, which includes bone growth and resorption. This dynamic and continuous process of growth and resorption is also called bone turnover (PARFITT, 2002).

In a healthy person, bone growth occurs through the secretion of collagen from osteoblasts, which is mainly located in the outward part of the bone, as shown in Figure 1. This secretion leads to the formation of a layer called osteoid. The mineral components are deposited through their interaction with glycoproteins and proteins such as osteocalcin, thus increasing the amount of Ca^{2+} under the surface. In addition, osteoblasts release phosphonate-rich vesicles, which work as a nucleus for crystal growth, resulting in the formation of hydroxyapatite crystals ($Ca_5(PO_4)_3OH$) (MESCHER, 2018). This continuous secretion and crystallization leads to the formation of a new bone. Alongside the bone growth, bone resorption, which is regulated by osteoclasts, can be observed. First, these cells, which are in contact with the bone surface, corrugate their membrane. Then, a few enzymes are excreted along with acids, such as nitric and lactic acids. This process causes the dissolution of organic and inorganic matrix accompanied by the absorption of small particles by osteoclasts, lately being released into the blood (KHONSARY, 2017).

Although the aforementioned process is in equilibrium, wherein no bone growth or resorption occurs, some situations, such as osteoporosis and traumas, alter this equilibrium. Generally, traumas can give rise to the need for a partial or total bone replacement. In this scenario, it is important to have an experienced doctor, a well-defined implant, and good

Figure 1 – Schematic representation of mineralization in bone matrix

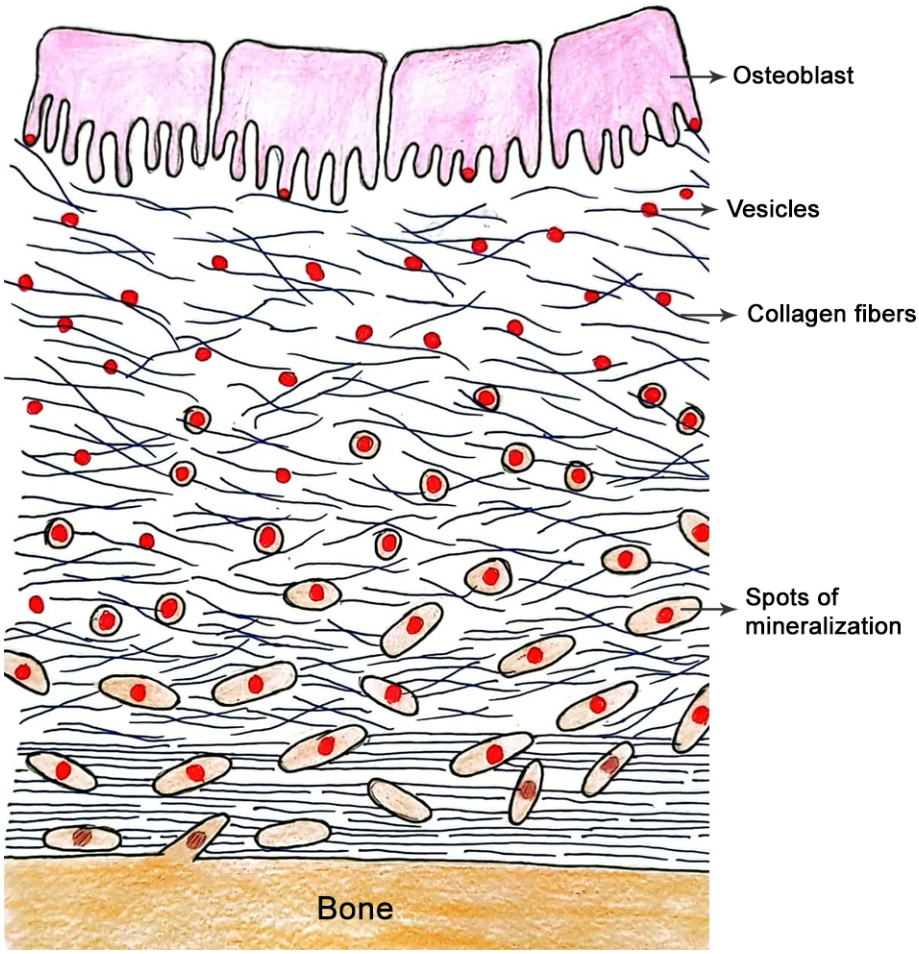

Source: Developed by Marina Cardoso based on (MESCHER, 2018)

health. However, these conditions are not met always; thus, it is crucial to have an implant that can replace the bone and positively intervene in the healing process.

Comorbidities, such as osteoporosis, diabetes, and Chron disease are related to implant failures (BLOCK et al., 2021; KASHI; SAHA, 2019). Additionally, smoking habits, alcoholism, and bruxism are associated with higher chances of implant failure (BLOCK et al., 2021; ANGELIS et al., 2017). For metallic implants, such as dental and hip implants, poor bone quality and overloading can be added as negative factors to the healing process. A review of the cases related to hip implant failure demonstrated the abovementioned for a short period (0-30 days), medium period (31 days to 6 months), and long period (6 months to 8.6 years) of implantation. The presence of comorbidities is listed as one of the factors that cause failure in all the scenarios (JOHNSEN et al., 2006). Although the effect of different types of commodities on the post-surgery is still being discussed. Evidently, the patient health and habits strongly influence the bone healing process after implantation (AGHALOO et al., 2019; BLOCK et al., 2021; ANGELIS et al., 2017). Thereby, the research and production of the multifunctional implant surfaces are crucial in reducing the implant failure rate.

Titanium is the frontrunner constituent element for metallic implants. Being one of the most abundant elements in the world, titanium is a transition metal that can be applied aeronautically to the biomedical equipment. Its use as a constituent for implants starts with the pioneering work of Brånemark and coworkers in the late 1960s (ADELL et al., 1981). Titanium and its alloys presented properties such as toughness, corrosion and wear resistance, and biocompatibility (KAUR; SINGH, 2019; SIDAMBE, 2014). A detailed discussion related to the mechanical, structural, and machine processes of the titanium alloys can be found in the selected reviews (KAUR; SINGH, 2019; LI et al., 2020; NICHOLSON, 2020; SIDAMBE, 2014). Excluding the mechanical properties that must be attended for metallic implants, biocompatibility and other biological aspects are surface-dependent. In other words, properties such as the chemical composition and roughness of the implant surface directly affect the cell response (RATNER; CASTNER, 2020). Titanium is a reactive metal, thus when it is exposed to air, an oxide layer, also known as the passivation layer, is created. Such spontaneous film has a thickness of approximately 4-10 nm. Although its presence increases the corrosion resistance, researchers have been working on different strategies for the growth of this oxide layer, including plasma deposition, sol-gel, and chemical etching (CHOUIRFA et al., 2019; NICHOLSON, 2020).

The titanium dioxide layer commonly presents several hydroxyls on its surface, usually, at a concentration of approximately 4.9–12.5 nm^{-2} (HANAWA, 2019). These groups may be increased by chemical or physical processes. In all the cases, the presence of OH species leads to good biocompatibility of the titanium-based materials (HANAWA, 2019). Once in contact with the biological medium, hydroxyl groups expose Ti^{+} or create Ti-O^{-} species while leaving the surface. The increase of Ti-O^{-} may favor the adsorption of proteins, such as albumin, integrin, and cytokine. After protein adsorption, neutrophils, monocytes, and macrophages adhere to the surface and start the recognition process. Two different responses can be triggered depending on the environmental conditions . In the first case, the foreign body reaction keeps evolving, leading to the encapsulation of the implant by a fibrous capsule, because the macrophages were not able to phagocyte the whole surface. In the second scenario, the collagen fibers are deposited; however, the signalization process is different. In addition to the macrophages' action, osteoblasts start to act using the fibers as a scaffold for new bone formation (BRUNETTE et al., 2001; HANAWA, 2019; JOHN et al., 2016; YOSHINARI et al., 2002).

Among the techniques for titanium dioxide deposition, the sol-gel route is the most suits one for this purpose. Compared to other methodologies, the sol-gel has advantages such as low cost compared with sputtering, low-temperature processing, chemical control, and precise microstructure. Additionally, due to the high surface area, materials prepared using this methodology present higher levels of biocompatibility (OWENS et al., 2016). One of the methodologies for the synthesis of TiO_2 by sol-gel uses titanium isopropoxide as a precursor (TRINO et al., 2018b), the synthesis mechanism is displayed in Figure 2. This

alkoxide is hydrolyzed in an acidified aqueous medium, resulting in a condensation reaction, which transforms $Ti(OH)_4$ in $Ti(OH)_4O^+H_2$ through solvation. Polymer chains of Ti-O-Ti are formed through the olation process, owing to the presence of Ti-OH^+-Ti species. The olation process occurs due to nucleophilic substitutions, in which Ti^{4+} is the nucleophile. The presence of water and alcohol in the medium allows the removal of the H_2O^+ and R-OH species. Peptization is the subsequent step when the aggregates start to break, forming a sol of small particles. Finally, solvent evaporation leads to the formation of the gel. The particle size of the forming gel can be controlled using a surfactant. Regarding its structure, titanuim dioxide exist mainly in three different structures: brookite, rutile and anatase. Rutile is the thermodynamically most stable structure and commonly employed for biomedical applications (DIEBOLD, 2003; TRINO et al., 2018a). Anatase has a higher photoactivity compared with rutile and brookite has a stability between rutile and anatase (LUTTRELL et al., 2014; ZHANG; BANFIELD, 2014). Here, rutile was choosen as main phase for TiO_2.

Figure 2 – Synthesis mechanism of titanium dioxide by sol-gel route using titanium isopropoxide as precursor.

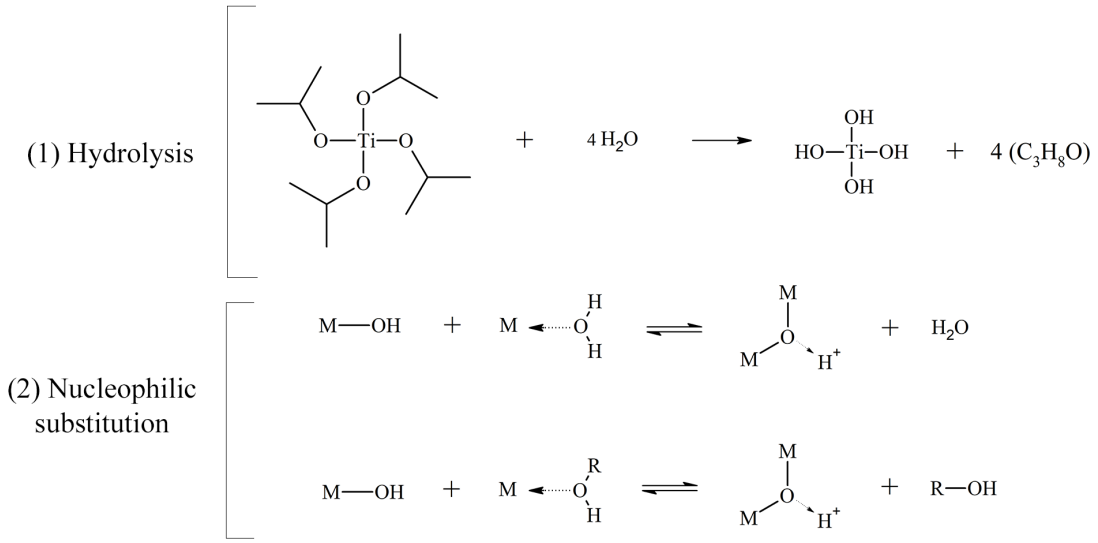

Source: Developed by the author

Since hydroxyapatite is one of the bone constituents, its presence combined with the hydroxyls from titania can also improve the biological performance of the deposited films, compared to the activity of the individual films (HE et al., 2008; WANG et al., 2018). Thus, using hydroxyapatite (HA) films with titanium dioxide, is a suitable strategy for coating metallic implants; however, the adhesion of HA over the titanium surface is poor, which may lead to detaching or cracking under certain levels of loading (HAN; YU; ZHOU, 2008; HARUN et al., 2018). A convenient strategy to overcome this characteristic is the deposition of the mixed films of TiO_2 and hydroxyapatite. Previous studies have shown that, compared to the pure HA coating, composite films of TiO_2/HA may present a 40% higher adhesion force (HAN; YU; ZHOU, 2008). The composite coatings can be produced by adding the

hydroxyapatite powder to the TiO_2 gel; simultaneous synthesis; and a multilayer approach, in which the HA is deposited over the titanium dioxide layer (MILELLA et al., 2001; RAMIRES et al., 2001; SIDANE et al., 2017).

After the deposition of the oxide or composite film, a further step may be performed on the surface, which includes the addition of an organic layer on the surface. This adsorption process has demonstrated the ability to increase the biocompatibility on surfaces, in addition to improving other properties such as hydrophilicity, corrosion, and tribocorrosion resistance (BRONZE-UHLE et al., 2019b; TRINO et al., 2018b; TRINO et al., 2018a). This layer can be a compound with specific properties and characteristics such as bifunctional molecules, proteins, peptides, drugs, and even polymers. Moreover, bisphosphonates (BPs) are a class of molecules suitable for layer deposition.

Similar to pyrophosphate, bisphosphonates are a class of molecules used for the treatment of osseous diseases, such as osteoporosis and Paget's disease. Instead of central oxygen, BPs have a P-C-P structure that presents two substituents, R_1 and R_2, as shown in Figure 3. The presence of a central carbon provides higher stability and increases the resistance to hydrolysis compared to its inorganic analogous (ROGERS; MöNKKöNEN; MUNOZ, 2020). Generally, the R_1 chain is a hydroxyl group and the R_2 may vary from a methyl group to heterocyclic rings (Figure 3 b,c,d). In physiological conditions, bisphosphonates exist mainly in their ionic state, which can vary according to the present chains (BEDOYA et al., 2017; LIN, 2019; ROGERS; MöNKKöNEN; MUNOZ, 2020).

Figure 3 – a) General structure of bisphosphonates, b) etidronate, c) alendronate and d) risedronate linear structure.

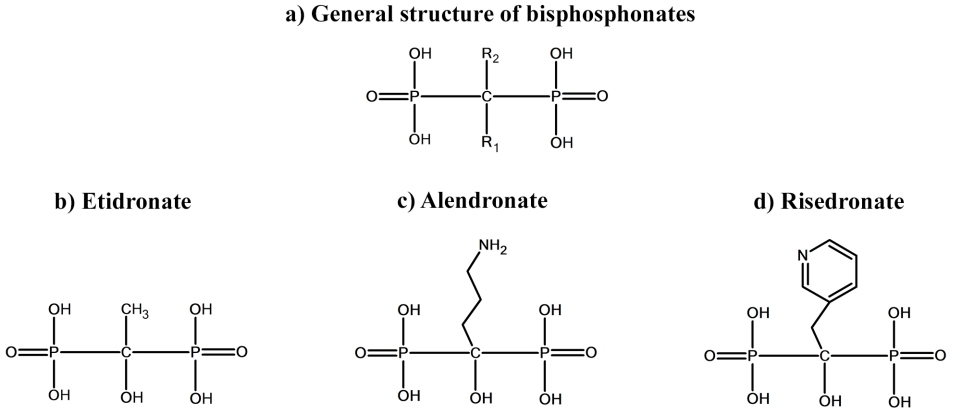

Source: Developed by the author

As mentioned previously, bisphosphonates are usually employed to regulate the bone metabolism, which can be compromised for different reasons. Due to its ionization, bisphosphonates act through the chelation of Ca^{2+} of the body, which leads these molecules to rapidly vanish from circulation due to their strong affinity towards the hydroxyapatite crystals (RUSSELL et al., 2008). Once these molecules are immobilized on the HA surface,

they have different mechanisms of action that are not fully understood. To simplify, the main mechanisms are as follows: (1) when osteoclast lays on the surface and starts the secretion of acids, BPs are released along with calcium crystals; (2) the material is internalized and bisphosphonates are used to synthesize adenosine triphosphate (ATP) owing to the presence of phosphonates groups. However, due to its different structure, the produced ATP analogue is toxic, leading to the death of osteoclast; (3) the presence of BPs in the prenylation of proteins is important for osteoclast function, which also induces cell death. The process is summarized in Figure 4 (CUI et al., 2019; RUSSELL et al., 2008). The knowledge on these mechanisms is still unclear; however, studies showed beneficial effects of BPs on the osteoblast cultures (DOLCI et al., 2019; MALAVASI et al., 2016).

Conversely, excessive or long-term use of bisphosphonates, which are administered orally or intravenously, is associated with jaw osteonecrosis, an adverse effect which is not fully clarified (ABTAHI et al., 2013). Considering the patients with implants, a literature review demonstrated that there is no evidence of the safe use of bisphosphonates before or after the implant surgery (GUAZZO et al., 2017). In other words, bisphosphonates cannot be administrated orally or intravenously as a procedure to reduce the implant failure.

The local use of bisphosphonates is an emerging alternative that aims at avoiding undesirable effects and maintaining its osteogenic activity (ABTAHI et al., 2013; KHAMIS; ELSHARKAWY, 2018). Prior to its usage, the drug can be locally applied through injection or deposited on the implant surface. The immobilization of bisphosphonates on the implant surface can be achieved by immersing the implant in a solution containing the drug. This is a simple procedure compared to administering the injections, which may require health professionals to perform the method.

As mentioned above, the BPs have a strong affinity for HA, which may justify most investigations toward the HA/BPs systems. Various researchers and groups have demonstrated the adsorption mechanism of the bisphosphonates on hydroxyapatite, and the stability of this system under physiological conditions (BOSCO et al., 2015; FORTE et al., 2017; FORTE et al., 2019; NANCOLLAS et al., 2006). These investigations highlight the importance of the HA/BPs systems. However, to effectively use these drugs as implant modifiers, the mechanism of adsorption, desorption, stability, and other aspects of oxide/BPs systems must be scrutinized. Mainly TiO_2/BPs helps to produce implants containing bisphosphonates under the surface. Few studies have shown the characteristics of titania/bisphosphonates arrangements from the physicochemical perspective. To achieve this goal, analytical techniques, such as X-ray photoelectron spectroscopy (XPS), atomic force microscopy (AFM), zeta potential, contact angle, and other surface-sensitive techniques are necessary.

(ROJO et al., 2016) immobilized alendronate on Ti6Al4V. The contact angle results showed that the presence of the adsorbent reduces the contact angle for water and increases the values of surface free energy. The XPS results indicated that alendronate binds on the

Figure 4 – Effects of BPs on bone metabolism. A) Transformation of non-N-BPs into cytotoxic ATP analogs prompts osteoclast apoptosis, while N-BPs induce osteoclast apoptosis by inhibiting FPPS. B) BPs modulate the expression of osteoclast-related genes and promote the expression of osteogenicrelated genes. C) BPs restrain BMSC adipogenic differentiation and promote their osteogenic differentiation. D) BPs inhibit apoptosis of osteoblasts and osteocytes.

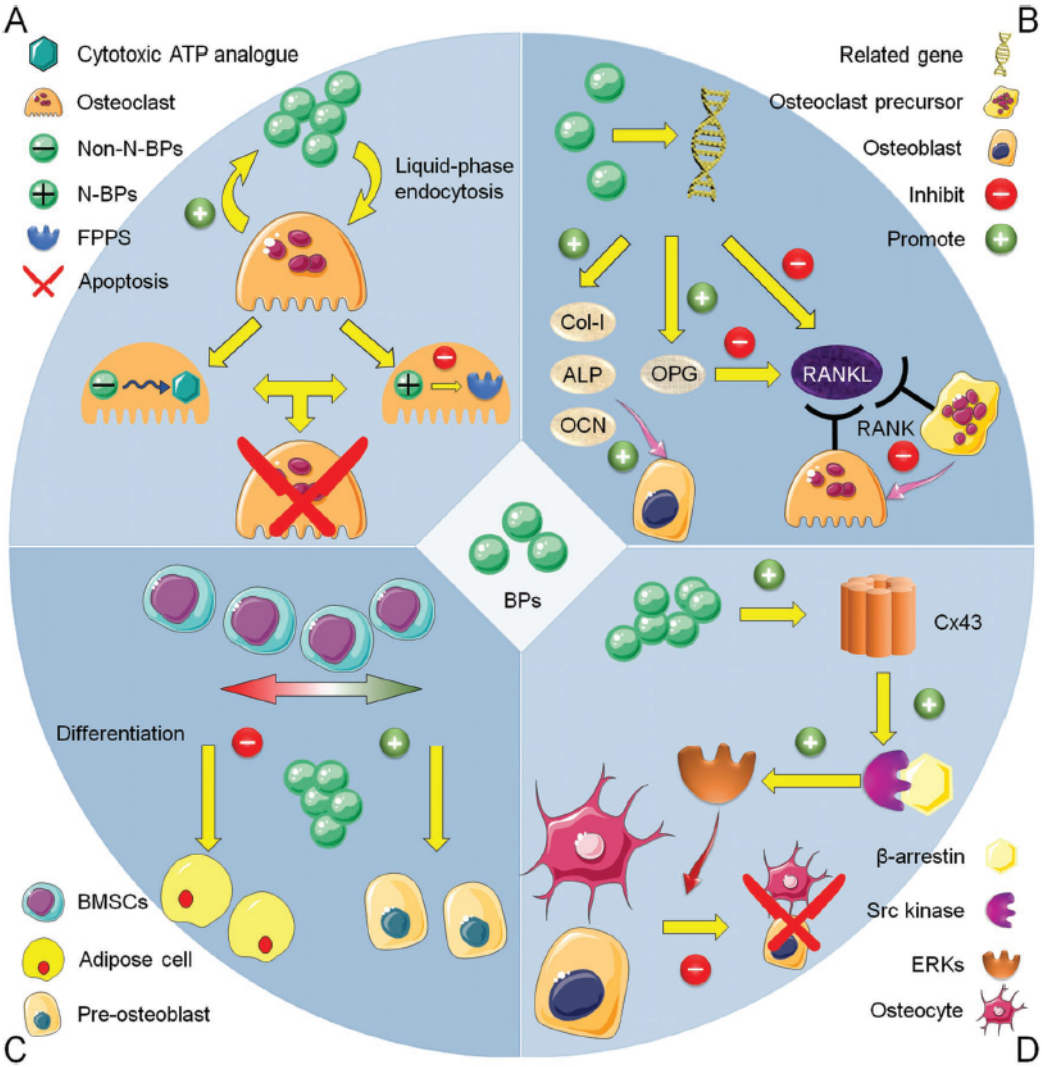

Source: (CUI et al., 2019). Published under the license number 5378781404773.

surface through phosphonates and nitrogen. However, the authors did not provide a strong evidence of the binding mode through XPS, mainly using O1s and C1s high-resolution spectra. Additionally, as indicated by the authors, there is no sufficient proof for monolayer formation; for instance, the lack of layer thickness. Considering that the size of alendronate is approximately 0.94 nm (KARLSSON; ATEFYEKTA; ANDERSSON, 2015), it is reasonable to assume that the presence of a monolayer would be insufficient to cause the biological response presented in the referred study. In this case, the molecules could rapidly vanish and/or be absorbed by the cells. thus, the immobilization efficacy lasts no longer than a few hours.

A different study from (ZHENG; NEOH; KANG, 2017) used alendronate immobilized on the Ti surface. The authors treated the surface with two different methods: plasma oxygen, and silanization. This study presents the survey spectra of XPS, which demonstrated the presence of nitrogen and phosphorus, the characteristics of alendronate composition. However, the high-resolution spectra were not presented, precluding the statements concerning the binding mode. Furthermore, studies demonstrated that the presence of alendronate reduce s the water contact angle of the surface. The immobilization of alendronate does not increase the surface nano roughness, as demonstrated by atomic force microscopy. Using inductively coupled plasma-mass spectroscopy (ICP-MS), the authors showed that the amount of adsorbent on the surface may vary from 308 to 1655 ng/cm^2, thus, indicating a layer thickness of 5.7-32.5 nm, which is different from the expected value of 0.94 nm for a monolayer. Additionally, depending on the immobilization procedure, the alendronate layer can release a maximum of 400 ng/cm^2 in 14 days of incubation in water. This result suggests the presence of a synergetic effect between the adsorbed and released molecules, as the same work mentioned that a modified titanium surface has a better biological performance in terms of cell survival and cell metabolism.

Using the density functional theory (DFT) (PETROVIć et al., 2020) discussed that alendronate is adsorbed on the TiO_2 surface through a competition between -NH_2 and -PO_3H groups, leading to two possible conformations. In the first one, the alendronate binds through amino and phosphonate; in the second one, it is through phosphonate only. Although this discussion can elucidate the aspects of the adsorption process, the simulation does not include the protonation states of the molecule. As indicated by the different studies, bisphosphonates exist mainly in their ionic state at physiological pH (BEDOYA et al., 2017; FERNáNDEZ; ORTEGA-CASTRO; FRAU, 2017; KE et al., 2016). The authors associated free nitrogen and phosphonates with the decrease of water contact angle. Electrochemical measurements indicated that the alendronate layer increases the corrosion resistance and may remain stable for seven days.

A study by (BRONZE-UHLE et al., 2019a) showed the influence of UV irradiation on the bisphosphonates adsorption. In this work, the TiO_2 surface was irradiated with UV light before immersion in the bisphosphonate solution. The XPS results indicate modifications in the alendronate and risedronate adsorption. Without the UV irradiation, the BPs can bind through the nitrogen-containing and phosphonates groups. While on an irradiated surface, the interaction surface-BPs occur through phosphonate groups alon e. In agreement with other studies, a decrease in water contact angle was observed.

The effects of UV radiation before the bisphosphonates adsorption on titania is not fully recognized. (BRONZE-UHLE et al., 2019a; KIM et al., 2017) demonstrated that this process modifies the binding mode and may improve the biological performance. (KIM et al., 2017) showed that the implants irradiated with UV light before immersion in alendronate

solution presented better biological results compared to the non-irradiated titania, including cell viability, adhesion, and alkaline phosphatase. Different authors studied the adsorbed bisphosphonates on surfaces that are not hydroxyapatite, although most of them focused on the biological performance of such modification. In this aspect, they reported that the immobilization of BPs can improve the biological markers and increase cell proliferation, survival, and adhesion (CHA; LEE; LEE, 2018; MALAVASI et al., 2016; YOSHINARI et al., 2001). This important information may contribute to the development feasible implants covered with BPs.

Nonetheless, some topics still remain unclear. Since such results are surface-dependent, well-characterized surfaces are crucial. As discussed by different authors, a well-performed surface characterization helps to understand how the adsorbed molecules can increase the surface biocompatibility. Therefore, oxide/BPs and composite/BPs systems are good candidates for extensive characterization.

2 GENERAL AND SPECIFIC GOALS

Considering the above mentioned discussion, the present work has as general goal to elucidate aspects of bisphosphonates adsorption on TiO_2, HA and HA+TiO_2 surfaces. From bisphosphonates, etidronate, alendronate and risedronate were chosen as surface modifiers, as shown in Figure 3 b,c,d. As hypothesis, this works try to verify if bisphosphonates can positively affect cell growth on the proposed surfaces.

As specific goals, we propose preparation of TiO_2, hydroxyapatite and composite surfaces, togheter with an extensive characterization of bisphosphonates layers using mainly X-ray photoelectron spectroscopy. Additionally, we propose to obtain a adsorption curve of bisphosphonates on titania (anatase and rutile).

3 New details of assembling bioactive films from dispersions of amphiphilic molecules on titania surfaces

This chapter was originally published on *RSC Advances, 2020, 10, 39854-39869* as original article, the manuscript is available through the DOI: 10.1039/D0RA06511K.

3.1 Introduction

The design of novel functional biomaterials depends on tailoring their multiscale structures (WEI et al., 2014; STAPELFELDT et al., 2019). Surface modification is a suitable strategy to enhance the properties of biomaterials such as biocompatibility and antibacterial efficacy (CORRALES-UREñA et al., 2020). Different procedures are well established, such as depositing silver as an antibacterial component or immobilizing functional molecules on medical products (BORCHERDING et al., 2019; BRONZE-UHLE et al., 2019a).Aiming to introduce antibacterial properties to medical devices, a valid alternative is grafting chemically reactive quaternary ammonium compounds (QACs), such as dimethyloctadecyl (3-trimethoxysilylpropyl) ammonium chloride (DMOAP). DMOAP has a quaternary ammonium group that is separated by a propylene spacer from a hydrophilic tri-methoxy silane group and bound to an aliphatic octadecyl chain ($C_{26}H_{58}NO_3SiCl$), which is responsible for its hydrophobicity (MENG et al., 2015).ODPA (octadecylphosphonic acid) also contains a hydrophobic chain, and its hydrophilicity is due to a protonated or deprotonated phosphonate group. The immobilization of ODPA can also form antibacterial response on surfaces (ZHANG et al., 2017). Structural formulas of linear DMOAP and ODPA conformations are presented in Fig. 5. Hydrophobic surfaces can be suitable for biomedical devices to avoid protein adsorption, increase the surface charge in contact with aqueous fluids, and establish an antimicrobial effect (ZHANG et al., 2017; ZHANG; WANG; LEVäNEN, 2013; BRAUNWARTH; BRILL, 2014; GRACE et al., 2016). Modifications of surface charge play an important role in achieving antimicrobial efficacy in different bacteria-containing media (KAUR; LIU, 2016). Although a long alkyl chain could increase the surface hydrophobicity and influence bacteria adsorption, the presence of a cation induces electrostatic interaction with the bacteria phospholipid bilayer (DOGRA et al., 2012).

As reviewed by Elena and Miri (ELENA; MIRI, 2018), QACs can be immobilized on different surfaces, from cotton fibers to metal oxides, apart from being incorporated in the synthesis of resins for dental applications (ANTONUCCI et al., 2012). Quaternary ammonium

Figure 5 – Linear structure of (a) DMOAP and (b) ODPA.

(a) Dimethyloctadecyl[3-(trimethoxysilyl)propyl]ammonium chloride

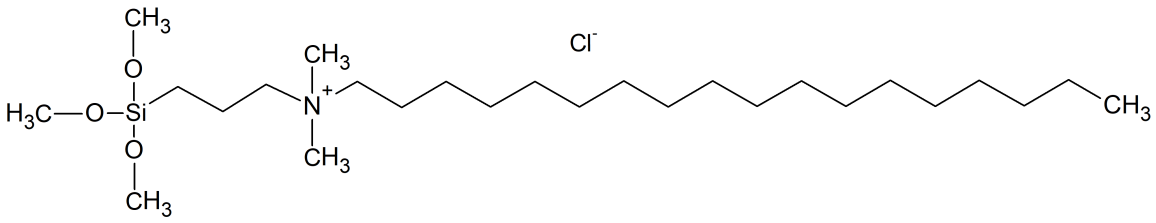

(b) Octadecylphosphonic acid

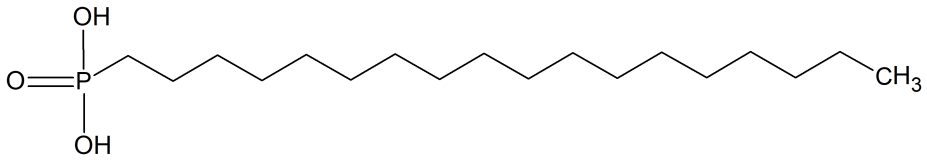

Source: Developed by the author

compounds present antibacterial activity even when their head groups are hydrolysed in a solution; however, non-immobilized QACs are often active surface water contaminants and can potentially cause environment damage (BOETHLING, 1984). Thereby, immobilization of QACs on a surface while largely maintaining their activity is a desirable but challenging procedure, which aims to provide a non-release system and avoid environment impact (NEU, 1996; OOSTERHOF et al., 2006). For instance, Meng *et al*. demonstrated that when immobilized on cellular membranes, DMOAP can maintain its antibacterial efficacy in various conditions, such as pH of 3.5 and temperature of 50℃ (MENG et al., 2015).

Despite its attested antibacterial efficacy, the mechanism of action of DMOAP has not been fully elucidated. The mechanism has been described in the following manner: attraction between the positively charged DMOAP layer and the negatively charged bacteria cell membrane occurs supported by van der Waals interactions between the respective DMOAP or phospholipid hydrophobic tails (ASRI et al., 2014). The electrostatic attraction leads to an ionic interaction causing the transport of divalent cations (Ca^{2+} and Mg^{2+}), inducing membrane disruption and consequent death of the bacteria (ASRI et al., 2014; BELKHIR et al., 2017). The surface charge density induced by the ammonium cation plays a crucial role in the antibacterial activity. Asri *et al*., using AFM measurements, reported that immobilized QAC has a strong interaction with *Staphylococcus epidermidis*, and the force of interaction with the bacteria surface was five to six times greater than usually found for bacteria adhesion on surfaces, which are in a range of 1 nN (ASRI et al., 2014). He *et al*. observed that when *E. coli* attaches on a DMOAP surface, a distortion of the cell membrane leads to its rupture (HE et al., 2016).

On the other hand, immobilized ODPA provides antibacterial properties due to the increased surface hydrophobicity, consequently avoiding the adsorption of some bacteria (ZHANG et al., 2017). Zhang *et al*. reported that ODPA immobilization on titania nanotubes not only avoids bacterial adherence but can also modulate the release of Sr and Zn when these are dopants of the nanotubes (ZHANG et al., 2017). ODPA is irreversibly adsorbed on $Ti_{0.5}Al_{0.5}N$ surfaces forming a non-release system, as reported by Theile-Rasche *et al* (THEILE-RASCHE et al., 2020).

In addition to characterization, useful tools for revealing the arrangement of DMOAP and ODPA layers on surfaces are contact angle measurements, atomic force microscopy, and X-ray photoelectron spectroscopy. DMOAP and ODPA modify the wettability of the surface due to their long alkyl chains. Besides the binding situation and area density of the functional groups of those molecules, quaternary ammonium for DMOAP and phosphonate for ODPA can be detected by XPS (ASRI et al., 2014; ZHANG et al., 2017; THEILE-RASCHE et al., 2020; DAI et al., 2014).

For tailoring the physicochemical properties in aqueous environment, such as zeta potential and wettability of the layer systems formed by immobilized DMOAP and ODPA, details about the adsorption process are important to understand. To elucidate the effects of process parameters in forming bioactive layers, combining microscopic and spectroscopic studies with nanoscale sensitivity and a layer build-up on flat and chemically well-defined substrates is innovative, as was shown for designing highly active antifouling layers (KULKA et al., 2019) and antimicrobial films, promoting protein adsorption (FABRE et al., 2018), and verifying the influence of electrolytes on contact angle (AL-ZAIDI; FAN, 2018).

For achieving antibacterial contact-activity, numerous approaches for tailoring substrate surface properties have been reported. Surface structure, wettability, composition, and time-dependent release properties in aqueous environment have been generally assessed. These studies revealed that increased antimicrobial activity is promoted by adjusting the surface roughness instead of providing smooth substrate surfaces; introducing amphiphilic moieties in films that will be in contact with phospholipid-based bacterial membranes; integrating molecular groups that affect the surface charge like QACs; or facilitating the release of metal ions from bulk film regions that are not exposed to the convective transport for permitting longer-term activity of antimicrobial coatings (AMC). The underlying antimicrobial strategies may comprise several components. Among them, providing anti-adhesive surfaces to avoid or retard microbial attachment (AGUIAR et al., 2019), contact-active surfaces that are based on immobilized and not released active species (CORRALES-UREñA et al., 2020; UREñA et al., 2015), and biocide-releasing surfaces (ADLHART et al., 2018).

Tailoring strongly attaching films composed of amphiphilic molecules with respect to their antibacterial activity has been reported based on approaches considering thick films (HSU et al., 2020; FORMAN et al., 2016) and polymeric (HE et al., 2016) or hybrid

(ASRI et al., 2014) bulk materials containing quaternary ammonium species. For such substrates, a substantial conformational freedom of the molecular entities exposing the quaternary ammonium species may be expected in a swollen state in the presence of aqueous environments containing bacteria (HE et al., 2016).

In addition to chemical modifications, the topography of a surface can significantly affect its hygienic status, either beneficially (reducing microbial retention) or negatively (increasing retention) (ADLHART et al., 2018). Findings of surface charge densities around 1.5 x 10^{15} cm^{-2} or even 10^{16} cm^{-2} for monovalent ammonium cations are based on calculations considering the geometric surface area of rough substrates rather than on their active surface area, since monolayer densities do not exceed 5 x 10^{14} atoms cm^{-2}, even of unbranched nonanethiols on gold (CAMPOSEO et al., 2006; JIAO et al., 2017).

The present study aims to achieve a more profound understanding about material-related properties governing a contact-killing ability from the interaction between bacteria and substrates containing quaternary ammonium species by assessing dynamic effects in the bacteria/QAC interface. Properties of silane-based layers and their mechanism of immobilization need to be explored to devise deposition processes and exploit their versatility for surface modification (PLETINCX et al., 2019). In addition, systematic studies for governing the contact formation and its effect by tailoring the substrate surface were performed. A versatile and well-controlled multi-step approach was developed for designing the AMC surface. Starting from a topologically well-defined substrate that may be smooth or micro-structured, thin biocompatible and non-cytotoxic titania nano-films were deposited as a base for the application of AMCs.

As immobilizing QACs in thin layers may strongly restrict conformational freedom of the molecules, DMOAP films with different thickness were studied starting from the monolayer regime to demonstrate the versatility of our approach. Studies relating layer structure and its biological activity are scarce and need to be clarified (LIU et al., 2020); thus, this work explores this gap in the literature, showing well characterized layers before and after biological assays. Smooth substrates were used to restrict the potential bacteria/QAC interface to the geometrical surface area. Inorganic oxidic titania substrate material was also used to exclude swelling effects upon exposure to aqueous environments. Finally, ODPA SAMs were used, which like DMOAP contain hydrophobic octadecyl molecular tails. The orientation of amphiphilic molecules in such well-ordered monolayers provides a reference for working out the effects of molecular orientation observed in thin DMOAP films.

3.2 Materials and methods

3.2.1 Materials

Silicon wafers (diameter of 100 mm) from Si-Mat and glass slides (75 x 25 mm) from Thermo Scientific® were used as substrates. Titanium dioxide was obtained from a metallic titanium target that was used for sputter-deposition in an oxygen containing atmosphere. A methanol-based mixture of 42 wt% dimethyloctadecyl(3-(trimethoxysilyl)propyl)ammonium chloride (DMOAP) (CAS 27668-52-6) and 8 wt% of (3- chloropropyl)trimethoxysilane from SIGMA-ALDRICH® and octadecylphosphonic acid (ODPA) (CAS 4724-47-4) from TCI® Germany were employed for the layer formation experiments on sputter-deposited TiO_2 on silicon wafers and glass. Ethanol 99% (CAS 64-17-5) from Labochem® was used as solvent to prepare DMOAP and ODPA solutions.

3.2.2 Preparation of bulk DMOAP and ODPA for XPS investigation

To prepare samples for XPS investigations and bioactivity tests, DMOAP was dropped as received in a silicon wafer, and after evaporation of the solvent the obtained specimen was henceforth called “bulk DMOAP” sample. A second sample was prepared by exposing the obtained solid deposit product to water at room temperature for distinct periods and subsequently dried. The thus prepared samples were called “water exposed DMOAP”. As a reference for the biological assay, DMOAP was dropped on titania surface and the solvent was left to dry in air. The procedure was repeated twice. The final sample named “Blot DMOAP” was a thick layer heated overnight at 100℃ in an oven at ambient atmosphere.

For preparing the so-called “bulk ODPA” samples, a small quantity of the ODPA product powder was dissolved in 99% ethanol to obtain a turbid suspension. A drop was placed on a silicon wafer and gently blown dry using an air stream generated by a hand bellow to remove the solvent excess.

3.2.3 Surface preparation – film deposition

A silicon wafer was cut in two different sizes, 3 x 5 mm and 20 x 20 mm, and the respective pieces were used for XPS measurements and biological assays, respectively. After the cutting procedure, the substrates were ultrasonically cleaned in water for 10 minutes. Glass slides were used as received. Subsequently, the substrates were placed in a vacuum chamber then pumped until reaching a pressure of 10^{-5} hPa. The argon flux was adjusted to 120 sccm. Finally, the titanium dioxide deposition started. First in the deposition process, the target was sputtered without the presence of oxygen for 30 s. Afterwards, oxygen was slowly added into the chamber, using a flux of 9 sccm, for 900 s. A power of 2300 W and maximum bias of 765 V were applied. For all adsorbents, the layer formation experiments

were performed five minutes after sample removal from the chamber.

3.2.4 Solution preparation

Two different solutions containing DMOAP were prepared, similar as described by Torkelson *et al* (TORKELSON et al., 2012). A volume of 0.6 mL of 42 wt% DMOAP solution in methanol was diluted in 49.4 mL of 99% ethanol to produce the first working solution. For the second solution, the same procedure was followed and 10 drops (approx. 50 μL) of 1 M aqueous hydrochloric acid (previously prepared) were added after mixing the alcoholic liquids. The solutions were called “DMOAP-N” (without acid addition) and “DMOAP-A” (with acid addition).

ODPA solution was prepared as follows: 167.25 mg of ODPA were dissolved in 50 mL of 99% ethanol, establishing a concentration of 1 mM.

All immersion experiments of titania-coated substrates were performed approximately 30 minutes afer solution preparation. In this freshly prepared state, the solutions visually appeared transparent, clear, and colourless and remained as such during the immersion procedures.

3.2.5 Layer formation on TiO_2

The procedures described below were used for all titania-coated substrates. All samples were gently rinsed (either in distilled water or ethanol) after immersion in DMOAP and ODPA solutions, and identified as “water rinsed” or “ethanol rinsed”, respectively.

3.2.6 DMOAP adsorption

To attach DMOAP on the titanium dioxide surfaces, the substrates were immersed for 10 minutes or 24 hours at room temperature for each DMOAP solution. After the submersion time, the samples were removed from the solution and gently rinsed using distilled water from a wash bottle.

Two distinct drying procedures were employed. One method consisted in blowing the sample surface using clean compressed air after the washing procedure. For the second method, the samples were subsequently placed in an oven and completed drying in air at 100 ℃ overnight. To clarify the achieved samples, the descriptions of the preparation label and conditions are summarized in Table 1.

3.2.7 ODPA adsorption

ODPA was adsorbed also through sample immersion in ODPA solution for 18 hours. Additionally, the samples were removed and either of the two above-described washing

Table 1 – Parameters of immersion, drying method, and sample name for DMOAP/titania films prepared from two different DMOAP solutions: DMOAP-N (without acid addition) and DMOAP-A (with acid addition)

Solution	Immersion time	Drying method	Sample name
DMOAP-N	10 minutes	Blown using compressed air	TiO_2/DMOAP-N 10 min
		Heated in an oven at 100 ℃ in air overnight	TiO_2/DMOAP-N 10 min heated
	24 hours	Blown using compressed air	TiO_2/DMOAP-N 24h
		Heated in an oven at 100 ℃ in air overnight	TiO_2/DMOAP-N 24h heated
DMOAP-A	10 minutes	Blown using compressed air	TiO_2/DMOAP-A 10 min
		Heated in an oven at 100 ℃ in air overnight	TiO_2/DMOAP-A 10 min heated
	24 hours	Blown using compressed air	TiO_2/DMOAP-A 24h
		Heated in an oven at 100 ℃ in air overnight	TiO_2/DMOAP-A 24h heated

Source: Developed by the author

procedures was followed. All samples were blown dry using air from a hand bellow to remove the excess solvent.

3.2.8 Atomic force microscopy

Nanomechanical surface properties were assessed applying a Bruker Dimension Icon3 with a Nanoscope VSPM control unit and the software NanoScope V9.40R1. The cantilever and tip used were selected according to the surface properties (XSC11- Pt, MikroMesh, force constant 40 nN nm^{-1}, tip radius < 20 nm). The calibration of the force constant was done by analyzing the thermal noise in combination with the Sader method (SADER et al., 2016).The sensitivity was calibrated with the help of an Al_2O_3 substrate. The tip radius was determined using the image of a nano rough Ti reference sample. The quantification was carried out according to a modified Villarubia method that was implemented in NanoScope (VILLARRUBIA, 1994). The QNM mode was used to quantify the nano-mechanical properties. For this purpose, the cantilever was excited non-resonantly at 2 kHz with amplitude of approximately 15 nm and indented into the surface with a depth up to a maximum of 2 nm; therefore, the indentation depth was approximately 10 nm.

Height profiles were obtained using a Nanosurf easyscan AFM device. The images were taken in a resolution of 512 x 512 pixels in different sizes. For this, the non-contact mode (variable force) was used with a scan line ratio of 2 seconds for each image and a cantilever with a force constant of 40 nN nm^{-1}. The post treatment was performed using the Gwyddion 2.55 software. First, a step line correction was applied. Then, the rows were aligned using a polynomial degree equal to five, and finally the strokes were corrected. The tip was a Tap190Al-G from Budget Sensors with a resonant frequency equals to 190 kHz.

3.2.9 Contact angle measurements

Contact angle measurements were performed immediately after the drying procedures. The analysed samples were TiO_2 sputter- deposited on glass slides. The measure-

ments were evaluated using the mobile surface analyser – MSA from KRÜSS – at room temperature.

HPLC quality water and diiodomethane were used as probe liquids, and 2 μL of each liquid were simultaneously and automatically dropped on the surface. Then, the contact angle for each drop was recorded using the tangent method. Two distinct regions of the sample were analysed, and the mean contact angle for each liquid was calculated.

Changes of apparent water contact angles as a consequence of exposing DMOAP coated titania specimens to aqueous bacteria medium were recorded using a goniometer based (OCA15 Plus, Data Physics Instruments, Germany) approach and applying the sessile drop technique. For each measure- ment, 5 μL drops were formed using HPLC-grade water (Acros Organics, Germany) and the subsequent contact angles were taken and analysed by the software SCA202 (Data Physics Instruments, Germany). The reported contact angles are an average of at least three measurements for each sample.

3.2.10 XPS characterization

XPS characterization was carried out using a Kratos AXIS Ultra system with a monochromatized Al Kα X-ray source (energy hν = 1486.6 eV). The base pressure of the analysis chamber was approximately 6 x 10^{-8} Pa. Spectra were acquired in the constant analyser energy mode using pass energies of 160 eV and an energy step of 0.444 eV for survey spectra and 20 eV and energy step of 0.066 eV for detail scans. Spectra fitting was performed using CasaXPS (v2.3.18, Casa Software Ltd). First, the binding energy scale of the spectra was aligned using the C1s signal at 285.0 eV of the aliphatic hydrocarbon species. Then, the signal area to analyse was set using a Shirley-type or linear background. Peak components were adjusted using the line shape GL(30). The full widths at half maximum (FWHM) for the C1s components were set to be equal. The created areas were fitted using the Marquardt–Levenberg algorithm. Based on the signal attenuation, the thickness of the adsorbed layers was estimated using the equation $d = ln(y).l$, where d is the thickness of the adsorbed layer, y is the ratio between the area of the Ti2p peak from the coated sample and the pristine sample, and l is the inelastic mean free path of the electrons in the organic film (2.8 nm for Ti2p). For such estimation, the surface coating was assumed to be homogeneous (WEI et al., 2014). A thickness of 0.6 nm was considered for the adventitious carbon layer on the titanium substrates (MANGOLINI et al., 2014). An estimated layer thickness of an adsorbate was calculated based on the assumption that the adventitious carbon layer was replaced by the adsorbate layer. Atomic surface concentration values were calculated based on the simplifying geometric model assumption that the sample surface is homogeneously composed.

3.2.11 Zeta potential measurements

Zeta potential measurements were performed with different titanium dioxide samples deposited on glass slides. The values were recorded using the SurPASS™ 3 device from Anton Paar at room temperature. The adjustable gap cell was used, and the gap adjusted to 100 mm. The pH was adjusted using 0.05 M solution of potassium hydroxide and 1 M solution of hydrochloric acid, respectively. The pH step was set to 0.75 in range from pH 8 to pH 4 (in this order) and measured with a pH meter sensor innate to the equipment. Before the measurements, the samples were stored for 24 hours in 2 hPa at room temperature. The error bars were estimated based on three distinct

3.2.12 Antibacterial assays

Escherichia coli bacterium (strain DSM 10290) was cultured in LB broth medium at 37℃ in aerobic conditions for 24 h. The growth culture suspension was centrifuged twice at 13000 rpm for 5 minutes and suspended in PBS buffer. The optical density (OD) was measured at 600 nm in UV-Vis Specord 200 Analytic Jena spectrophotometer and the concentration was adjusted to 1 x 10^7 CFU m^{-1} (with 0.06 OD corresponding to 2 x 10^8 CFU mL^{-1}) in minimal medium (1 : 100 of LB broth medium in PBS buffer). In a UV2 Sterilizing PCR Workstation, at room temperature, the samples (n = 3) were placed in sterile Petri dishes and received sprays of isopropanol 70% . The Petri dishes lids were opened, the working bench was closed, and the UV light was turned on for 30 minutes to sterilize the samples. Afterwards, 50 mL of bacterial solution were applied over each sample surface and a sterilized cover glass slip (18 x 18 mm) was placed to spread the drop over the substrate, according to the ISO 22196. Moreover, 2 mL of PBS was pipetted in the outlines of the Petri dishes to prevent evaporation. After incubation for 4 h at 37℃, the cover glass slips were removed, and samples were carefully washed twice with distilled water to remove non-adherent or weakly adherent bacteria. The rinsed water was kept in a 2 mL centrifuge tube for further analysis. The samples were placed into a 50 mL centrifuge tube, which was filled with 15 mL of PBS buffer. The tubes were sonicated (Ultrasonic bath Sonorex RK100 Bandelin Electronic, Berlin, Germany) for three minutes and vortexed (Minishaker MS2, IKA – Werke GmbH & Co. KG, Staufen, Germany) for one minute to allow detachment of the adherent bacteria. The 24 h kinetic of both the non-adherent bacteria (from the rinsed water) and the bacteria detached from the sample were evaluated using Mith- ras LB 940 Microplate Reader (Berthold Technologies Ltd). Accordingly, 150 μL of each bacterial solution + 50 μL LB broth medium were pipetted in a well of a 96-well cell culture plate, which was placed in the device with all parameters set in the same conditions of the bacterium culture. The bacterial growth was related to the bacteria adhered on the surface of the samples, which after ultrasound and vortex remained alive and healthy to continue growing in suitable nutrients and temperature conditions. The bacterial growth from the rinsed water indicated a

bacteriostatic effect of the sample, which inhibits the initial bacteria adhesion and further biofilm formation.

Testing with Gram-negative *E. coli* was introduced to the experimental design because DMOAP immobilized on polymers exhibited comparatively low minimum inhibitory concentra- tions (MIC) against *E. coli* and Gram-positive *S. aureus* as compared to *C. albicans fungus* (LI et al., 2016). Gram-negative *S. mutans* was chosen to be part of the conceptual design including bulk DMOAP specimens because of its relevance for dental research and considering the paramount objective was to identify if DMOAP shows an antibacterial effect against *S. mutans*.

3.3 Results and discussion

From the XPS spectroscopic point of view, the approach presented in this study profits from opting for smooth titania films. Moreover, on smooth substrates, the morphology of organic adsorbates can be accessed (WEI et al., 2014). In comparison to silica or alumina adsorbents exhibiting contributions to the O1s signal at binding energies around 533.0 eV (FERREIRA-NETO et al., 2019; TORNOW et al., 2005), the O1s signal contributions related to oxide, hydroxide, or carbonate-related bulk and surface species, in case of titania substrates, are characterized by binding energies around 530.2 and 531.6 eV ($\pm$0.1 eV), respectively (FERREIRA-NETO et al., 2019). This facilitates the spectroscopic characterization of the chemical environment of oxygen species in thin adsorbates of complex oxygen-containing amphiphilic adsorbates (like ODPA or DMOAP) on titania substrates.

3.3.1 XPS characterization

3.3.1.1 Bulk sample

Pure bulk material ODPA is composed of octadecylphosphonic acid molecules with a molecular structure displayed in Fig. 5; the molecule presents the following stoichiometry: $C_{18}H_{39}O_3P$. If a sample of this pure bulk material has a homogeneous composition, the atomic concentrations listed in Table 2 are expected based on this stoichiometry. Additionally, the measured atomic concentration (given in at%) of carbon is slightly higher than that displayed. The values obtained for carbon, oxygen, and phosphorous are close to the stoichiometrically expected values. The concentration ratios [C]/[O], [C]/[P], and [O]/[P] indicate that a minor excess of carbon species is found at the sample surface, as shown in Table 3.

High resolution XPS spectra for the investigated bulk ODPA sample are presented in Fig. 6. C1s high resolution spectra were fitted using two contributions: one contribution at 285.0 eV from aliphatic carbon and the second centred at 285.8 eV due to C*–P species.

Table 2 – Comparison between expected for homogeneous solid ODPA and obtained values from the XPS-based evaluations of atomic concentration

	[C]			[O]			[P]	[Si]		
Atomic concentration (at%)	Total	[C*-C/C*-H]	[C*-P]	Total	[P-O*-H]	[P=O]	Total	Total	[Bulk Si]	[SiO^*_2]
Expected value	81.92	77.33	4.59	13.64	9.09	4.54	4.54	0	-	-
Obtained from data evaluation	82.68	78.45	4.23	11.75	7.84	3.90	4.22	1.34	1.18	0.16

Source: Developed by the author

From the molecular structure, the intensity for XPS signals related to C*–P and P*–C species in ODPA is expected to be equal to the atomic concentration [P] of phosphorus species in ODPA (4.5 at%). Based on an appropriate calibration of the applied relative RSF (relative sensitivity factors) for C1s and P2p in the XPS measurement, an area constraint was set to guarantee that the evaluated [C*–P] atomic concentration was equal to the evaluated atomic concentration [P] of phosphorus species in the investigated ODPA bulk material.

Table 3 – Ratios between the atomic concentrations of carbon [C], phosphorous [P], and oxygen [O] species, as expected from stoichiometry and found in XPS investigations

Atomic concentration ratio	[C]/[O]	[C]/[P]	[O]/[P]
Expected from stoichiometry	6.0	18.0	3.0
Found by XPS	7.0	19.6	2.8

Source: Developed by the author

Figure 6 – XPS high resolution spectra for investigated bulk sample ODPA, (a) C1s, (b) O1s and (c) P2p signal.

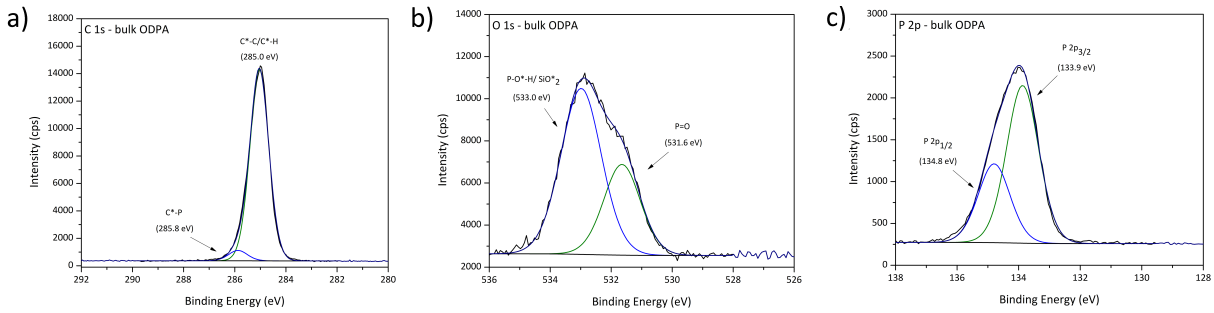

Source: Developed by the author

Outcomes of the proposed fit agree with the signal positions reported by (MILOšEV; METIKOš-HUKOVIć; PETROVIć, 2012), who reported C*–P species with a C1s binding energy between 285.8 and 286.2 eV in ODPA on a NiTi alloy surface. The obtained atomic concentration ratio [C*–C|C*–H]/[C*–P] equals 18.5, and the expected value is 17. The atomic concentration [C*–C|C*–H] of aliphatic carbon species obtained from the fitting is slightly higher than the expected value. The aspects to assess this difference are the presence of additional substances other than ODPA, a non-precise relative sensitive factor ratio of P2p and C1s, and the presence of non-isotropic dried ODPA micelles on the sample surface inspected by XPS. O1s spectra were fitted using two contributions based on the obtained binding energy values. The causative oxygen species were identified as P=O* (531.6 eV) and

P–O*H with minor contributions from SiO^*_2 (533.0 eV). The positions agree with previous studies of ODPA on different surfaces (THEILE-RASCHE et al., 2020; MILOšEV; METIKOš-HUKOVIć; PETROVIć, 2012; GOUZMAN et al., 2006). The expected and obtained atomic concentration ratio of [P–O*–H]/[P=O*] are both equal two (see Table 2). These results evidence an agreement between the ODPA stoichiometry and the proposed fit. The Si2p signal showed the spin–orbit coupling ($\triangle$E = 0.6 eV) from the silicon wafer used as substrate and a peak centred at 103.3 eV from Si^*O_2 on substrate surface (see Fig. 32a) (GOUZMAN et al., 2006; MOULDER, 1993). Based on the fitting, merely 0.16 at% of silicon is in the form of Si^*O_2. P2p high resolution spectra displayed only the characteristic spin–orbit coupling with an energy distance of 0.93 eV (CICCO et al., 2019; ROJO et al., 2016). The single P2s peak was centred 57.8 eV higher than the $P2p_{3/2}$ signal, in agreement with the value reported in the literature (see Fig. 32b) (MOULDER, 1993).

Concerning the second amphiphilic agent, pure bulk material DMOAP is composed of DMOAP entities, with the stoichiometry of $C_{26}H_{58}ClNO_3Si$ (see Fig. 5). If a sample of such pure bulk material has a homogeneous composition, the atomic concentrations listed in Table 4 are expected in an XPS investigation based on this stoichiometry. To compare the former with a thick vacuum-dried film, the atomic concentration for a fully hydrolysed DMOAP is also listed.

Table 4 – Atomic concentration in at% of the distinct surface species by XPS investigations, compared to stoichiometrically expected values.

	[C]				[O]	[N]			[Si]	[Cl]
Sample name	Total	[C*-C/C*-H]	[C*-N^+]	[C*-O-Si]	Total	Total	[-N^+]	[N*-O]	Total	Total
Bulk DMOAP, vacuum-dried	82.21	56.17	14.30	11.74	9.53	3.06	2.61	0.45	2.80	2.40
Expected value for bulk DMOAP	81.52	59.37	12.50	9.38	9.36	3.13	3.13	-	3.13	3.13
Water exposed DMOAP	80.28	61.33	10.27	8.68	8.73	3.46	3.42	-	4.31	3.22
Expected values for fully hydrolysed DMOAP	79.31	65.52	13.79	0	10.34	3.45	3.45	-	3.45	3.45

Source: Developed by the author

For the water treated DMOAP, a hydrolysis of the methoxysilane groups might be expected according to the established behaviour of methoxysilanes with short alkyl chains (SALON; BELGACEM, 2011), as schematically presented below:

$$[(CH_3O)_3Si(CH_2)_3N(CH_3)_2(CH_2)_{17}CH_3]Cl + 3H_2O \rightarrow [(OH)_3Si(CH_2)_3N(CH_3)_2(CH_2)_{17}CH_3]Cl + 3CH_3OH$$

This equation is valid for a complete hydrolysis without subsequent condensation. Notably, the process modifies the atomic concentration of carbon in the molecule, and the concentration ratio [C]/[N] can be used as a stoichiometry-based indicator. The [C]/[N] value expected for pristine DMOAP is 26, and for homogeneously composed fully hydrolysed DMOAP is 23. The respectively observed values are 26.9 and 23.2. Details about the bulk and water exposed DMOAP are presented in the C1s high-resolution spectra in Fig. 7 and 34, in the ESI.

Figure 7 – XPS C1s high-resolution spectra for DMOAP, (a) bulk, (b) water exposed, and (c) heated blot

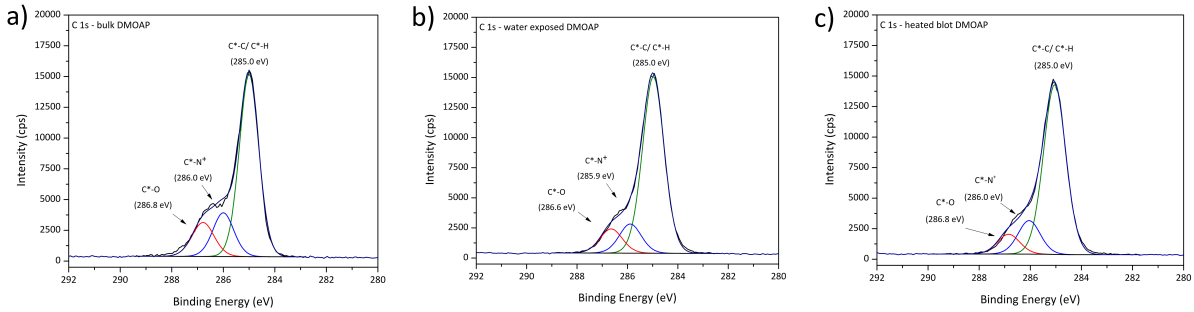

Source: Developed by the author

The binding energies of signal contributions from expected species in C1s spectra for bulk DMOAP were adjusted based on the carbon covalent binding neighbourhoods and considering the suggested binding energy ranges of the expected binding neighbourhoods as compiled by Beamson and Briggs (BEAMSON, 1993). Following this, three distinct binding energies for C1s signal contributions were considered, corresponding to aliphatic C*– C/C*–H (285.0 eV), quaternary ammonium-related C*–N^+ (286.0 eV), and C*–O in methyl ester groups (286.8 eV) (see Fig. 7). Significant signal contributions from possible carbon species with binding energies higher than 287 eV were not detected.

For a completely hydrolysed DMOAP material, a conversion of the C*–O groups is expected, coinciding with a decrease of the atomic concentration of C*–O from the stoichiometrically expected value 9.38 at% or the measured value of 11.74 at% (non-hydrolysed DMOAP) to 0 at%. However, for [C*–O] of the water-exposed sample, a value of 8.38 at% was found. The minor changes observed for the surface composition suggest a partial hydrolysis caused by water exposure of the DMOAP material after evaporation of the alcoholic solvent. Similarly, the XPS obtained for the thick DMOAP film dried and heated at 100℃ in air found small effects on the material composition and, notably, a slight decomposition of methoxy species resulting in a decrease ofthe [C*–O]/[C*–N^+] concentration ratio as presented in Table 5.

Table 5 – Concentration ratios obtained from fitting C1s signals of DMOAP bulk samples prepared following different processes.

Sample name	[C*-O]/[C*-N^+] ratio
Vacuum-dried from solution	0.8
Water exposed	0.8
Thick film after conditioning at 100℃ in air	0.6

Source: Developed by the author

Subsequently, structural implications of the spectroscopic outcomes will be highlighted. Considering the stoichiometric composition of DMOAP, hydrolysis is expected to be revealed by decreasing the [Si–O*]/[Si*–O] concentration ratio starting from a value of three.

The measured value for bulk DMOAP agrees with this expected value. After the water treatment, the value reduced to two, indicating a partial oligomerization of DMOAP molecules due to a condensation following the partial hydrolysis of the methoxysilane moieties. However, the C1s peak shape analysis indicates that a substantial portion of the methoxysilane groups were not hydrolysed.

This finding implies that the chemical inertness of the reactive head group of amphiphilic DMOAP is attributed to the formation of DMOAP micelles in water and to the sterically restricted accessibility of methoxysilane groups for water molecules. Head groups inside micelles may be screened from water by the aliphatic octadecyl tails. Similarly, the formation of ordered structures upon hydrolysis of C_{12}–C_{18} triethoxy(alkyl) silanes was reported by (SHIMOJIMA; SUGAHARA; KURODA, 1997). Even in acidified solution of ethanol-D6 and deuterated water CD_3CD_2OD : D_2O, 80 : 20 w/ w, trimethoxysilanes without amino groups and especially tri-methoxy (7-octen-1-yl) silane (OEMS) required several hours to present significant hydrolysis, as (SALON et al., 2008) reported.

A covalent attachment of methoxysilane groups to a titania surface requires the formation of a Si–O–Ti bond starting from a hexagonally coordinated Ti centre. Although the formation of Si–O–Ti bridges is established starting from tetrahedrally coordinated tetraalkoxy compounds under sol–gel conditions, the evidence for the formation of Si–O–Ti bonds starting from titania surfaces is based on hydrosilanes or chlorosilanes rather than alkoxysilanes (FERREIRA-NETO et al., 2019; GUNJI; KASAHARA; ABE, 1999; REN et al., 2008). Starting from a long-chain alkyltrialkoxysilane, such as octadecyltriethoxysilane (ODS) on zinc oxide surfaces, the formation of Si–O–Si was reported to dominate the formation of Si–O–Zn bonds, leading to a cross- linked siloxane network that adheres on the substrate surface via hydrogen bonding or with few anchoring points along the surface (TORUN et al., 2017). Interestingly, acidic properties of both zinc oxide and titania are related to Lewis acid surface sites rather than to Bronsted sites (REN et al., 2008; LIU; TABORA; DAVIS, 1994). The complexation of the acidic substrate surface sites with oxoanions or esters may be driven by Lewis basic electron pair donor properties of the respective adsorbent providing the oxo-bridge.

3.3.1.2 Adsorbed layers on smooth titania substrates

High-resolution XPS spectra of sputter-deposited titanium dioxide are displayed in Fig. 8. The Ti2p spectrum was characterised by one doublet showing a B.E. of 458.5 eV for the $Ti2p_{3/2}$ peak, as expected for titania (MOULDER, 1993). The O1s signal presented two contributions attributed to oxidic oxygen from the titanium dioxide centred at 529.9 eV and organic oxygen/hydroxyl groups at 531.6 eV (THEILE-RASCHE et al., 2020; LANDOULSI et al., 2008). The C1s signal presented four contributions, aliphatic carbon at 285.0 eV, and further contributions at 286.6 eV and 288.7 eV that are also attributed to adventitious carbon

in a sorption layer. Finally, in view of the nitrogen species accompanied by an N1s signal with a binding energy of 400.1 eV, a minor contribution of moieties containing organic nitrogen at 285.9 eV was considered (THEILE-RASCHE et al., 2020; LANDOULSI et al., 2008).

Figure 8 – XPS high-resolution spectra for sputtered titanium dioxide, (a) Ti2p, (b) O1s, (c) C1s and (d) N1s signal.

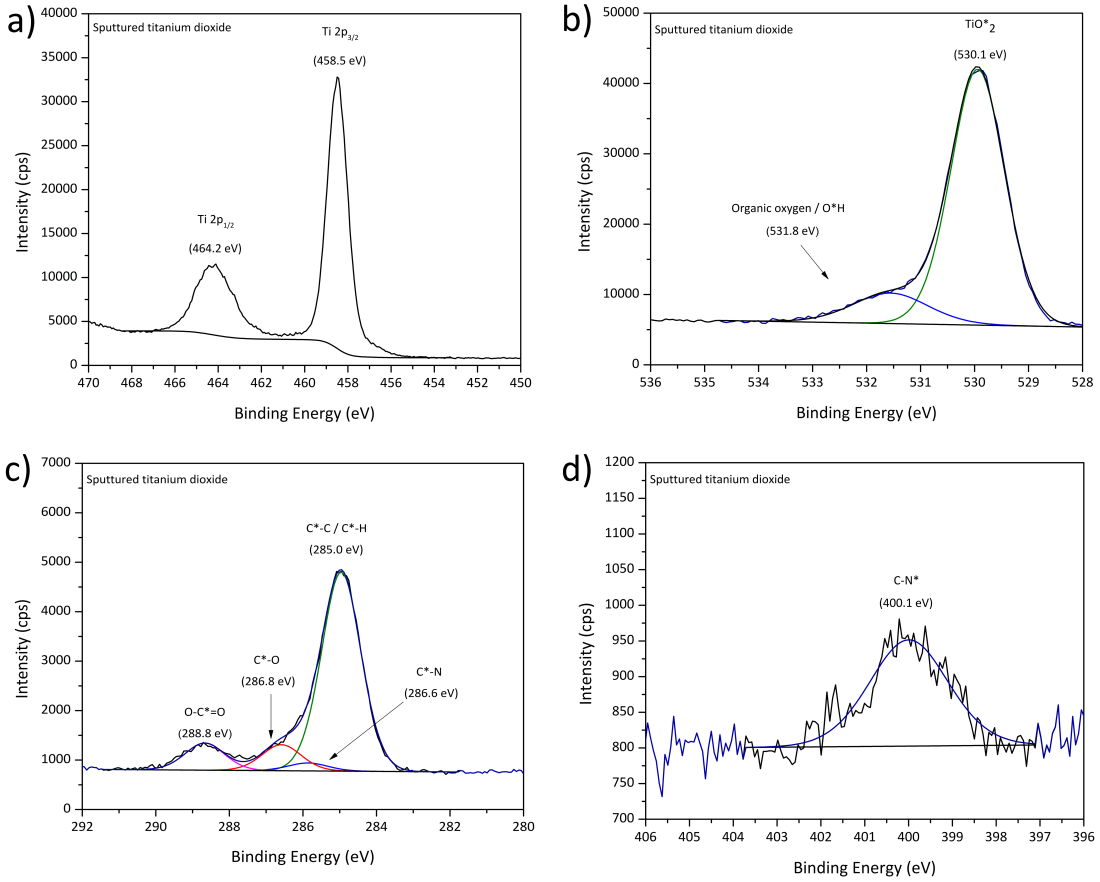

Source: Developed by the author

3.3.1.2.1 ODPA/titania films

Films assembled on these substrates from clear ODPA formulations were used as reference for a well-ordered monolayer with their structure widely studied over the years on polar oxide surfaces like alumina, silica, or titanium aluminium alloys (THEILE-RASCHE et al., 2020; GOUZMAN et al., 2006; HOQUE et al., 2006). Theile-Rasche *et al.* recently reported photoelectron spectroscopic peculiarities in C1s spectra of ODPA SAMs on $Ti_{0.5}Al_{0.5}N$ hard coatings. Therefore, a more detailed approach for the XPS signal fitting was pursued. As a reference for the C1s and O1s signals of ODPA-based assemblies, the spectra obtained for bulk ODPA were used. The correspondingly fitted signals of the most relevant studied film samples are displayed in Fig. 9, and further findings are presented in Fig. 34. For the adsorbate obtained after 4 h immersion and subsequent rinsing with ethanol, the C1s signal displayed in Fig. 9a was dominated by the contribution from aliphatic carbon species (with a

binding energy of 285.0 eV) and showed a contribution provided by C*–P bonded carbon atoms.

Figure 9 – High-resolution C1s and O1s XPS spectra obtained for ODPA layers on titania after immersion in ODPA solution for 4 h (a) and (c); 24 h (b) and (d).

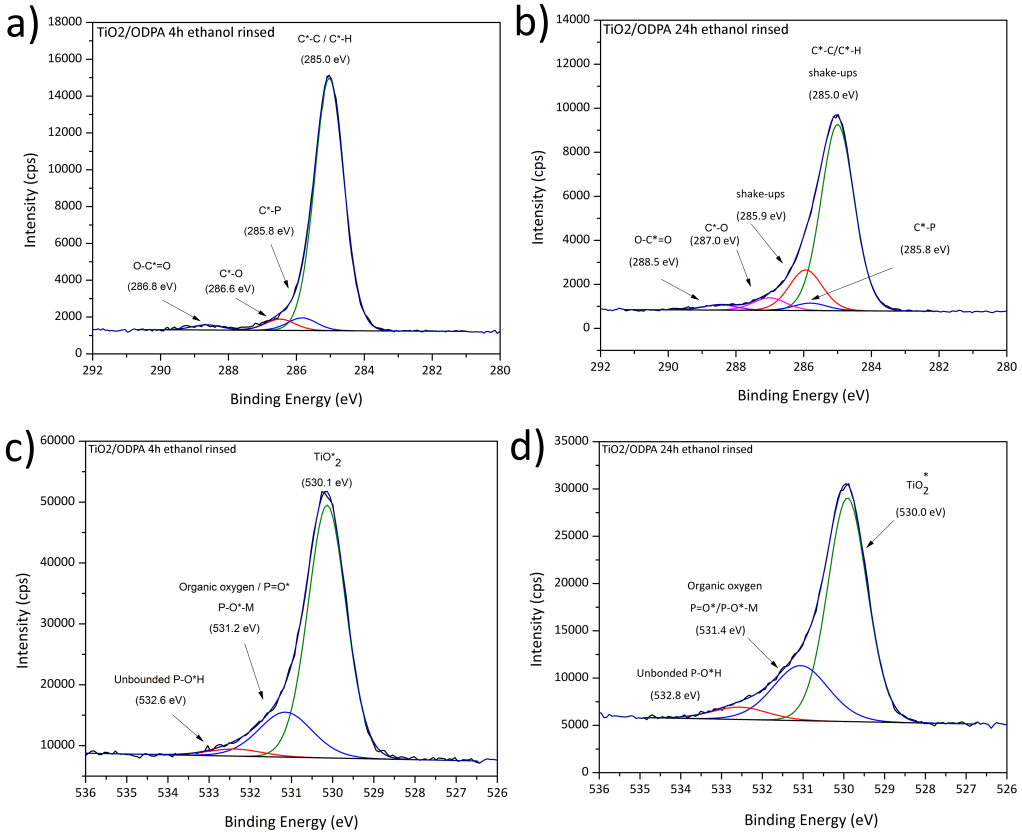

Source: Developed by the author

Comparing the respective spectra obtained for sputter-deposited titania and for the TiO_2/ODPA films prepared by 24 h immersion and subsequent rinsing with ethanol (Fig. 9b), there is clear reduction of the carboxylate adsorbed on the surface. However, indications for adventitious carbon species like C*–O (at 286.6 eV) and carboxylates (at 288.7 eV) were still observed as well as a contribution of organic nitrogen at 285.9 eV (THEILE-RASCHE et al., 2020; LANDOULSI et al., 2008). The O1s signal presented two contributions with the peaks centred at 529.9 eV and 531.6 eV (Fig. 9c and d). This indicates a partial competitive desorption of adventitious carbon moieties due to the formation of specifically adsorbed ODPA films. However, a thorough replacement of adsorbed carboxylate species was observed only after considerably longer immersion periods. In detail, when the immersion time was increased from 4 h to 24 h, a significant raise of the ODPA coverage on titania by approximately 70% (as shown in Table 6) was found; however increasing the immersion time to 72 h did not result in a further raise of the ODPA surface coverage. Additionally, the increase of the layer thickness reached a maximum value of 1.5 nm, consistent with a monolayer formation (MCINTYRE et al., 2005). Along with the compaction of the ODPA layers when extending the exposure in ODPA solution to 24 h, the C1s signal became

wider and asymmetric, displaying additional features, as depicted in Fig. 9b. These spectral features, as shown in Fig. 9b, may be related to vibrational shake-ups. This observation is consistent with the formation of a self-assembled monolayer structure, as reported by (THEILE-RASCHE et al., 2020) who suggested components at 285.4, 285.8, and 286.4 eV due to vibrational shake-ups similar to the ones reported for polyethylene.

Table 6 – Normalized XPS signal intensity ratios for ODPA samples adsorbed on titania, based on the sample immersed for 24 h in ethanolic ODPA solution and then rinsed with ethanol (subsequently labelled “SAM”), and estimated layer thickness

Sample name	{[P]/[Ti]}/{[P]/[Ti]}$_{SAM}$	{[C]/[P]}/{[C]/[P]}$_{SAM}$	Estimated layer thickness (nm)
TiO_2/ODPA 4 h EtOH	0.58	0.47	0.4
TiO_2/ODPA 24 h EtOH	1.00	1.00	1.5
TiO_2/ODPA 72 h EtOH	1.00	0.71	1.3
Bulk ODPA	-	0.71	-

Source: Developed by the author

In contrast to ODPA adsorbates rinsed with ethanol, the film surfaces of equally immersed but water rinsed ODPA/titania specimens presented a signal shape similar to the investigated ODPA bulk sample indicating the presence of physisorbed ODPA species on the surface of the assembled layer.

Following the applied XPS-based strategy for assessing details related to the bonding situation of the adsorbed species, the O1s spectral region was investigated in more detail. Aside from the two peaks fitted to encompass the contributions in case of the pristine titania, the O1s high-resolution signals obtained for thicker water-rinsed ODPA films revealed a further spectral and, thus, chemical feature contributing to a third peak at a higher binding energy around 532.7 eV, as presented in Fig. 9c and d. The concentration ratio [P=O*]/[P–O*H] did not agree with the value of 0.5 found for bulk ODPA. This finding may be due to remaining water trapped close to the polar titania substrate surface or to contributions from the phosphonate species in the underlying ODPA/titania monolayer. Both discussed samples presented a peak at 530.0 and 530.1 eV due to oxidic oxygen species from titania, which indicates that contributions from the film/substrate interphase were also recorded. The second contribution centred at 531.1–531.4 eV is attributed to organic oxygen, P=O* and P–O*–metal ion bonds (THEILE-RASCHE et al., 2020; MILOšEV; METIKOš-HUKOVIć; PETROVIć, 2012; LANDOULSI et al., 2008). In prior studies of films formed from phosphonic acids, contributions resulting in O1s peaks with higher binding energies than 532 eV were tentatively attributed to unbonded phosphonic acid P–O*H groups (THEILE-RASCHE et al., 2020). A lower surface concentration from unbound groups suggests the presence of physisorbed octadecylphosphonic acid. However, the ODPA/titania film obtained after 24 h of immersion and subsequent ethanol rinsing still exhibited a high-binding energy contribution in the O1s spectrum. As AFM investigations of this sample surface did not reveal significant rises, such as patches or physisorbed ODPA micelles (as shown in Fig. 12). This

finding may indicate that the chemisorbed ODPA is attached to the surface through tri and bi- dentate bounds rather than mono-dentate. Similar XPS findings were not detailed by (THEILE-RASCHE et al., 2020), which may be due to the intense O1s signal contributions of the mixed oxide layer of the $Ti_{0.5}Al_{0.5}N$ coating they investigated. Due to the predominance of a mono-dentate conformation, a higher contribution of unbound groups may be expected, leading to similar O1s contributions, as observed for the investigated bulk ODPA specimen. The observed $P2p_{3/2}$ binding energy is consistent with the values reported for immobilized phosphonates in the literature (see Fig. 34 and 35) (ROJO et al., 2016; CICCO et al., 2019).

3.3.1.2.2 DMOAP/titania films

The XPS findings for the investigated DMOAP/titania films are summarised in Table 7, displaying the detected elements and the contributions of the attributed chemical species.

Table 7 – Atomic concentration in at% of the distinct surface species from XPS investigations of DMOAP/titania films

	[C]					[O]			[N]		[Si]	[Ti]	[Cl]
Sample name	[C*-C/C*-C]	[C*-N^+]	[C*-O]	[C*-N]	[O-C*=O]	[TiO^*_2]	[Organic oxygen/O*H]	[Si-O*]	[C-N*]	[-N^{*+}]	[O_3Si^*-C]	[TiO^*_2]	[Cl^-]
TiO_2/DMOAP-A 10 min heated	25.04	3.25	2.29	0.75	2.38	36.38	6.82	1.09	0.76	0.84	1.85	17.64	0.47
TiO_2/DMOAP-N 10 min heated	17.71	2.43	1.55	0.65	2.04	41.35	7.53	0.86	0.61	0.62	1.27	12.22	0.00
TiO_2/DMOAP-N 24 h heated	36.85	1.66	3.19	1.10	2.64	27.91	5.40	3.98	1.05	0.43	2.47	13.22	0.08
TiO_2/DMOAP-N 24 h	38.56	1.54	4.13	1.35	3.70	22.84	5.12	6.60	1.35	0.41	1.63	12.22	0.00

Source: Developed by the author

The fitting procedures applied to the spectrum sets of all samples were based on those used for the pristine titania and the bulk DMOAP samples. The binding energy positions observed for all adsorbate signals, in case of all samples, are consistent with the species expected for an adsorbed layer of DMOAP (THEILE-RASCHE et al., 2020; BEAMSON, 1993; LANDOULSI et al., 2008). High-resolution Si2p spectra for all the considered DMOAP/titania samples included a centrosymmetric peak with a binding energy between 101.5 and 102.3 eV (see Fig. 10 and 36), consistent with the presence of groups with a –C–SiO_3– binding environment of the silicon atoms on the surface (DIETRICH et al., 2016; ZARRIN et al., 2015). N1s spectra are presented in detail in Fig. 10. Compared to pristine titania, DMOAP/titania exhibited an additional peak at higher binding energy, consistent with the presence of quaternary ammonium according to the species of the carbon signal, and with the bulk sample (HE et al., 2016; ZARRIN et al., 2015; TANG et al., 2016). There is no significant difference between the shapes on the acidified and the neutral medium, not even on the heated and unheated samples. The C1s high-resolution spectrum of the sample immersed for 24 h is displayed in Fig. 10a. The peak with a binding energy of 286.0 eV is attributed to contributions from C*–N^+ species. In the frame of the fitting procedure, an area constraint was applied for this contribution to ensure a reasonable value based on DMOAP stoichiometry showing a C_4N^+ binding environment.

Remarkably, the C1s signal for all these samples revealed contributions around 288.5 eV, attributed to carboxylate species. Following the rationale established for ODPA/titania

Figure 10 – XPS high-resolution spectra for DMOAP layer on titania, (a) C1s, (b) O1s, (c) N1s and (d) Si2p signals.

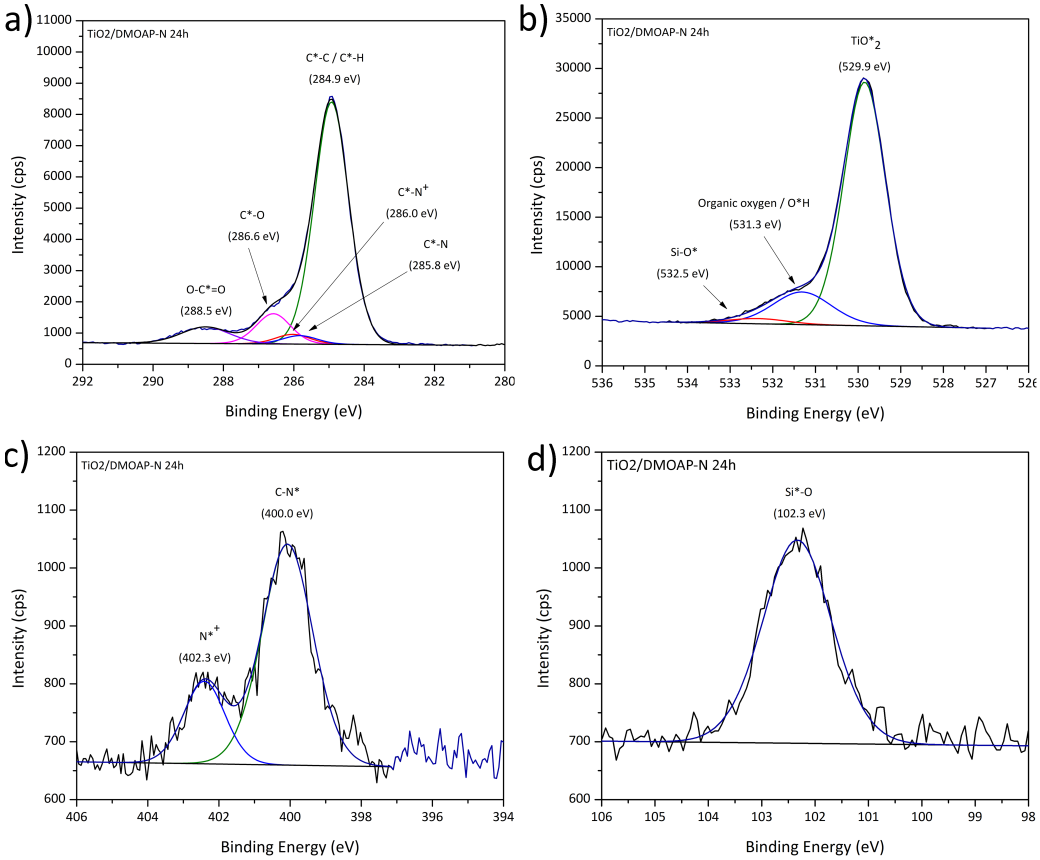

Source: Developed by the author

films, this finding indicates that the DMOAP species do not competitively adsorb on the titania surface to form a chemisorbed monolayer structure. Moreover, C1s shake-up contributions, as observed for the ODPA/titania monolayers, were not found. Three species were detected in the O1s spectra for all samples, as illustrated in Fig. 10b. The contribution centred at approximately 532.5 eV is due to Si–O* bounds, consistent with the Si2p signal and the findings for DMOAP bulk samples (BEAMSON, 1993; LANDOULSI et al., 2008; SANTOS et al., 2015). Although the samples prepared in different medium show similar signal shapes, the silanol contribution clearly increased after the heat treatment along with a decrease of the contact angle, as presented in Table 9.

In Table 8, the estimated layer thickness and different ratios for the investigated samples normalized for the TiO_2/DMOAP-N 24 h sample are displayed. Heating a film in air at 100 °C did not modify the film thickness. However, the normalised [C]/[Si] ratio was affected by performing the annealing process. This is highlighted for the TiO_2/DMOAP-N 24 h sample. On the one hand, the [C]/[Si] found for the dried sample was equal to the respective ratio of the bulk sample. This is attributed to the absence of a preferential molecular orientation perpendicular to the sample surface in both cases. On the other hand, the heated film sample showed a considerably decreased [C]/[Si] concentration ratio. This result indicates that the

annealing procedure induces a preferential orientation, which leads to higher exposure of the silanol groups close to the film surface. The concomitant increase of the [Si]/[Ti] ratio is in concordance with modification of this layer.

Table 8 – Normalized atomic concentration ratios for freshly prepared DMOAP films on titania surfaces as obtained by XPS and referencing the findings for the DMOAP-N/titania films obtained after 24 h immersion (labelled “DMOAP-N 24 h” here)

Sample name	{[Si]/[Ti]}/{[Si]/[Ti]}DMOAP$_{-N24h}$	{[C]/[Si]}/{[C]/[Si]}DMOAP$_{-N24h}$	Estimated layer thickness (nm)
TiO_2/DMOAP-A 10 min heated	0.8	0.6	0.9
TiO_2/DMOAP-N 10 min heated	0.8	0.6	0.6
TiO_2/DMOAP-N 24 h	1.0	1.0	1.8
TiO_2/DMOAP-N 24 h heated	1.4	0.6	1.7
Bulk DMOAP vacuum dried	-	1.0	-

Source: Developed by the author

As XPS is a surface-sensitive technique and some preferential molecular orientation may introduce a nanoscale structural anisotropy in films, these findings may be expected to sensitively reflect such geometric effects. Therefore, the difference found between the signal intensities of the heated and unheated samples, which were coated in concordant processes establishing coincident surface coverages, suggests that the heat treatment rearranges the adsorbed layer.

3.3.1.2.3 Comparing ODPA/titania DMOAP/titania films

Finally, in the headgroup densities of ODPA/titania and DMOAP/titania films prepared by 24 h immersion in alcoholic solutions and subsequent rinsing with ethanol, the [Si]/[Ti] concentration ratio amounting to 0.14 is 1/3 higher than the [P]/[Ti] concentration ratio for the ODPA monolayer. In addition to the strong headgroup attachment facilitating competitive desorption of carboxylic adventitious carbon species and the highly ordered film structure resulting in C1s shake-ups, this finding substantiates that although these films exhibit similar thickness their assembly schemes have significant differences. This is also reflected when considering the respective differences with respect to the surface concentrations of the bulk samples, revealed by values around 1 and 0.6 for [C]/[Si]$_{bulk}$/[C]/[Si]$_{DMOAP-N,24h}$ and [C]/[P]$_{bulk}$/[C]/[P]$_{SAM}$, respectively. Evaluating the relative XPS signal contributions from atoms in head and tail group for bulk or film specimens, respectively, may be considered an effective approach to and orientational differences of amphiphilic species in the distinctly assembled phases.

3.3.2 Contact angle measurements

The layer modification can be noticed also by the decrease of the water contact angle after the heating procedure (as shown Table 9). Since DMOAP and ODPA have long alkyl chain (octadecyl tails) and a minor solubility in water, the presence of the adsorbates on the surfaces can be verified by contact angle measurements. Surfaces terminated by

methylene $–CH_2$ and methyl $–CH_3$ groups were reported to present a water contact angle (WCA) higher than 90° (D'ELIA et al., 2009). Nonetheless, immediately after its preparation and a few minutes in contact with ambient air the sputter-deposited titania displayed a low WCA. Thus, for both DMOAP and ODPA films on titania, a significant increase is expected in the contact angle due to these amphiphiles adsorption. The results of measured contact angle for the freshly prepared titania and the films after the adsorption of DMOAP and ODPA are summarized in Table 9.

Table 9 – Contact angle results for DMOAP and ODPA films on smooth titania (freshly prepared

Sample name	Water contact angle (°)
TiO_2	11.4 ± 3.5
TiO_2/DMOAP-N 10 min	80.0 ± 0.9
TiO_2/DMOAP-A 10 min	86.8 ± 0.9
TiO_2/DMOAP-N 10 min heated	65.1 ± 0.8
TiO_2/DMOAP-A 10 min heated	63.1 ± 3.0
TiO_2/DMOAP-N 24 h	82.3 ± 2.5
TiO_2/DMOAP-A 24 h	85.4 ± 0.4
TiO_2/DMOAP-N 24 h heated	48.8 ± 1.1
TiO_2/DMOAP-A 24 h heated	48.3 ± 0.4
TiO_2/ODPA, 4 h EtOH rinsed	99.5 ± 0.5

Source: Developed by the author

The observed increase of the WCA for the ODPA and DMOAP-N 24 h flms on titania indicated that the surface is mainly terminated by $–CH_2$ and $–CH_3$ groups (D'ELIA et al., 2009). Such effect of film formation was corroborated by the XPS results, which were obtained after 24 h immersion of titania substrates in ODPA or DMOAP containing formulations, and indicate the presence of aliphatic carbonaceous species on the surface. The contact angle strongly decreased due to the heating procedure indicating an alteration of the adsorbed layer, as presented in Table 9.

Such modifications are comparable to the results presented by (D'ELIA et al., 2009) who demonstrated the influence of the film formation temperature on the thickness and contact angle of DMOAP layers on oxidic ITO thin films. After the heat treatment at 120°C, the contact value was near 67°, and similar results were obtained in our study. Following a heat treatment at 100 °C, the WCA findings displayed in Table 9 were 64° for samples immersed for 10 minutes and 48° for samples immersed for 24 hours. D'Elia *et al*. explained the contact angle reduction in the case of DMOAP/ITO films due to a disordering of the DMOAP layer induced by the heat treatment. Those authors stated that lower drying temperatures (about 85 °C) are suitable for the formation of ordered DMOAP monolayers.

The measured WCA value for the ODPA layer presented in Table 9 agreed with the literature and indicated the presence of a layer on TiO_2 surface. Chen *et al*. reported a WCA between 90° and 110° according to the concentration of ODPA adsorbed on aluminium

(CHEN et al., 2014). Further studies also showed water contact angles higher than 100° for adsorbed ordered ODPA (DAI et al., 2014; HOQUE et al., 2006).

3.3.3 Zeta potential measurements

Zeta potential investigations are mainly performed on colloidal suspensions of different materials (FERRARIS et al., 2018). In this case, different factors can modify the zeta potential values and the isoelectric point; for instance, the particle size, roughness, and crystalline phase of materials prevailing in distinct modifications, such as titania (BORGHI et al., 2013; SUTTIPONPARNIT et al., 2011). Besides the investigation of differently modified titania surfaces, the approach presented in this work was done using a smooth substrate to avoid the influence of roughness on the measurement. Thus, the results are mostly influenced by the adsorbed species on the surface.

The results of these measurements are displayed in Fig. 11. Pristine titania samples presented a plateau between pH 6.0 and 8.0. Ferraris and co-workers who investigated different Ti6Al4V surfaces reported similar results for a chemically treated sample (FERRARIS et al., 2018). The occurrence of such plateau was attributed by Ferrari *et al.* to the presence of acid hydroxyl groups. The OH groups terminating the titania surface were also revealed by the XPS findings, reinforcing this explanation as presented in Fig. 8. The zeta potential results displayed in Fig. 11 show, apart from the DMOAP/titania sample immersed for 10 minutes, an increase of the zeta potential after adsorption of DMOAP. Although it is difficult to quantitatively compare trends of zeta potential measurements obtained for samples in such different geometries as powders and films, in this study, a zeta potential shift towards more positive values was also observed for quaternary ammonium-containing molecules adsorbed on membranes compared to bare membranes (ZHAI et al., 2020; LIU et al., 2020; YANG et al., 2020). Such shift caused by the presence of quaternary ammonium agrees with the XPS outcomes that showed the presence of C–N^+ in DMOAP/ titania films obtained after immersion in DMOAP solution. Moreover, as presented in Fig. 11, ODPA adsorbed on titania shifted towards lower zeta potential values, in qualitative agreement with reported studies of ODPA adsorbed on different materials (OUEINY et al., 2016; QUIñONES et al., 2017). The shift of the zeta potential at basic pH was possibly due to unbonded P–OH groups, which will be investigated in more detail.

3.3.4 AFM investigations

The layers obtained by self-assembly of ODPA and adsorption of DMOAP on the surface of sputter-deposited titania films on flat and smooth silicon wafers were investigated by AFM and evaluated in comparison with the pristine substrate. The surface root mean square (RMS) R_q of the surface roughness obtained by AFM for TiO_2/Si film was 0.41 nm. As illustrated in Fig. 12, the surface of an uncoated TiO_2/Si substrate revealed a homogeneous

Figure 11 – Zeta potential results for the studied layers on smooth titanium dioxide.

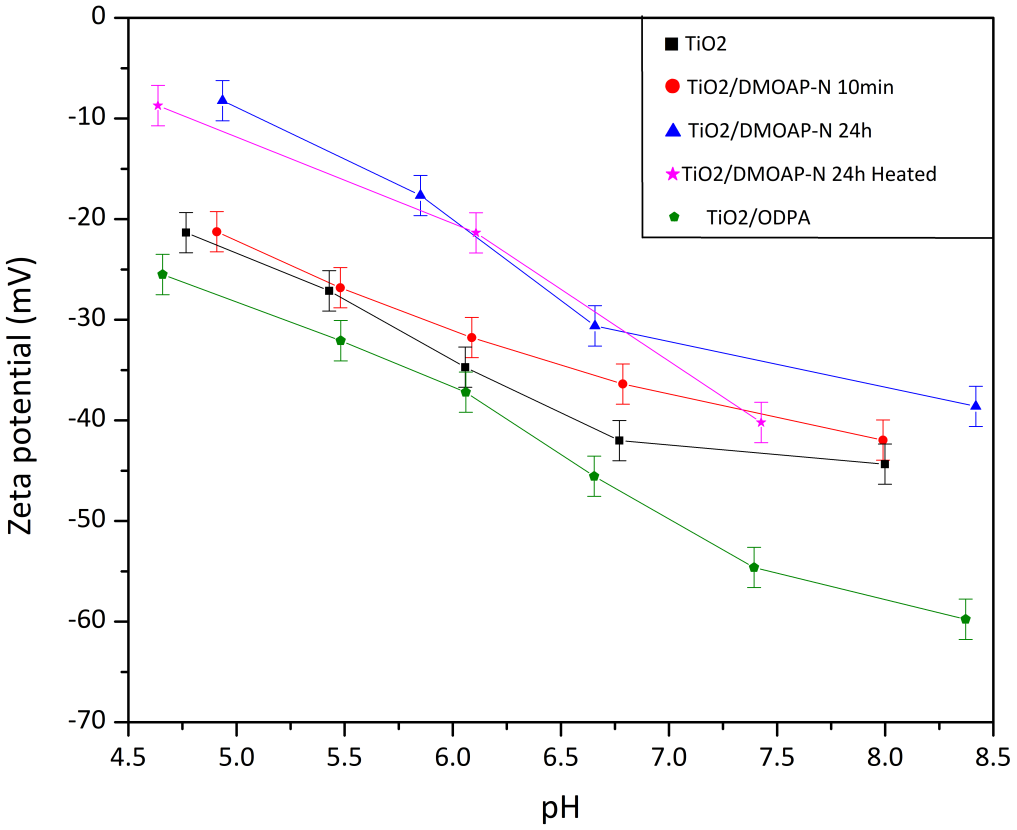

Source: Developed by the author

and smooth topography characterized by imaged height differences with the range of up to 3 nm. Upon interaction with the AFM tip, the most pronounced risings with heights around 3 nm exhibit distinct adhesion properties, from the surrounding smooth substrate areas, and are attributed to particulate deposits.

Subsequently, we assessed the microscopically characterized surface properties achieved by 24 h of immersion in alcoholic solutions of separate amphiphiles ODPA or DMOAP and subsequent sample conditioning steps with distinct rinsing or mild heating procedures.

After immersion in ODPA-containing ethanolic solutions and subsequent rinsing with the solvent, the obtained TiO_2/ODPA sample displayed height differences with a range of up to 7 nm and a R_q roughness of 1.1 nm. The most pronounced risings with heights around 7 nm had distinct adhesion properties from the surrounding smooth substrate areas. As their areal density is higher than that of the pristine substrates, they are attributed to particulate deposits obtained during the process chain comprising immersion and rinsing steps.

In contrast, when rinsed with water after the immersion, an increased R_q roughness, around 4.2 nm was observed along with patch-like deposits with a width of approximately 0.1 mm. On the upper right area, the R_q was 2.4 nm, and on the lower left area, 6.7

Figure 12 – AFM height and adhesion force image for the investigated layers.

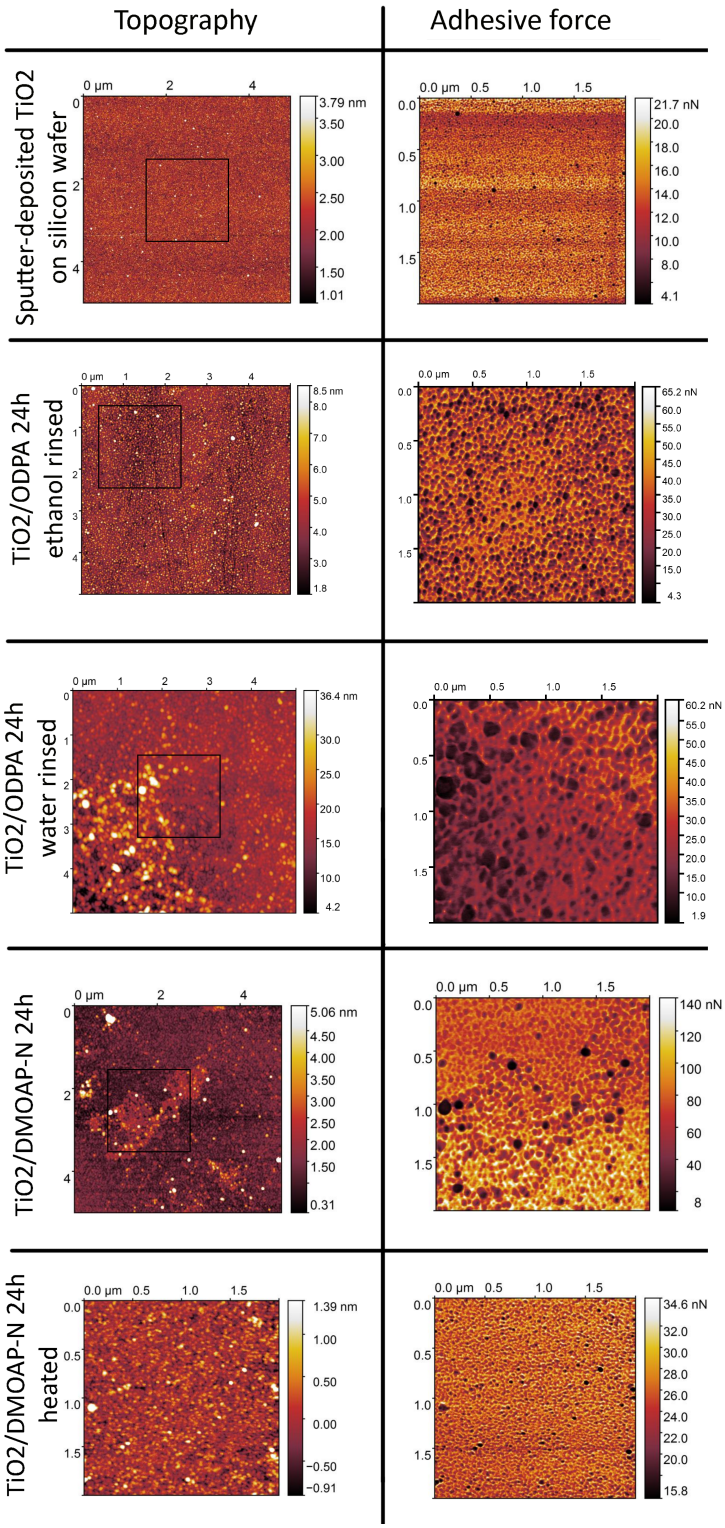

Source: Developed by the author

nm. The differences in topography and adhesion properties as compared to the pristine substrate surfaces are attributed to the formation of adsorbates and to local deposition of surplus organic material. For its areal density, less than 10% of the imaged surface area is significantly lower when rinsed with ethanol than that exposed to water during rinsing.

After immersion in DMOAP-containing ethanolic solutions and subsequent rinsing with water, the obtained TiO_2/DMOAP- N sample displayed height differences up to 2 nm and a R_q roughness of 0.35 nm. After the sample was exposed to a heating process at 100℃ in air overnight, the obtained TiO_2/ DMOAP heated samples revealed an increase in roughness of 0.69 nm and imaged height differences up to 5 nm. The findings obtained by SFM investigations of ODPA/titania films along with the XPS results indicate the formation of ODPA/titania SAMs after rinsing with ethanol and the deposition of thicker ODPA/titania films composed of octadecylphosphonic acid on top of an ODPA/titania SAM when rinsed with water instead. For the thin DMOAP/titania film, the roughening of the film surface and the occurrence of elevated patch regions with distinctive adhesion properties are interpreted to result from the thermal conditioning process.

Fig. 13 presents the height profile for sputtered titania and the SAM of ODPA. The profile shows a difference caused by the physisorbed ODPA species on the surface of the assembled layer, consistent with the aforementioned discussion. This finding may point to ODPA micelles on the SAM surface. The formation probably occurred during the washing procedure because ODPA is only poorly soluble in water. Such geometric film model explains the occurrence of approximately 5 nm height nanoscale risings as observed in the AFM images presented in Fig. 13.

Figure 13 – AFM height profile of (a) sputtered titanium dioxide and (b) ODPA monolayer.

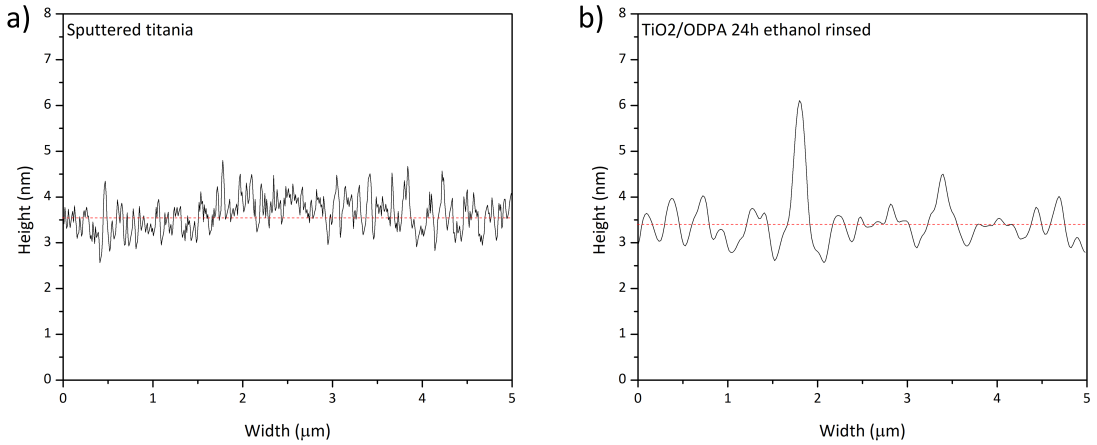

Source: Developed by the author

3.3.5 Antibacterial assays

Antibacterial assays were performed to evaluate how the studied samples respond to bacterial agents. In the antibacterial assay against *S. mutans*, the thick DMOAP bulk film presented greater antibacterial activity than the other investigated specimens, which became evident mainly after 24 hours (Fig. 14).

To check the efficacy of the prepared surface modified titania samples in longer

Figure 14 – *S. mutans* growth after exposition to different samples during three different periods.

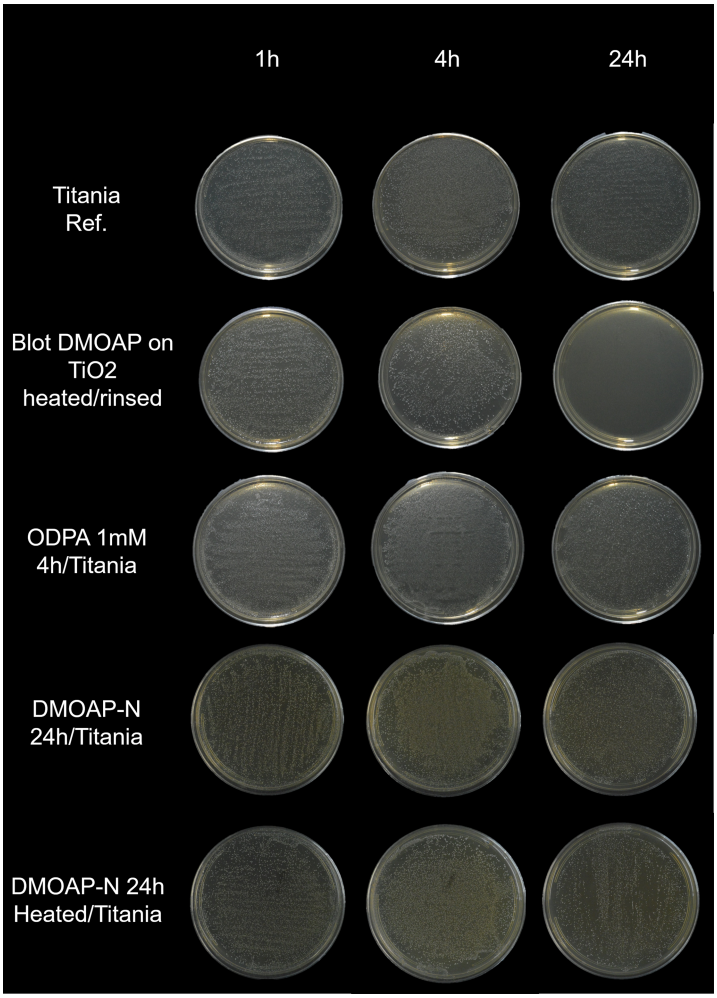

Source: Developed by the author

exposure, adsorbed layers of ODPA and DMOAP were submitted to a test using *E. coli* for 24 hours. The statistical analysis is displayed in Table 10. All groups showed the same pattern: low growth at the beginning and an intermediate growth in the end of the evaluated time. No surface treatment provided an effective reduction of the bacteria growth compared to the control (TiO_2). The TiO_2/DMOAP-A 24 h group had a more pronounced bacteria growth than the control, which was not expected. The value p is lower than 0.05 for the maximum and final time, showing that the samples are significantly different, but not due to the reduction of the bacteria, as aforementioned. A decrease in bacteria growth was not observed compared to the control.

Although DMOAP antibacterial properties have been reported in different studies, there was a strong modification on the surface wettability after the biological assay, indicating that during the incubation period DMOAP layers are partially removed. This statement is based on the water contact angle measurements presented in Table 11 that reveal the changes of the WCA during the antibacterial test.

Table 10 – Mean (SD) findings of *E. coli* growth attached to sample surface in 24 h[a]

	Time evaluation		
Treatment group	Initial	Maximum	Final
TiO_2	0.099 (0.2 x 10^{-2}) Ca	0.442 (0.03) Ab	0.287 (0.07) Bb
TiO_2/DMOAP-A 10 min	0.100 (0.6 x 10^{-2}) Ca	0.445 (0.05) Ab	0.346 (0.03) Bab
TiO_2/DMOAP-A 10 min heated	0.102 (0.7 x 10^{-2}) Ca	0.491 (0.03) Aab	0.394 (0.03) Bab
TiO_2/DMOAP-A 24 h	0.096 (0.07 x 10^{-2}) Ba	0.512 (0.03) Aa	0.430 (0.06) Aa
TiO_2/DMOAP-A 24 h heated	0.101 (0.5 x 10^{-2}) Ca	0.460 (0.05) Ab	0.334 (0.5 x 10^{-2}) Bab
TiO_2/DMOAP-N 10 min	0.098 (0.09 x 10^{-2}) Ca	0.494 (0.02) Aab	0.356 (0.03) Bab
TiO_2/DMOAP-N 10 min heated	0.096 (1.1 x 10^{-2}) Ca	0.481 (0.01) Aab	0.360 (0.04) Bab
TiO_2/DMOAP-N 24 h	0.104 (1.1 x 10^{-2}) Ca	0.545 (0.04) Aa	0.413 (0.06) Bab
TiO_2/DMOAP-N 24 h heated	0.099 (0.4 x 10^{-2}) Ca	0.454 (0.05) Ab	0.353 (0.02) Bab
TiO_2/ODPA	0.102 (1.1 x 10^{-2}) Ca	0.461 (0.04) Ab	0.338 (0.02) Bab
p-value	*p*-value = 0.826	*p*-value = 0.026	*p*-value = 0.016

[a] Mean values followed by distinct letters differ statistically at 5%, according to two-way repeated measures ANOVA and Bonferroni test. Uppercase letters compare time evaluation within treatment group (lines). Lowercase letters compare treatment groups (columns).

Source: Developed by the author

Table 11 – Changes of water contact angles obtained for thick and thin DMOAP films on titania substrates and for ODPA/titania after 24 h exposure to bacterial medium containing *S. mutans* and subsequent rinsing with alcohol

Sample name	Water contact angle (°)
Before rinsing in isopropanol	92.8 $\pm$ 8.3
After rinsing in isopropanol	54.2 $\pm$ 8.4
After 1 h exposition in biological medium	65.4 $\pm$ 16.1
After 4 h exposition in biological medium	58.9 $\pm$ 12.3
After 24 h exposition in biological medium	55.2 $\pm$ 23.5
TiO_2/DMOAP-N 24 h heated	46.3 $\pm$ 4.2
TiO_2/ODPA, 4 h	88.6 $\pm$ 8.3

Source: Developed by the author

Notwithstanding, different characterization, *e.g.* by zeta potential measurements requiring test periods of approximately one hour, indicated the immobilization of DMOAP on the titania surfaces. However, the adsorbed layer appears strongly affected by the biological assay and is possibly released to the biological medium. Such finding suggests that following the applied immobilization scheme, the resulting DMOAP layers are significantly less stable than the assembled ODPA layers, although covalent attachment on the titania surface may be anticipated for both adsorptives. As the thick DMOAP bulk film presented the higher antibacterial activity, the activity could be influenced by the adsorbate mobility and/or release. Accordingly, Stular and co-workers reported that after several washing procedures, DMOAP was partially removed from cotton surface (ŠTULAR et al., 2017). The release of alkylorganosilanes was reported by Torun and co-workers, who revealed that alkylorganosilanes anchor by few points on ZnO surface leading to a small number of covalent bonds (TORUN et al., 2017). Thereby, well ordered DMOAP monolayers might not be suitable for antibacterial coatings since the quaternary ammonium groups are not easily accessed by the bacteria membrane.

3.4 Conclusions

The presented study aimed at providing a comprehensive experimental setup with distinct methods and scales for promoting a systematic characterization of octadecylphosphonic acid (ODPA) and dimethyloctadecyl[3-(trimethoxysilyl)propyl] ammonium chloride (DMOAP) adsorbed on smooth or structured surfaces to deliver new information about the structure–property relationships accompanying the surface modification. By applying the proposed methodology, new details were provided for the immobilization and assembly of such adsorptives on titania surfaces, starting from films on smooth oxide surfaces. The choice of the substrates provides access to physicochemical properties of such structures, which minimizes the substrate influence. ODPA and DMOAP on sputter-deposited titania were intensively characterized through different techniques. XPS characterization was performed starting from the bulk materials. After the adsorption of ODPA on titania for 24 hours of immersion and subsequent rinsing with ethanol, the C1s high-resolution spectra showed contributions consistent with a monolayer formation, presenting decrease of carboxylate on the surface. Such structure was only observed in samples prepared during longer immersion periods followed by washing with the same solvent, confirming that time and rinsing procedures play a crucial role in monolayer formation. The layer thickness of 1.5 nm reinforces the presence of a monolayer.

Well-ordered and strongly attached monolayers were not observed for distinct approaches of assessing DMOAP adsorbed on smooth titania, although different characterization indicated the presence of a layer on the surface. XPS and zeta potential measurements verified the presence of quaternary ammonium groups close to the surface. The mild heat treatment for conditioning DMOAP layers promoted a reorganization of the constituents of the films on the surface but did not significantly attach the reactive trimethoxysilyl headgroups to the titania substrate. The complete hydrolysis of trimethoxysilyl moieties moieties was identified as a challenge for the synthesis of bioactive films from dispersions composed of functional amphiphilic molecules. Congruently, sample surface characterization after the biological assays found that DMOAP layers are not stable after one day of exposure to aqueous media and could be released during the test. The fact that a several micrometres thick DMOAP film presented the highest antibacterial activity against Gram-positive *S. mutans* bacteria could be due to release from an imperfectly attached and crosslinked film and the mobility of the thus dispersed species in the bacterial medium. Thus, the preparation plays a crucial role in the activity of DMOAP layers, and a thin layer would not be suitable for an extended antibacterial activity. Likewise, the results showed that the protocols reported in the literature cannot be applied for titania surfaces.

The proposed methodology elucidates aspects of bioactive layers on titania based on the structure of the adsorbents on the surface, providing physicochemical characterization of the layers before and after biological assays. Such approach could also be applied to other

bioactive layers on variably coated substrates to provide new information about the layer properties rather than only biological activities.

3.5 Conflicts of interest

The authors declare that they do not have any conflicts of interest.

3.6 Acknowledgements

The authors are grateful to the São Paulo Research Foundation FAPESP for the financial support through the grants 2019/ 13100-0 and 2018/07520-3; Dr Welchy Leite Cavalcanti for fruitful discussions; Thorben Brenner for the assistance with the zeta potential investigations; and João Pedro Costa Rheinheimer for kindly helping with the plots. Stephani Stamboroski thanks Fraunhofer-Gesellschaft for support within the internal program Fraunhofer TALENTA start.

4 Bisphosphonates on smooth TiO_2: modeling and characterization

This chapter was originally published on *ChemistrySelect, 2022, 7, 19, e202200286* as original article, the manuscript is available through the DOI: 10.1002/slct.202200286

4.1 Introduction

Bisphosphonates (BPs) are molecular anions of organic molecules analogous to pyrophosphate (HOLSTEIN et al., 1998). Unlike pyrophosphate, BPs have a central carbon that allows the presence of two substituents (R_1 and R_2), as shown in 15 (CHEN et al., 2012). The substituent R_1 is in general a hydroxyl group, and R_2 can vary from a methyl to a nitrogen-containing heterocyclic ring. Such groups play an essential role in the biological activity of these molecules. A nitrogen-containing bisphosphonate can have a 10000 times more potent osteogenic effect than a BP containing only a methyl group (DRAKE; CLARKE; KHOSLA, 2008).This work chooses etidronic acid, alendronic acid, and risedronic acid as surfaces modifiers. These anions were considered since etidronic acid is the simplest structure for bisphosphonic acid, while alendronic and risedronic acid are nitrogen-containing BP, with a linear and cyclic nitrogen, respectively. Thus, these three molecules cover a variety of bisphosphonic acids structure.

Figure 15 – a) General structure of bisphosphonic acids and linear structure of b) etidronic acid, c) alendronic acid and d) risedronic acid.

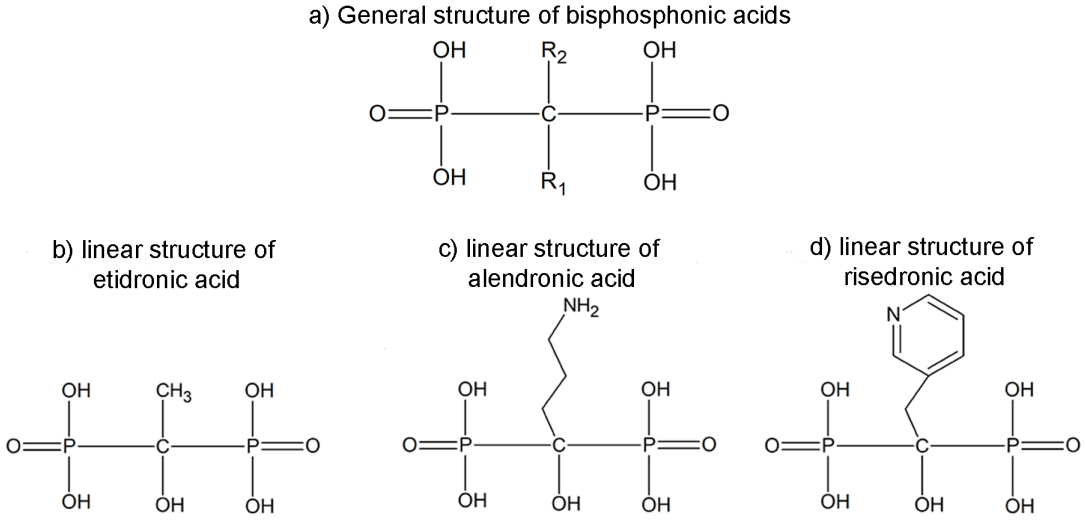

Source: Developed by the author

Although BPs have been intensely studied throughout the years, some points still

need to be clarified about their pharmacological functions and their potential as surface modifiers (ROJO et al., 2016; PETER et al., 2005). Frequently, the BPs are adsorbed on or combined with hydroxyapatite (HA), because such molecular anions have a strong affinity for HA surfaces and can coordinate Ca^{2+} (NANCOLLAS et al., 2006), to increase cell growth and proliferation of implants surfaces. Regardless of their attested biocompatibility, the production of HA surfaces is laborious, mainly on metallic substrates such as titanium alloys used as implants, screws, and plates, exhibiting a poor adhesion between film and substrate (SIDANE et al., 2017; ARIFIN et al., 2014). To avoid complications related to the film-substrate interface, the use of titanium dioxide films is a solution to explore the entire potential of immobilized bisphosphonates. Different studies present the properties of TiO_2, such as biocompatibility, corrosion resistance, and presence of hydroxyl groups, suitable characteristics for an implant cover (TRINO et al., 2018a; BRONZE-UHLE et al., 2019b; LóPEZ-HUERTA et al., 2014).

As surfaces modifiers, most studies with bisphosphonates have focused only on the biological aspects. Thus, there is a lack of information about the effects of BPs adsorption on metallic and oxidized surfaces. For example, surface energy and groups previously adsorbed on the titania surface modify the interaction between the substrate and the molecules (ZHENG; NEOH; KANG, 2017; BRONZE-UHLE et al., 2019a).

Through an X-ray photoelectron spectroscopy (XPS) and density functional theory (DFT), it was demonstrated that titanium implants functionalized with alendronate exhibit decreased contact angle. In addition, competitive adsorption takes place between two configurations: the first conformation amino (-NH_2) and phosphonic acid (-PO_3H_2) groups bound on the surface; the second occurs through phosphonic acid (-PO_3H_2) groups only (PETROVIć et al., 2020). Despite using different techniques, the influence of roughness was not mentioned in the referred study, as only one bisphosphonate was used and simulated in a vacuum.

Hence, in this work, we demonstrated the modification of surface properties caused by bisphosphonates' adsorption on smooth titanium dioxide. The choice of this specific substrate is due to its common application as an implant cover (GEETHA et al., 2009). The proposed approach was applied with the same substrate using quaternary ammonium-containing silane and octadecyl phosphonic acid (ODPA), which demonstrated the association between biological activity and layer structure (DIAS et al., 2020). The use of a smooth substrate aims to reduce the influence of the geometric surface area, which can increase the surface charge or even the interaction between layers and cells (SUTTIPONPARNIT et al., 2011; BORGHI et al., 2013; VIDYASAGAR; APSE, 2004).

In this work, bisphosphonic acids were simulated using density functional theory (DFT) to predict their properties. Different studies used DFT to explore the adsorption of BPs. Such an approach provides the HOMOs (highest occupied molecular orbital), the LUMOs

(lowest occupied molecular orbital), and the density of states, permitting the most reactive sites of the BPs to be found. Few works have considered that the molecules display different protonation and deprotonation states with the pH – important for adsorption experiments – and most of them focused on the adsorption on hydroxyapatite crystals (CHEN et al., 2012; FERNáNDEZ; ORTEGA-CASTRO; FRAU, 2017; RI et al., 2018). However, TiO_2 is also employed as an implant coating.

In this way, the performed simulations considered the different states of protonation and deprotonation, and these results were compared with X-ray photoelectron spectroscopy providing aspects of BPs adsorption. The results were complemented with water contact angle (WCA), zeta potential, and atomic force microscopy (AFM) measurements. XPS evaluated short-time immersion (2 h) and long-time immersion (24 h), samples were analyzed through other techniques, XPS investigations of overnight immersion were published elsewhere (BRONZE-UHLE et al., 2019a).

4.2 Results and discussion

4.2.1 Theoretical modeling

A reactivity study of distinctly protonated bisphosphonic acids in an aqueous solution in contact with uncharged crystalline titania surfaces was conducted to investigate whether the reactive regions are consistent with typical adsorption centers of the BP-based entities on the substrates. As BP structures are very susceptible to pH influence, molecules or ions were simulated in different protonation and deprotonation states. In pH 7, etidronic acid can undergo two or three deprotonations (FERNáNDEZ; ORTEGA-CASTRO; FRAU, 2017). Alendronate passes through one protonation and two deprotonations (FERNáNDEZ; ORTEGA-CASTRO; FRAU, 2017; KE et al., 2016). On the other hand, risedronate undergoes two or three deprotonations (BEDOYA et al., 2017). Information regarding theoretical modeling in vacuum and water for neutral bisphosphonates is available in the supplementary material.

Figure 16 the DFT results for the BP structures simulated in a water environment. In this figure, blue and red colors are both related to CAFI/MEP results and indicate positively and negatively charged sites, respectively. According to the presented RGB scale, the other colors indicate regions with intermediate charge concentration. As the protonation/deprotonation state causes an unbalance in the total charge of the molecule, it becomes impossible to use a single value scale for the MEP results. For this reason, each molecule has asterisks (*) that indicate the exact numeric scale used for the MEP results.

In general, CAFI indicates interactions involving the frontier orbitals of nucleophilic (f^+) and electrophilic (f^-) species. Such interactions are commonly defined as “soft-soft”

Figure 16 – Structure, Fukui indices, and map of electrostatic potential (MEP) of studied molecules when dissolved in water. The number of asterisks (*) in each molecule is used to indicate the scale of the map of the electrostatic potential, because the protonated/deprotonated states of the molecule are unbalance in the charge.

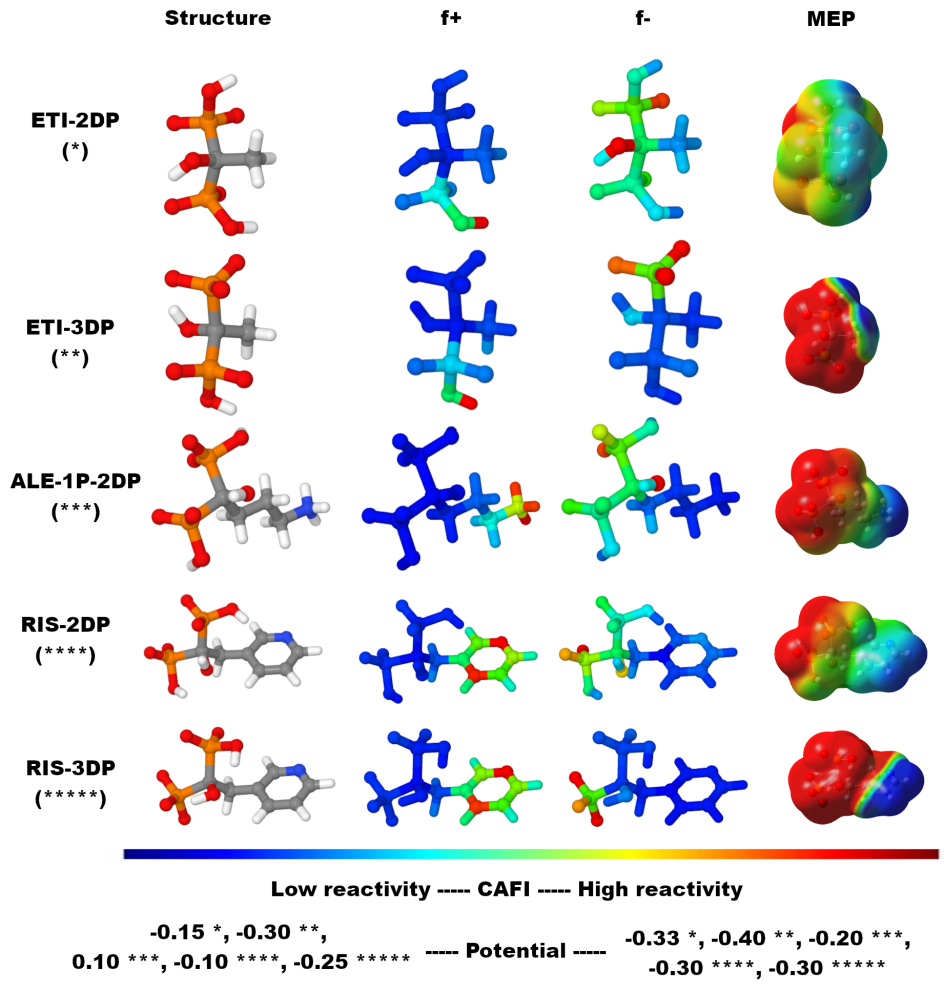

Source: Developed by the author

interactions since they are associated with deformations in the frontier orbitals induced by external species, while MEP shows possible electrostatic interactions, known as “hard-hard” interactions with little deformation of the electronic molecular orbital (MELIN et al., 2004).

In etidronic acid with two deprotonations (ETI-2DP), the -OH of the phosphonic acid group is the region more susceptible to nucleophilic attacks, while the phosphonic acid group and the -OH are the regions more prone to interact with external electrophilic sites. The MEP of etidronate displays regions of elevated negative electrostatic potential around the oxygen atoms of the molecule, while the positive electrostatic potential regions remain around the H atoms.

For the etidronate with three deprotonations (ETI-3DP), the -OH group of the phosphonic acid that did not deprotonate presented a reactive site related to nucleophilic attacks,

which can indicate that the etidronic acid could go through four deprotonations. For electrophilic attacks, the phosphonic acid group that passed through three deprotonations on -OH showed to be the most probable region to interact with electrophilic agents. The MEP displays regions of intense negative electrostatic potential around the deprotonated oxygen atoms of the phosphonate groups, while the regions of positive electrostatic potential remain around the hydrogen atoms that were not deprotonated.

In alendronate with one protonation and two deprotonations (ALE-1P-2DP), the region more prone to interact with external nucleophilic attacks is the -NH_3. For external electrophilic attacks, the reactivity of the molecule concentrates around the phosphonic acid group, mainly in the deprotonated oxygen atom. The MEP displays regions of negative electrostatic potential around the phosphonate groups, while the region of positive electrostatic potential remains in the amine group.

The risedronate with two deprotonations (RIS-2DP) exhibits a region prone to interact with nucleophilic attacks around the pyridine ring, especially for the nitrogen atom. For electrophilic attacks, the more prone regions are the phosphonic acid groups, mainly in the deprotonated oxygen atom. The MEP shows regions of negative electrostatic potential around the phosphonic acid group and regions of positive electrostatic potential around the pyridine ring.

For the risedronate with three deprotonations (RIS-3DP), the reactivity for nucleophilic attacks remains as in risedronate with two deprotonations (RIS-2DP), concentrated in the pyridine ring (mainly in the nitrogen atom and in its position). The regions are inclined to interact with external electrophilic attacks concentrated in the phosphonic acid group with all oxygen atoms deprotonated. The MEP displays regions of negative electrostatic potential around the phosphonic acid groups, while the negative electrostatic potential regions are more present around the pyridine ring.

Such results are consistent with previous experimental published data, this suggests that the chemical characteristic of the nitrogen-containing bisphosphonates (N-BPs) is responsible for its biological effect and binding with hydroxyapatite surfaces (CHEN et al., 2012; PETROVIć et al., 2020; FERNáNDEZ; ORTEGA-CASTRO; FRAU, 2017; RI et al., 2018).

4.2.2 XPS characterization

High-resolution XPS spectra were used after drying to verify the presence of adsorbate groups from bisphosphonate adsorption on titania surfaces in water. Samples immersed in bisphosphonate aqueous solutions with a concentration of 1 mM for 15 minutes and 2 hours were used to confirm the surface modification of the titania substrates in a short time. The XPS findings for the overnight exposure were published elsewhere (BRONZE-UHLE

et al., 2019a). Figure 17 presents the XPS high-resolution C1s, O1s, and N1s spectra for sputtered-deposited titania. The C1s signal exhibited four contributions at 285.0 eV from aliphatic carbon and contributions at higher binding energy, centered at 285.9 eV, 286.6 eV, and 288.8 eV, also from adventitious carbon, in agreement with previous work (DIAS et al., 2020). O1s signal showed two contributions centered at 530.1 eV and 531.3 eV, which are oxidic oxygen from titanium dioxide and organic oxygen/hydroxyl groups, respectively. Finally, N1s spectra presented a single contribution at 400.2 eV, and a minor contribution from organic nitrogen species was also observed on C1s spectra at 285.9 eV (THEILE-RASCHE et al., 2020; LANDOULSI et al., 2008).

Figure 17 – C1s, O1s, and N1s high-resolution spectra for sputtered-deposited titania; C1s high-resolution spectra of etidronic acid (ETI), alendronic acid (ALE), and risedronic acid (RIS) layers adsorbed on titania.

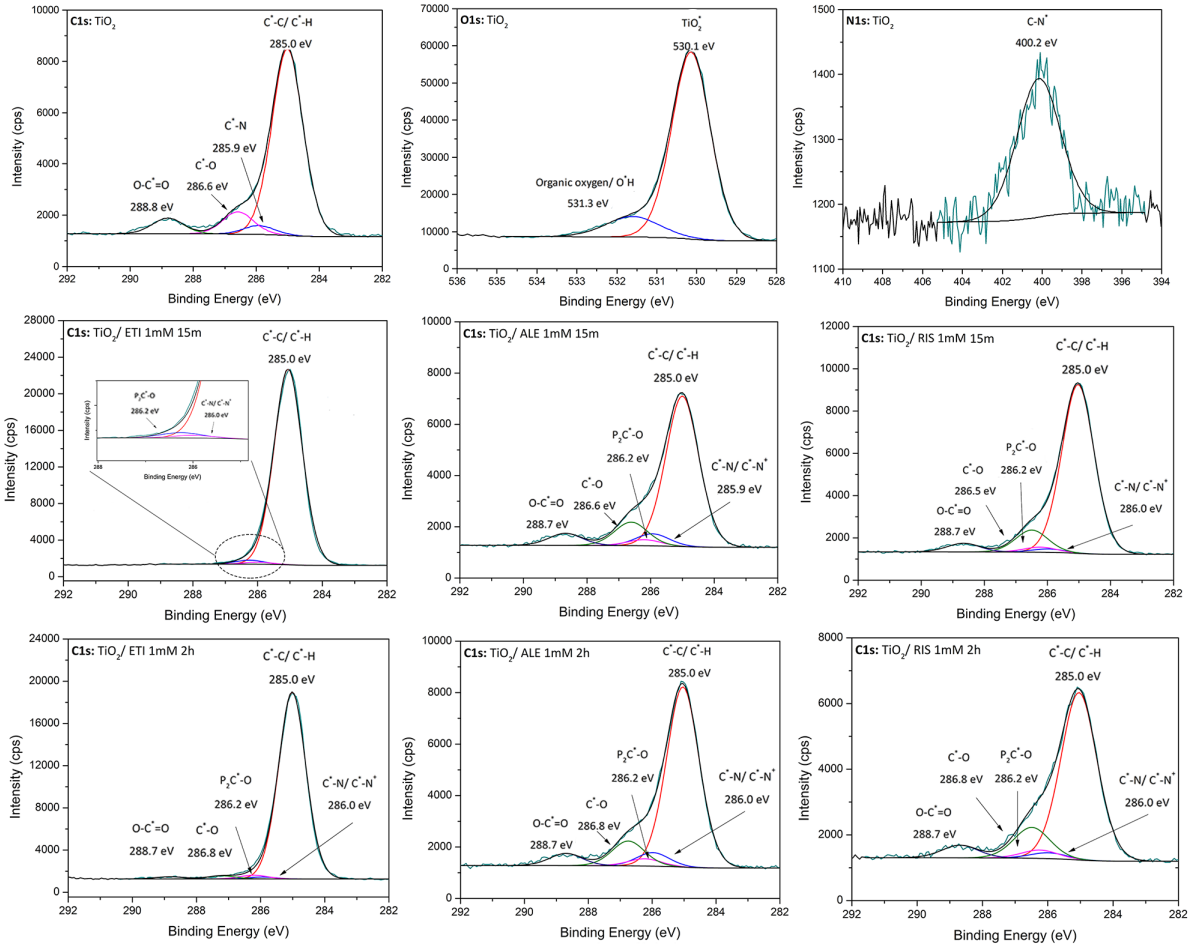

Source: Developed by the author

C1s, O1s, and N1s high-resolution spectra for bisphosphonate species adsorbed on titania are presented in Figures 17 and 18. As bisphosphonic acid molecules have a similar composition due to the common -O_3P-C(OH)R-PO_3- backbone and only differ in the respective substituent R, a difference in the spectra is expected mainly in the C1s and N1s signals. The full widths at half maximum (FWHM) of the peaks obtained from fitting can be

found in the supplementary material. C1s highresolution spectra of TiO_2/BP layers presented the same contributions observed on pristine titania. Centered at 286.2 eV, the contribution related to P_2C*-O moieties is characteristic of bisphosphonic acids as presented in Figure 39 for bulk etidronate (GAO; SHERWOOD, 2013). The decreased area related to carboxyl moieties on the TiO_2/ETI sample compared with the pristine titania surface is related to competitive adsorption, as observed for ODPA monolayers (DIAS et al., 2020). No differences were observed with the increased immersion time, indicating that the surface rapidly reached saturation and that 15 m, 2 h, and 24 h may present similar behavior. Figure 18 presented the O1s and the N1s high-resolution spectra of bisphosphonic acid layers adsorbed on titania after 2 hours of immersion. P2p high-resolution spectra were adjusted using an area ratio of 2:1 between $2p_{3/2}$ and $2p_{1/2}$ contributions due to the spin-orbit coupling, and the plot was omitted. All adsorbed bisphosphonates showed a $P2p_{3/2}$ binding energy of 133.3 ($\pm$ 0.1) eV, this indicates a lack of differential surface charging during the measurements and that calibration based on positioning the C1s signal of hydrocarbonaceous carbon species at 285.0 eV was appropriate (MOULDER, 1993). As the samples were thoroughly rinsed with solvent after functionalization, the detected bisphosphonates were considered adsorbed on titania.

O1 s high-resolution spectra showed three peaks for all titania samples/BP. Contributions were fitted based on the approach previously published for bulk ODPA; as the molecule has a phosphonate group, the presence of P=O, P-O-H, and P-O-Ti groups would be expected for adsorbed bisphosphonates (DIAS et al., 2020; THEILE-RASCHE et al., 2020; ZOULALIAN et al., 2010). Thus, the spectrum was fitted considering a third peak at higher binding energy from P-O*-H contribution, related to free phosphonic acid moieties. The peak around 530.1 eV is related to oxide species from titania substrate (BEAMSON, 1993). The second peak is from organic oxygen, P=O*,and P-O*-Ti species around 531.1 eV and free/not adsorbed P-O*-H species around 532.4 eV (PETROVIć et al., 2020; THEILE-RASCHE et al., 2020; ZOULALIAN et al., 2010).The formation of P-O-Ti may occur through a Ti^+ and PO^- species, consistent with DFT results. BPs can also protonate when exposed to Ti-OH groups, which leads to a condensation reaction, forming P-O-Ti and H_2O.

For the N1s signal, one contribution is expected from the alendronate and risedronate structure from the substituent R_2; however, along with the organic contribution of about 400 eV, the presence of nitrogen N1s peak centered at 401.6 eV was detected and attributed to positively charged nitrogen (BEAMSON, 1993). Nitrogen species about 398 eV were not verified on sputtered deposited titania, as presented in a previous study for rough rutile surfaces (R_a=9.34 $\pm$ 0.2 nm) (BRONZE-UHLE et al., 2019a). The same was true for ammonium. These results reinforce that the surface chemistry of oxide surfaces influences the adsorption of nitrogen-containing bisphosphonates (ZHENG; NEOH; KANG, 2017).

Although these differences compared with other XPS studies in the literature of BPs

Figure 18 – O1s and N1s XPS signals for etidronic acid (ETI), alendronic acid (ALE), and risedronic (RIS) adsorbed on titania.

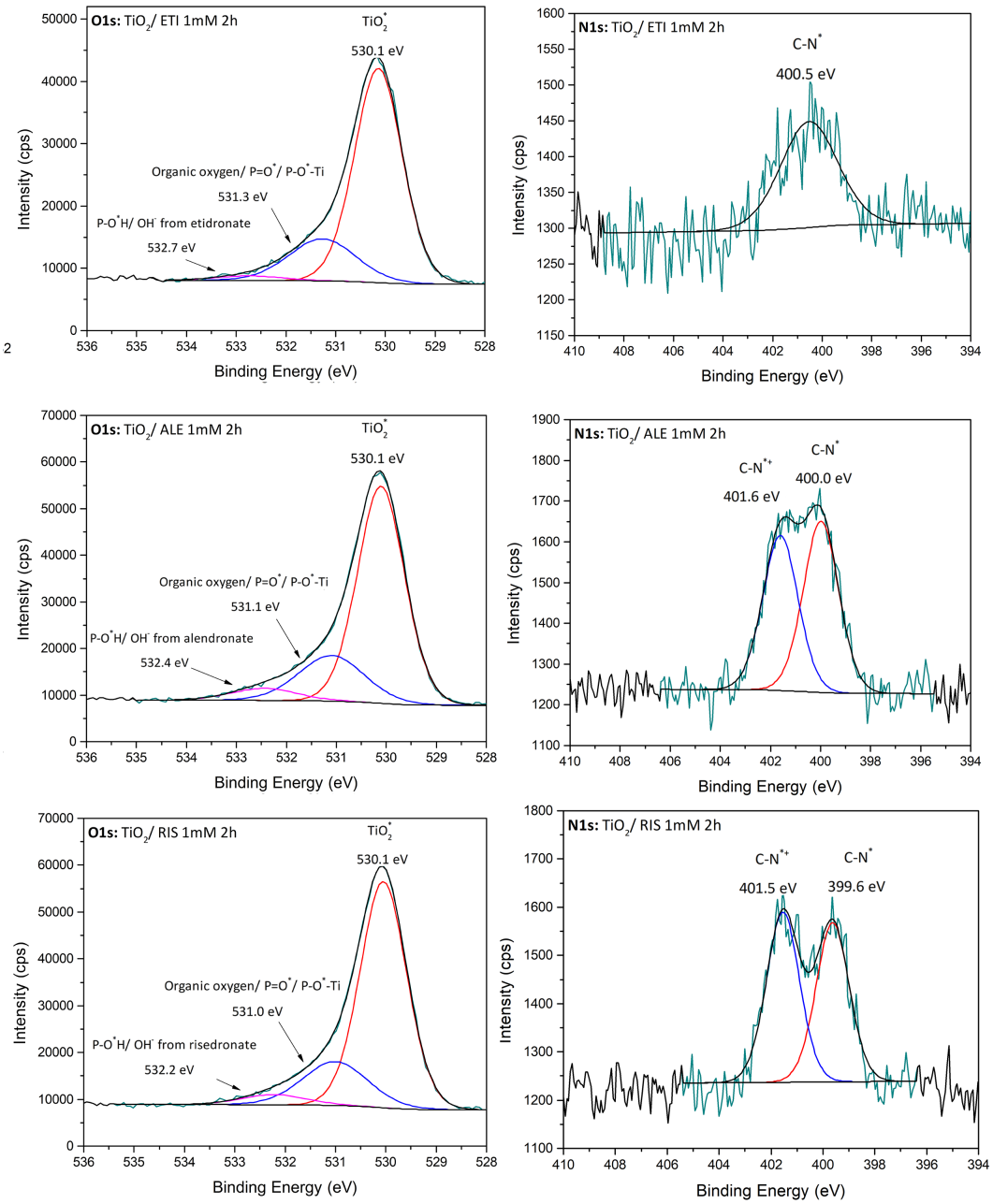

Source: Developed by the author

adsorbed on TiO_2, prior surface hydroxylation modifies the conformation of bisphosphonates (ZHENG; NEOH; KANG, 2017; BRONZE-UHLE et al., 2019a). Consequently, our results may indicate a particularity of amorphous titania and BP adsorption. The composition of titania surfaces influences the point of zero charge (pzc). The pzc values of crystalline and amorphous titania are different on flat surfaces (KOSMULSKI, 2002). Since the adsorption of BPs was done using HPLC quality water (pH 7), the surface had a charge close to zero, allowing the protonation of nitrogen groups during the adsorption (HANAWA, 2011; SRIPRANG; WONGNAWA; SIRICHOTE, 2014). Some N-BPs are protonated at physiologi-

cal pH (FERNáNDEZ; ORTEGA-CASTRO; FRAU, 2018). Further investigations must be performed to elucidate additional details and the influence of titania surface and chemistry on bisphosphonate adsorption.

To obtain details about bisphosphonate layer formation, we followed the procedure introduced by Goncalves *et al.*, the relative [P]/[Ti] concentration ratios normalized for a selfassembled monolayer of octadecylphosphonic acid (ODPA) on sputter-deposited titania were compared (DIAS et al., 2020). Table 12 provides ([P]/[Ti])/([P]/[Ti]$_{ODPASAM}$) values for different BP/titania adsorbates. Since they are smaller than the ones observed for a monophosphonate SAM even though a BP moiety contains two -PO_3- groups instead of one per ODPA species, we inferred that all the titania/BP adsorbates are characterized by a lower area density of adsorption sites than the ODPA SAMs.

Table 12 – Normalized XPS signal intensity ratios for bisphosphonate samples adsorbed on TiO_2, based on an octadecylphosphonic acid monolayer (ODPA SAM) previously published.

Sample name	([P]/[Ti])/([P]/[Ti]$_{ODPASAM}$)
TiO_2/ETI 1mM 15m	1.30
TiO_2/ETI 1mM 2h	0.94
TiO_2/ALE 1mM 15m	0.59
TiO_2/ALE 1mM 2h	0.62
TiO_2/RIS 1mM 15m	0.62
TiO_2/RIS 1mM 2h	0.59
TiO_2/ODPA SAM	1.00

Source: Developed by the author

Based on this table and XPS results, 15 minutes and 2 hours of immersion leads to an exposure of phosphonates moieties, which was also confirmed for overnight exposure (BRONZE-UHLE et al., 2019a). Such exposure influences properties such as water contact angle and zeta potential. Furthermore, a comparison of the normalized [P]/[Ti] ratio shows that the conformation of BPs on the titania surface is not strongly affected by the increase in immersion time. Finally, the ratio of N-BPs and etidronic acid is about 1.5. This was attributed to the fact that etidronic acid can adsorb only through two phosphonates groups. Nitrogen-containing BPs can interact through three different sites, leading to lower values of [P]/[Ti] as the nitrogen groups interact with hydroxyl groups on the titania surface forming N^+ species, as detected by XPS (SPATZ et al., 1997). The interaction of nitrogen groups occupies a site that blocks a bond of another molecule. This idea is summarized in Figure 19.

4.2.3 Contact angle

Water contact angle measurements were performed to verify the modification of the surface wetting behavior due to bisphosphonate adsorption on titania surfaces. A spreading

Figure 19 – Representation of I) etidronic acid, II) alendronic acid, and III) risedronic acid molecules adsorbed on titania surface. Hidrogen atoms are represented in white, carbon in grey, oxygen in red, nitrogen in blue, and phosphorous in yellow.

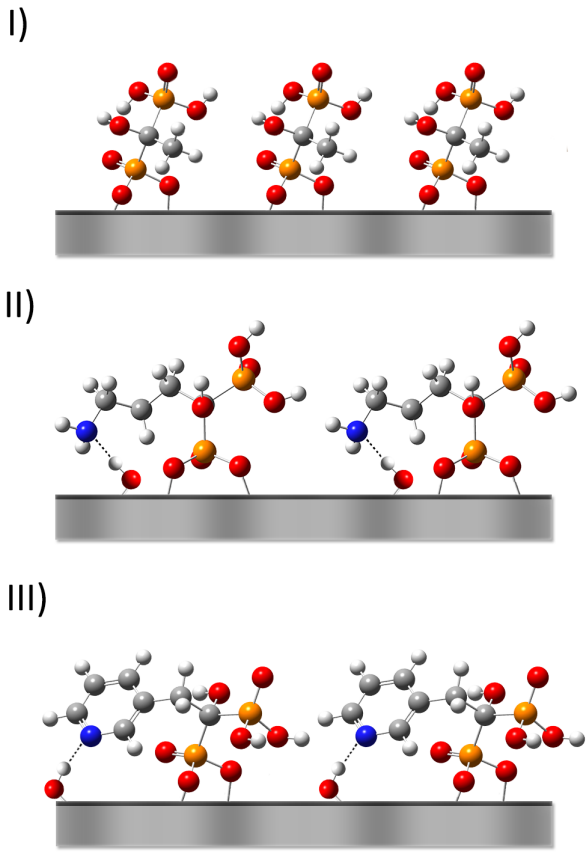

Source: Developed by the author

of water was reported for bisphosphonate layers due to the presence of phosphonates and nitrogen-containing groups (PETROVIć et al., 2020; CICCO et al., 2019; ALMUQRIN et al., 2020). Our findings from water contact angle measurements are in Table 13.

Table 13 – Water contact angle (WCA) for the studied layers.

Sample name	**Water Contact Angle (°)**
TiO_2	11.4 ± 3.5
TiO_2/Alendronate	21.6 ± 2.6
TiO_2/Etidronate	15.1 ± 1.0
TiO_2/Risedronate	22.8 ± 2.0

Source: Developed by the author

The presence of -PO_3H_2 and -NH_2 groups provides a hydrophilic behavior on surfaces (ROJO et al., 2016; ZHENG; NEOH; KANG, 2017; BRONZE-UHLE et al., 2019a; CICCO et al., 2019). Our results indicate that the titania surface is hydrophilic after the immersion in all the bisphosphonate solutions. XPS results show the presence of phosphonate and nitrogen groups on the surface after 15 minutes of thorough rinsing with water, a period that exceeds

the contact time between the water droplet and the titania surface/BP. Thus, although the wetting behavior of the titania/BP surfaces is similar to that of pristine titania, we inferred that the WCA findings relate to BP adsorbate systems. The surface containing risedronate exhibited a slightly higher value, possibly due to the pyridinium ring. This behavior was reported in previous work on rough surfaces (BRONZE-UHLE et al., 2019a).

4.2.4 Zeta potential measurements

Zeta potential measurements of bisphosphonate adsorbates are scarce. Electrokinetic assessments are performed only on hydroxyapatite particles or related particulate materials. Thus, the following results are the first that demonstrate BP/titania zeta potential measurements on a solid surface over a range of pH values. Smooth substrates were used to reduce the influence of roughness, as presented elsewhere (DIAS et al., 2020).

The results from zeta potential measurements are displayed in Figure 6. For pristine titania, the same behavior depicted in a previous work was observed (DIAS et al., 2020). The bisphosphonates exhibited increased zeta potential values compared to pristine titania with a decreased pH. In neutral pH, the phosphonate groups exist mainly as deprotonated groups (C-PO_3^{2-}) rather than CPO_3H_2, leading to negative values for zeta potential at pH values around 6.7 (BEDOYA et al., 2017). This is consistent with the findings from MEP simulations, indicating that deprotonated phosphonic acid is predominant.

Although etidronate has the simplest structure of the investigated bisphosphonic acids, TiO_2/ETI curve is very similar to ODPA on titania, where the surface has more negative charge values than pristine titania, this indicates the presence of the adsorbates on the surface. Such values are attributed to unbonded P-OH, corroborated by XPS results (DIAS et al., 2020). This is also confirmed by the MEP findings, as the etidronic acid molecule becomes more suitable for nucleophilic attacks after two deprotonations than in a neutral state.

As reported, the zeta potential of alendronate adsorbates has positive values for zeta potential on hydroxyapatite crystals at physiological pH, while the opposite occurs for risedronate (NANCOLLAS et al., 2006). Despite this contrast, both presented similar biological efficacy at the same concentration. The surface containing alendronate has a curve similar to pristine titania; a similar behavior was reported for alendronate on the titania surface at pH 7.4 (ZHENG; NEOH; KANG, 2017).The presence of protonated amine plays an important role in balancing the deprotonated phosphonate. MEP validated such behavior. Moreover, different studies found that free alendronate has a charge equal to zero in acidic conditions due to the protonated amine and one deprotonated phosphonate. However,with the increase of the pH at physiological value, additional hydrogens leave the phosphonate leading to a negative liquid charge (FERNáNDEZ; ORTEGA-CASTRO; FRAU, 2017; KE et al., 2016). As presented by XPS, approximately half of the amine groups are protonated.

Figure 20 – Zeta potential measurements of bisphosphonates adsorbed on TiO_2.

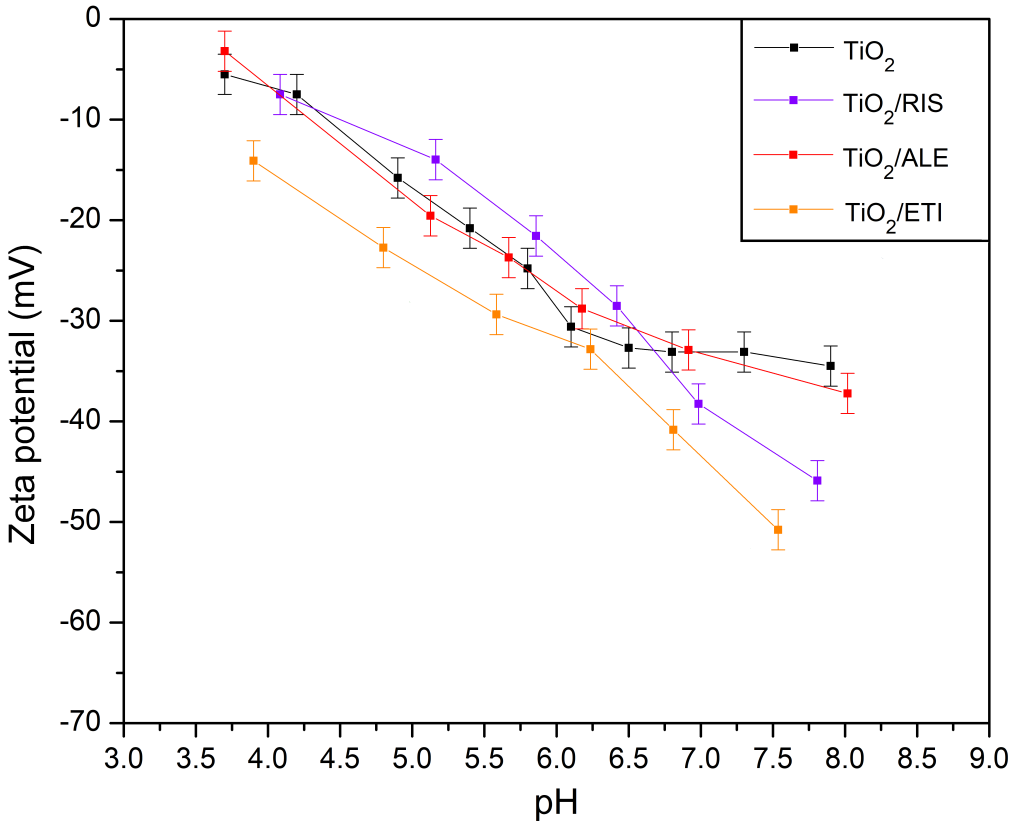

Source: Developed by the author

Consequently, the small decrease of the zeta potential compared with the pristine titania may occur due to the limited number of deprotonated phosphonates.

For risedronate, the presence of nitrogen influences the zeta potential only when pH is lower than 3. Deprotonation of phosphonates starts at pH 5 and reaches the maximum effect at pH greater than 10 (BEDOYA et al., 2017). Hence, the TiO_2/RIS curve becomes more negative after pH 6, near to etidronate. This is reinforced by the presence of P-OH moieties observed through XPS and the change of electrostatic potential from theoretical modeling.

4.2.5 Atomic force microscopy

Figure 21 contains topography images and the RMS of roughness. Peak heights can vary according to the adsorbate on the surface based on the scale bar. Samples showed a similar roughness value as the pristine substrate after adsorption of bisphosphonates, except for alendronic acid, which presented a slightly lower value. Due to the low roughness of substrate surface and the lack of data from bisphosphonates in the literature, the results are difficult to compare with other studies.Nonetheless, few studies present the change of roughness caused by bisphosphonic acid adsorption.

Figure 21 – AFM images of bisphosphonates adsorbed on smooth titania.

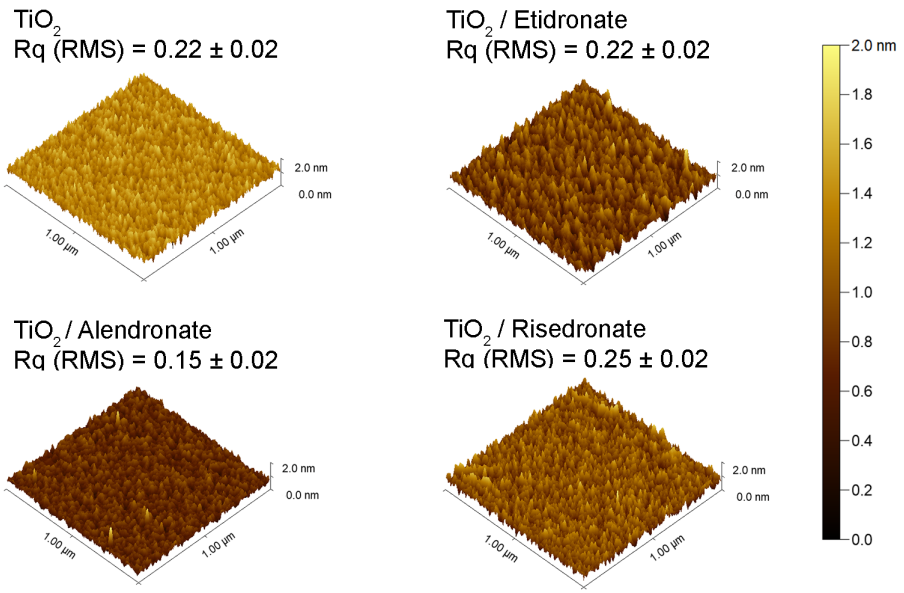

Source: Developed by the author

On hydroxyapatite (HA) surfaces, values can vary from 28.9 to 50.1 nm for pristine HA and etidronic acid adsorbed on HA, respectively (OTHMANI et al., 2013). Smooth titania exhibited no significant change in surface roughness after adsorption of alendronic acid using different strategies. The reported values vary between 187 and 175 nm for pristine and functionalized substrates, respectively (ZHENG; NEOH; KANG, 2017).

As mentioned in the discussion of the XPS results, surface chemistry plays an important role in bisphosphonic acid adsorption. Thus, the surface topography may also affect the adsorption process. A smooth surface might favor an arrangement where the molecules follow the titania topography, as observed in octadecylphosphonic acid (DIAS et al., 2020). A rough surface, especially hydroxyapatite, may approximate the molecules increasing the adsorption caused by the charge of bisphosphonic acids, thus leading to higher roughness values (NANCOLLAS et al., 2006).

4.3 Conclusion

This work presents insights about changes in physicochemical aspects of bisphosphonate layers on titanium dioxide. The results help broaden the comprehension of BPs on titania surfaces through theoretical modeling and extensive surface characterization. The study demonstrated that pH and adsorption medium must be considered when dealing with these molecules. In the case of an aqueous medium, oxygen increases the chance of nucleophilic interactions, while nitrogen is more suitable for electrophilic attacks. The DFT results were corroborated by the XPS investigation, in which highresolution N1s show

protonated species on alendronate and risedronate. Besides this, it was demonstrated the formation of Ti-O-P bonds, consistent with the MEP results. XPS investigation demonstrated that exposed phosphonate moieties influence water contact angle and zeta potential; furthermore, the presence of additional groups leads to less dense layers of nitrogen-containing BPs compared with etidronic acid. Water contact angle measurements confirmed that these groups lead to more hydrophilic surfaces, indicating that all functionalized samples remained with a low WCA. For zeta potential measurements, the particularity of each structure was discussed on a solid surface, considering a pH range for the first time. For etidronate, the prevalence of negative charges of unbounded P-OH leads to more negative values of zeta potential. Despite exhibiting free phosphonates, alendronate has a protonated amine which partially balances the charge leading to values close to pristine TiO_2. On the other hand, the influence of the nitrogen group is reduced on risedronate, because protonation occurs only at a pH lower than 3. Thus, at pH higher than 6, zeta potential indicates negative values, forced by free P-OH groups, which start the protonation close to pH 5. After adsorption of bisphosphonates, the titania surface remains smooth, suggesting that the molecules may be affected by substrate roughness and surface chemistry. As complementary works, we recommend quantitative measurements of the adsorbed amount of BP and also the stability of BP layers, and the determination of adsorptions curves of bisphosphonic acids with deeper computational modeling (such as adsorption energy calculations of the BP's + substrate system). The use of bioactive molecules adsorbed on smooth surfaces was revealed as a suitable strategy to provide a deeper understanding of the physicochemical aspects of these molecules, particularly when allied with modeling. Once the surface is well characterized, the next step is to understand how surface properties influence biological performance.

4.4 Supporting Information Summary

The supporting information comprises details of sample preparation and experimental details for data acquisition. Bisphosphonates modeling in a vacuum is also presented, as well XPS measurements of bulk etidronate, and FWHM of XPS analysis.

4.5 Acknowledgments

The authors are grateful to the São Paulo Research Foundation (FAPESP) for the financial support through the grants 2019/13100-0, 2018/07520-3, and 2019/09431-0. Marina Honorato Cardoso for critical reading. Dirk Salz assisted with sputtering deposition, and Thorben Brenner supported zeta potential measurements. Open Access funding enabled and organized by Projekt DEAL.

5 Adsorption and X-ray photoelectron spectroscopy investigation of bisphosphonates on titania and hydroxyapatite surfaces

This chapter is currently under review on *Surfaces and Interfaces*.

5.1 Introduction

For biomedical implants, mechanical properties and surface characteristics must be considered (RATNER; CASTNER, 2020). Thus, different studies have explored thin film production and organic molecule adsorption to modulate surface properties such as wettability, biocompatibility, and antibacterial activity (BRONZE-UHLE et al., 2019a; BRONZE-UHLE et al., 2019b; TRINO et al., 2018b; DIAS et al., 2022).

Because it adheres well to metallic substrates and its surface can be modified so that hydroxyl groups are present, titanium dioxide (TiO_2) has been extensively studied for application to surface modifications and implant coatings (HANAWA, 2019). However, TiO_2 is less biocompatible than hydroxyapatite (HA), which plays a crucial role in biocompatible surfaces and is one of the main components of human bone. In contrast to TiO_2, HA poorly adheres to metallic substrates (HAN; YU; ZHOU, 2008; HARUN et al., 2018). Thus, TiO_2+HA composite films are suitable for overcoming poor adhesion and increasing surface biocompatibility (WANG et al., 2018; HE et al., 2008). Furthermore, to increase biological performance, these surfaces can be functionalized with different compounds ranging from amphiphilic molecules to proteins (BRONZE-UHLE et al., 2019b; DIAS et al., 2020; ALBANO et al., 2020).

Bisphosphonates (BPs), an organic pyrophosphate analog, are a class of organic molecules employed for treating osseous diseases, and their linear structures are presented in Figure 22 (MENEZES et al., 2005; ROGERS; MöNKKöNEN; MUNOZ, 2020). Most studies have focused not on adsorption but on biological performance, BPs may both increase osteoblast metabolic activity while killing osteoclasts, thus increasing new bone formation (MENEZES et al., 2005; RUSSELL; CROUCHER; ROGERS, 1999; CUI et al., 2019).

Because of their ability to coordinate with calcium ions, BPs have a strong affinity for HA (MENEZES et al., 2005; CHEN et al., 2020). Thus, different studies, from theoretical calculations to measured adsorptions, have been conducted on the interaction of BPs with

Figure 22 – Linear structures of BPs, etidronate, alendronate, and risedronate.

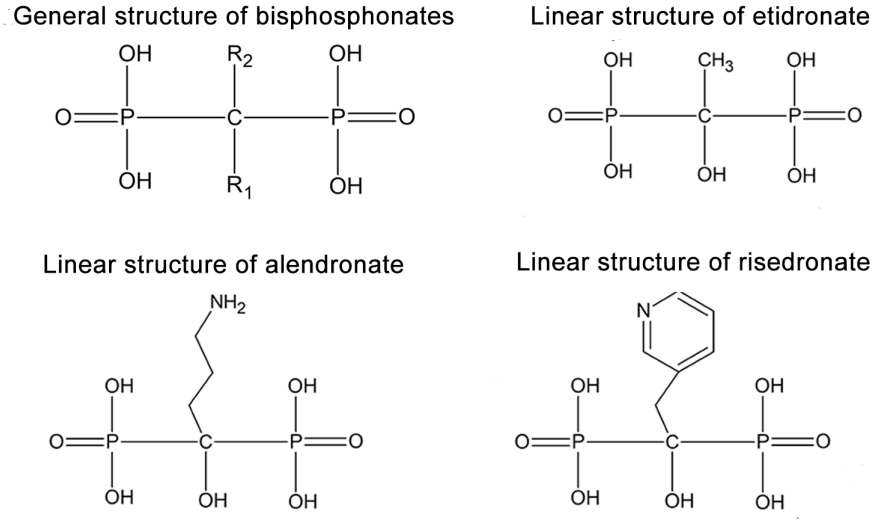

Source: Developed by the author

HA (FORTE et al., 2017; FORTE et al., 2019; CHEN et al., 2012; AGHABOZORG et al., 2012). However, few studies have focused on the TiO_2/BP system (BRONZE-UHLE et al., 2019a; DIAS et al., 2022; PETROVIć et al., 2020). When BPs interact with HA, HA phosphate groups may be substituted for BP phosphonate groups, and/or calcium ions may coordinate with BP anions (PALAZZO et al., 2007). BPs can adsorb on TiO_2 through phosphonate groups, forming mono- or bidentate Ti–O–P bonds (BRONZE-UHLE et al., 2019a; DIAS et al., 2022; PETROVIć et al., 2020).

Therefore, we measured etidronate and alendronate BP adsorption on anatase and rutile TiO_2 to determine the influence of hydroxylation on adsorption and explore the effects of etidronate, alendronate, and risedronate on TiO_2, HA, and composite films. To the best of our knowledge, this is the first study to report a TiO_2+HA/BP system and generate adsorption curves for BPs on oxidized surfaces. The samples were investigated by X-ray diffraction (XRD), confocal microscopy, scanning electron microscopy (SEM), measuring water contact angles, X-ray photoelectron spectroscopy (XPS), and atomic force microscopy (AFM). The study findings could accelerate the development of biomedical implants exhibiting superior biocompatibility, wettability, and antibacterial activity. Besides, helps to elucidate the understanding of the properties of surfaces-containing bisphosphonates.

5.2 Materials and methods

5.2.1 Materials

For sol–gel synthesis, titanium (IV) isopropoxide (Sigma–Aldrich®/CAS 546-68-9) and nitric acid (65% Synth®/CAS 7697-37-2) were employed as precursors. The adsorptions of disodium etidronate hydrate (TCI® German/CAS 7414-83-7), sodium alendronate

trihydrate (TCI® German/CAS 121268-17-5), and sodium risedronate (Sigma–Aldrich®/ CAS 115436-72-1) were investigated. Hereinafter, etidronate, alendronate, and risedronate are referred to as “ETI,” “ALE,” and “RIS,” respectively. KCl (NEON/CAS 7447-40-7) was employed to prepare the adsorption medium. H_2SO_4 (98% Meta química/CAS 7664-93-9) and H_2O_2 (35% Dinâmica/CAS 7722-84-1) were used to prepare the piranha solution. Cerium sulfate IV tetrahydrate (CAS 10294-42-5) was purchased from NEON® and was used as an oxidizing agent for quantifying BP absorption.

5.2.2 Synthesis of TiO_2 solution, HA, and TiO_2 particles

Titanium dioxide solution was synthesized as described by Trino et al. (TRINO et al., 2018a). For synthesizing HA particles, we employed the procedure described by Ben-Arfa et al. (BEN-ARFA et al., 2017). TiO_2 nanoparticles were synthesized using the same procedure as that for preparing the TiO_2 solution, except the solution was left to dry completely instead of evaporating to 50 mL. The remaining powder was manually macerated using a pestle and a mortar. Anatase and rutile titania nanoparticles were formed by heating the powder at 1 ℃.min^{-1} to 450 ℃ and 850 ℃, respectively, where the samples were held for 2 h and subsequently cooled 1 ℃.min^{-1}.

5.2.3 Preparation of Ti substrates and film deposition

Cp IV was used as the film deposition substrate. First, the substrates were laser-treated, as described by Borcherding et al. (BORCHERDING et al., 2019). The surface was then cleaned using piranha solution (H_2SO_4:H_2O_2, 7:3 v/v) for 2 h. Finally, the substrates were ultrasonically cleaned with water and acetone for 10 min each and then dried at 60 ℃ prior to deposition.

Four dispersions were prepared for film deposition. To prepare the titania films, the pristine TiO_2 solution was diluted in isopropanol (1:3 v/v). The hydroxyapatite dispersion was prepared by mixing 300 mg of HA powder with 6 mL of ethylene glycol. The mixture was then stirred for 15 min at 60 ℃. Then, 106 L of Triton-X and 1 mL of isopropanol were added, and the product was stirred for 15 min. Finally, the dispersion was ultrasonicated for 10 min. The final dispersions comprised mixtures of 1:1 and 1:2 v/v TiO_2 and HA (i.e., TiO_2:HA 1:1 and TiO_2:HA 1:2, respectively). Finally, isopropanol was added at a ratio of 3:1 v/v TiO_2.

The films were deposited by spin-coating at 2000 rpm for 60 s. Before spinning, three drops of the desired dispersion were placed on the substrate. After 60 s, the films were dried at 60 ℃ for 5 min. This procedure was repeated three times. The spin-coated films were heated at 1 ℃.min^{-1} to 850 ℃ where they were held for 2 h and then cooled at 1 ℃.min^{-1}.

5.2.4 BP adsorption

We determined calibration curves for ETI and ALE. The linearity regime was between 0 and 2 mM, representing the adsorption curve values for which the equilibrium concentration (Ceq) was < 2 mM. In each experiment, different ETI and ALE solution concentrations were prepared, usually 0.2 to 4 mM. For the adsorption test, 5 mg of titanium dioxide was left undisturbed to react with 1000 μL of the BP solution, and all experiments were performed in triplicate. First, the saturation time was determined, and the system was left undisturbed without stirring for 1, 2, or 3 h. The optimum adsorption time was 2 h.

For measuring BP adsorption on the films, we employed ETI, ALE, RIS, and 1 mM aqueous KCl (pH 7). BP solutions (0.2 and 4 mM) were prepared. Prior to functionalization, the films were irradiated with ultraviolet (UV)-C (254 nm; 8 W) light for 45 min to increase the number of OH groups on and clean the surface (BRONZE-UHLE et al., 2019a). For functionalization, 3 mL of the BP solution was left to react with each disk for 2 h, and the disk was then washed twice with distilled water to remove any residual BP solution.

5.2.5 Characterizations

The crystallinity of the prepared materials was evaluated using XRD (D/MAX-2100/PC, Rigaku) equipped with a CuKα radiation source (λ = 1.54056 Å) coupled to a nickel filter to eliminate CuKβ radiation. The samples were scanned from 10 to 100° in regular steps of 0.02° min^{-1} and at 2° min^{-1} and 40 kV/20 mA. Diffractograms of TiO_2 particles are available in Figure 42.

The UV absorbance was quantified using a Shimadzu UV-1800 spectrophotometer. A 0.5 M aqueous H_2SO_4 solution was used for preparing a 0.1% w/v cerium sulfate solution, following reported by Taha et al. (TAHA; YOUSSEF, 2003). The prepared cerium solution was stored in an amber-colored flask. Cerium sulfate exhibits a characteristic signal at 320 nm, and BP oxidation weakens the signal. The presented values are the absorbance modulus. The BP absorption was measured by placing 250 μL of the BP solution in a 15-mL tube and adding 2000 μL of cerium solution. The mixture was left to react without stirring for 1 h, and 6000 μL of 0.5 M H_2SO_4 was then added. The absorbance was measured by placing 1000 μL of the final product in a cuvette. The same procedure was adopted using a blank for generating a calibration curve by replacing the BP solution with a 1 mM KCl solution. BPs were adsorbed on the titania by adding 5 mg of nanoparticles to 1000 μL of the BP solution. After the established time, the microtubes were centrifuged for 10 min at 10000 rpm. An aliquot (250 μL) was removed using the same procedure. Although the same nanoparticle mass was used as a blank, the BP volume was replaced with an equal volume of 1 mM KCl. We employed CAVS software (freely available at http://www.prppg.ufpr.br/site/posalim/pb/aplicativos/) for model fitting.

The specific surface area was determined using a Micromeritics ASAP-2020. Nitrogen adsorption/desorption isotherms were measured at 77 K, and the surface area was calculated using the Brunauer–Emmett–Teller (BET) method. Prior to the measurements, the samples were degassed at 70℃ for 24 h.

To capture microroughness and 3D images, a confocal microscope (Leica DCM3D) equipped with a 10× lens was used. Root-mean-square (RMS) surface roughnesses were measured for three points in each sample.

SEM images were obtained using a Zeiss LS15 microscope operating at an acceleration voltage of 15 kV. The chemical composition was verified using energy-dispersive X-ray spectroscopy (EDS) for at least two distinct points on each sample.

Water contact angles were measured under ambient conditions using a goniometer (Ramé-Hart 100–00, Succasunna, NJ) and the sessile drop technique. A drop (5 μL) was automatically released over the film. For each sample, two drops were placed in different regions. For each drop, ten water contact angles were calculated using image processing, and the mean angle and standard deviation were calculated.

The chemical compositions of the material surfaces were determined using XPS (Scienta Omicron ESCA) equipped with an EA125 Xm1000 monochromator and an Al Kα (1486.7 eV) X-ray source. The survey spectra were collected using a pass energy of 50 eV and an energy step of 0.500 eV. High-resolution spectra were obtained using a pass energy of 30 eV and an energy step of 0.050 eV. A charge neutralizer (CN10) was used to exclude the surface charging effects. The spectra were fitted using CasaXPS software, and the signal was corrected using the aliphatic hydrocarbon C 1s reference signal at 285.0 eV. The atomic surface concentration was evaluated based on Scofield's relative sensitivity factor (RSF).

The surface nanotopography and nanoroughness of the prepared samples were analyzed using AFM (Park XE7; Park Systems, Santa Clara, CA, USA) operating in the noncontact mode. A silicon cantilever (PPP-NCHR; Park Systems, Inc.) was employed at a constant force of 42.0 N.m^{-1} and a frequency of 330 kHz. Measurements were performed in air at 20ºC. Images (1 × 1 μm^2) were scanned at 0.7 Hz.

5.3 Results and discussion

When applied as a surface modifier, BPs can increase cell growth. Thus, studying their adsorption on TiO_2, usually, the composition of the outermost bioimplant layer, may help to develop more-biocompatible surfaces. We investigated the adsorption of BPs on different surfaces. On particles, we employed ETI and ALE on anatase and rutile surfaces, in addition, we evaluated the effect of hydroxylation on BP adsorption. Our results indicated that hydroxylation is an effective method for increasing BP adsorption. We extensively

characterized TiO_2 and HA film surfaces and found that BPs adsorbed on the surface were exposed to P–OH groups, leading to a water contact angle of 0º.

5.3.1 Effects of BP adsorption on TiO_2 particles

The BET measurements are presented in Table 14. From these results, although anatase titania has a higher surface area than rutile titania, the latter has larger pores, which can influence the adsorption capacity. The anatase and rutile titania comprised nanoparticles and microparticles, respectively, which was expected because we did not control the rutile particle growth.

Table 14 – BET measurements of prepared samples.

	Anatase	Rutile
BET surface area ($m^2.g^{-1}$)	92.6	2.4
Pore width (Å)	60.1	534.5
Nanoparticle size (nm)	64.8	2521.6

Source: Developed by the author

From the experimental data, we obtained parameters for the Freundlich adsorption model, as listed in Table 15. The results showed that hydroxylation increased the affinity of BPs for titania surfaces, which was verified by the increased affinity constant (K). ETI and ALE had higher affinities for anatase and rutile titania, respectively.

Table 15 – Freundlich adsorption parameters obtained from experimental data.

Sample	**N**	***K*** **($(mg.g^{-1})(L.mg^{-1})$)**	**R^2**
ETI on anatase	1.0 ± 0.1	0.2 ± 0.1	0.995
UV + ETI on anatase	2.6 ± 0.2	13.1 ± 1.7	0.988
ETI on rutile	0.6 ± 0.1	0.1 ± 0.1	0.937
UV + ETI on rutile	1.8 ± 0.2	4.5 ± 1.9	0.928
ALE on anatase	5.2 ± 1.1	18.0 ± 4.5	0.873
UV + ALE on anatase	2.3 ± 0.6	4.6 ± 2.9	0.908
ALE on rutile	2.0 ± 0.7	4.9 ± 2.0	0.937
UV + ALE on rutile	5.0 ± 1.1	40.3 ± 10.1	0.927

Source: Developed by the author

The adsorption curves are presented in Figure 23. All the curves show that the surface adsorption increased, which is attributed to hydroxylation. The effect of hydroxylation on adsorption was previously described by our group (BRONZE-UHLE et al., 2019a), and the influence of OH phosphonic acid on adsorption was investigated in another study (LUSCHTINETZ et al., 2010). In our previous study, we observed that hydroxylation predominantly affected adsorption through phosphate groups. In this study, we complement this result by determining that UV exposure increases adsorption on the titania surface.

Phosphonate adsorbs on TiO_2 through deprotonation of H_2PO_3 groups. Deprotonation increases BP reactivity, and HPO^{3-} or PO_3^{2-} reacts with Ti–O on the surface, forming

Figure 23 – Adsorption curves of BP adsorbed on titania particles. Dotted lines represent theoretical curves.

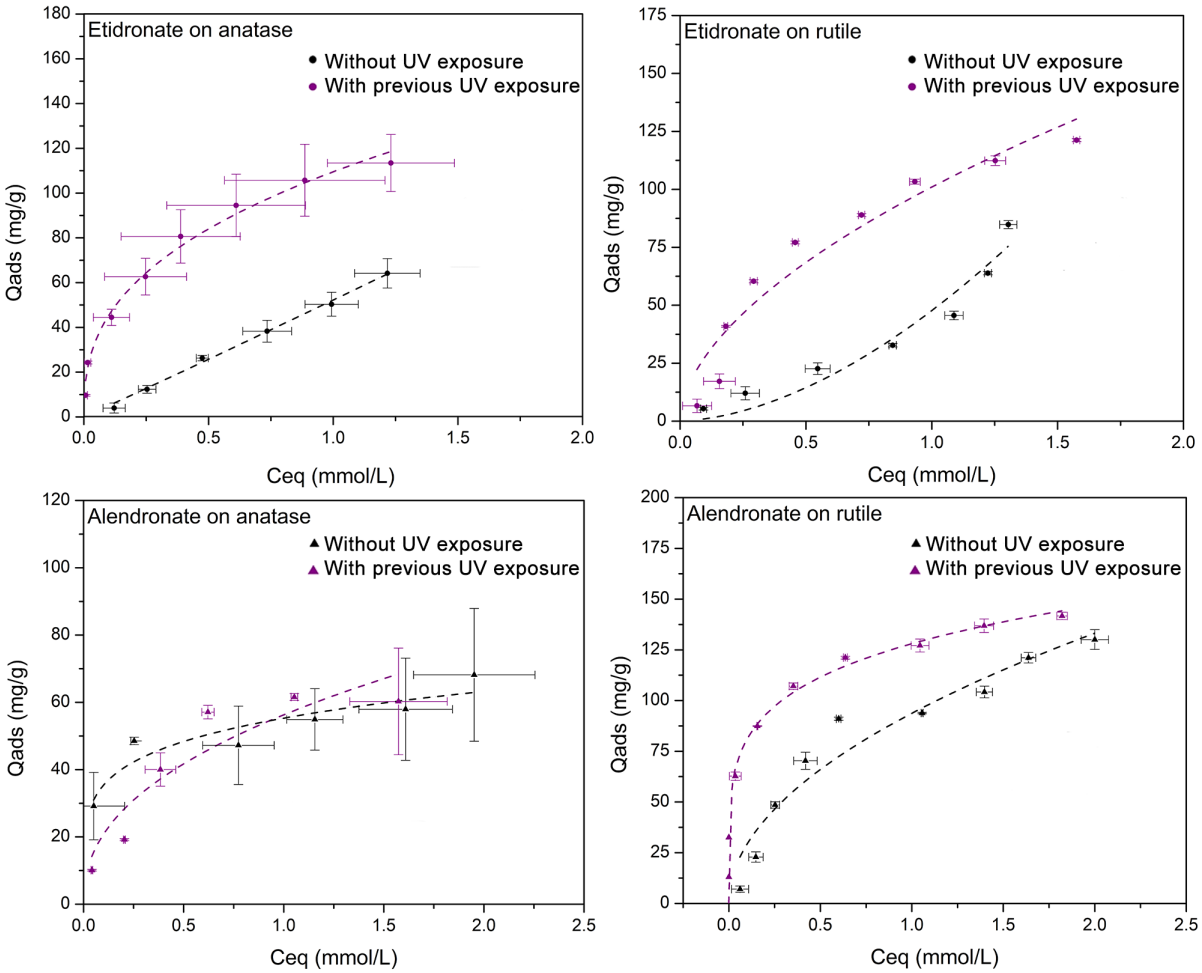

Source: Developed by the author

Ti–O–P bonds (DIAS et al., 2022). BPs are mostly attached through bidentate bonds, exposing the additional phosphate and other groups of the molecule (LUSCHTINETZ et al., 2010), which suggests that hydroxylation increases the BP deprotonation as BPs approach the surface. Thus, the surface OH rapidly recombined with H^+ from the H_2PO_3 groups, forming Ti–O–P bonds. This would also explain the predominant adsorption on Ti surfaces, which decreases the Ti^{3+} content owing to the generation of Ti–OH groups, which favors H_2PO_3 condensation.

5.3.2 Structures and morphologies of prepared films

For the structural analyses, we dried the deposition solutions following the heating procedure described in Section 5.2 The results are shown in Figure 24. The spectrum for titanium dioxide presented rutile characteristic peaks (PDF No. 2-494), which also verified HA formation (PDF No. 3-747). The spectra for the composite materials exhibited rutile, HA, and anatase (PDF No. 21-1272) characteristic peaks. With increasing HA content, the HA

peak intensified.

Figure 24 – XRD patterns of dried dispersions.

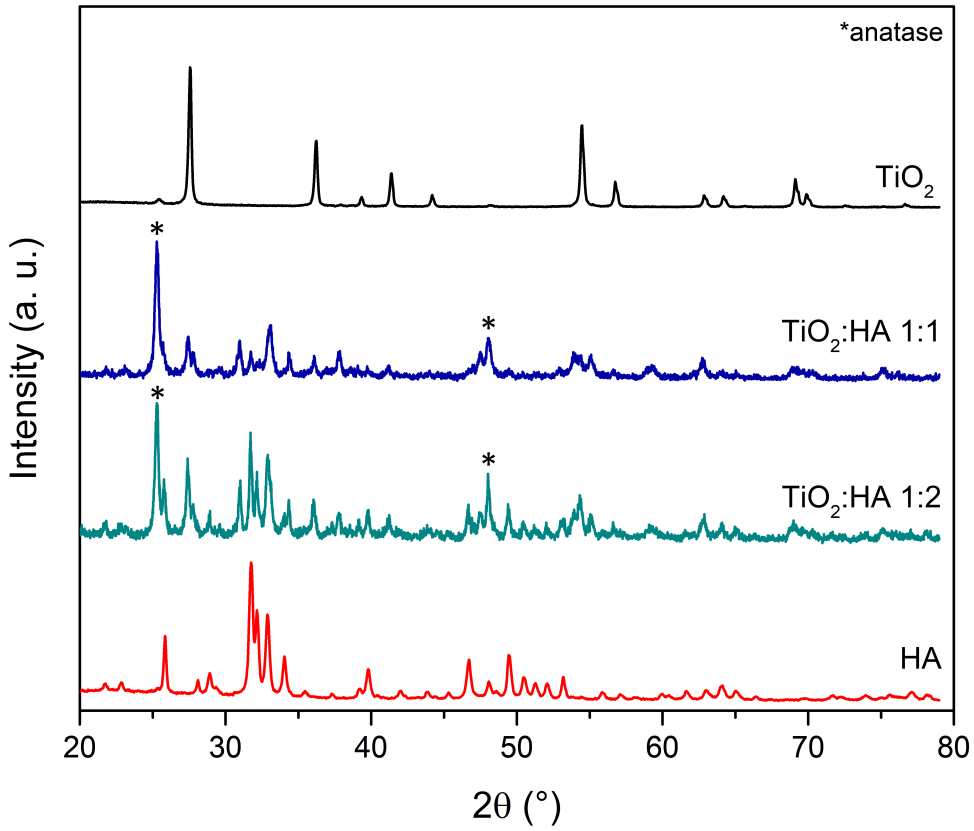

Source: Developed by the author

Table 16 lists the mean surface roughness of the prepared samples. The film deposition decreased the surface roughness by approximately 35% and the HA film exhibited the lowest surface roughness. The standard deviation also reduced, indicating that the film deposition increased the surface homogeneity. Several studies have attempted to determine the relationship between the (nano/micro) surface roughness and cellular activity (MAZóN et al., 2015; RAFIEE; NAFFAKH-MOOSAVY; TAMJID, 2020; ZAREIDOOST et al., 2012). However, no consensus has been reached for the optimum surface roughness. These results were in the same range as those previously reported for good cellular responses (MAZóN et al., 2015; RAFIEE; NAFFAKH-MOOSAVY; TAMJID, 2020). The corresponding confocal images are shown in Figure 42.

SEM was employed to investigate the surface morphology, and the SEM images of the prepared films are presented in Figure 25. At low magnifications, the TiO_2 surface appears smooth compared with the other surfaces. Cracks are common on HA-containing surfaces (MILELLA et al., 2001) and are attributed to mechanical constraints during heating. Only the TiO_2:HA 1:1 film exhibited cracks. The titania and HA surfaces comprised small cubes and rod-like particles, respectively, the composite film surfaces exhibited both particles.

The EDS measurements are listed in Table 17, and the corresponding elemental

Table 16 – Mean surface roughness of prepared samples.

Sample	Mean Surface Roughness (μm)
Ti	41.7 ± 1.6
TiO_2	37.7 ± 0.4
TiO_2:HA 1:1	28.9 ± 0.7
TiO_2:HA 1:2	35.4 ± 0.7
HA	27.8 ± 0.5

Source: Developed by the author

Figure 25 – SEM images of prepared samples.

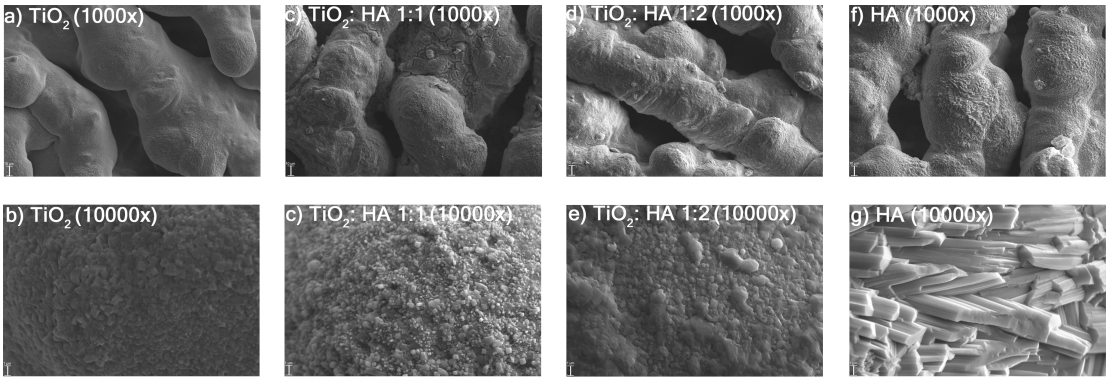

Source: Developed by the author

composition maps are shown in Figures 44-47. The samples contain the expected elements. Calcium and phosphorus were homogeneously distributed on the surface, except for the HA sample, where it was possible to observe regions with higher concentrations. HA and TiO_2:HA 1:1 had Ca/P ratios close to 1.67. TiO_2:HA 1:2 presented a low value of phosphorous compared with the other samples, and once the HA came from the same dispersion of the TiO_2:HA 1:1 sample, this difference was not expected.

Table 17 – Elements in atomic% measured by EDS.

Sample	Elements (at%)			
	Ti	O	Ca	P
TiO_2	28.2 ± 1.9	71.7 ± 1.9	-	-
TiO_2:HA 1:1	28.3 ± 0.4	65.1 ± 0.1	3.7 ± 1.2	2.0 ± 0.1
TiO_2:HA 1:2	26.8 ± 0.7	66.8 ± 2.9	4.1 ± 1.8	1.3 ± 0.7
HA	2.5 ± 0.2	62.2 ± 2.6	16.0 ± 2.0	9.0 ± 0.4

Source: Developed by the author

5.3.3 Effects of BPs adsorption on TiO_2, HA, and TiO_2+HA films

Surface hydrophilicity was evaluated by varying the concentration of BPs. For this, we measured samples functionalized with 0.2 mM and 4 mM solutions. The results demonstrated that small concentrations had the same effect on hydrophilicity at a concentration of 4 mM. Table 18 presents only the results for the 4 mM samples; further results are presented in

Table 21. Once the 0.2 mM and 4 mM samples showed similar results, we focused our investigation on the 4 mM samples.

The results obtained for TiO_2 differed from those obtained for smooth TiO_2 (DIAS et al., 2022). The water contact angle did not show any decrease after BP adsorption (1 mM). This indicates a synergetic effect between the roughness and BP layers. This behavior suggests that our samples follow Wenzel's model: once the substrate has a water contact angle lower than 90º, an increase in roughness leads to an increase in hydrophilicity (QUéRé, 2008; WANG et al., 2020). The pure HA film presented a lower water contact angle than that in the published results (ELIAZ et al., 2009; CHEN et al., 2007). After the adsorption of BP, the water drops completely spread on the surface. The addition of HA to TiO_2 appears to be beneficial, especially for the TiO_2:HA 1:1 sample, which completely spread the drop, even in the absence of BPs.

Table 18 – Water contact angle (WCA) for pristine and samples prepared with 4 mM BP solutions.

Samples	**WCA (°)**
TiO_2	49.7 $\pm$ 8.2
TiO_2/ETI	0*
TiO_2/ALE	0*
TiO_2/RIS	0*
TiO_2:HA 1:1	0*
TiO_2:HA 1:1/ETI	0*
TiO_2:HA 1:1/ALE	0*
TiO_2:HA 1:1/RIS	0*
TiO_2:HA 1:2	34.7 $\pm$ 1.9
TiO_2:HA 1:2/ETI	0*
TiO_2:HA 1:2/ALE	0*
TiO_2:HA 1:2/RIS	0*
HA	37.5 $\pm$ 2.5
HA/ETI	0*
HA/ALE	0*
HA/RIS	0*

*0 indicates that water drop completly spread on surface.
Source: Developed by the author.

XPS was used to examine the surface composition in detail, and the results are presented in the following sections. Table 19 presents the atomic concentrations of the studied surfaces obtained from survey measurements. BPs were successfully adsorbed on TiO_2 because of the presence of phosphorous in these samples. In addition, an increase in nitrogen content due to the presence of nitrogen-containing BPs was observed. For samples of pure or HA, the presence of BPs was observed due to an increase in phosphorous concentration and the presence of nitrogen on the surface. For TiO_2:HA 1:1, the decrease in phosphorus was attributed to the substitution of phosphates on HA by phosphates of BPs.

Table 19 – Surface elementary composition from XPS measurements.

Sample	Elements (at%)					
	C 1s	O 1s	N 1s	Ti 2p	Ca 2p	P 2p
TiO_2	32.9	50.1	1.9	15.	-	-
TiO_2/ETI	45.1	40.6	1.8	10.4	-	2.2
TiO_2/ALE	51.8	33.8	3.9	6.1	-	4.4
TiO_2/RIS	64.3	26.6	2.2	6.2	-	0.7
TiO_2:HA 1:1	29.1	49.8	-	13.4	4.1	3.7
TiO_2:HA 1:1/ETI	39.8	43.3	1.2	11.9	1.3	2.5
TiO_2:HA 1:1/ALE	40.1	42.8	1.4	10.1	1.3	4.2
TiO_2:HA 1:1/RIS	31.2	46.6	1.8	10.8	4.6	5.0
TiO_2:HA 1:2	28.3	50.9	-	14.7	3.6	2.5
TiO_2:HA 1:2/ETI	44.6	39.4	-	9.8	2.5	3.8
TiO_2:HA 1:2/ALE	34.7	47.7	0.8	11.0	2.8	3.0
TiO_2:HA 1:2/RIS	28.6	49.1	1.4	11.6	4.7	4.7
HA	50.3	35.0	-	8.4	4.5	1.7
HA/ETI	27.4	51.6	-	12.5	4.3	4.2
HA/ALE	35.2	42.6	0.6	8.3	6.1	7.2
HA/RIS	41.1	35.6	3.2	5.3	6.2	8.6

Source: Developed by the author.

The C 1s high-resolution spectra of the prepared films are displayed in Figure 26. We added contributions (286.2 eV) from P_2C–O moieties, based on the presence or increase in phosphorous concentration. This strategy follows previous investigations on bulk phosphonic acids (DIAS et al., 2022; DIAS et al., 2020; MILOšEV; METIKOš-HUKOVIć; PETROVIć, 2012).

The higher peaks are centered at approximately 285.0, 286.6, and 288.8 eV, for aliphatic carbon, C–O, and O–C=O, respectively (DIAS et al., 2020). A few samples showed a contribution centered at 286.0 eV from C–N; for TiO_2, TiO_2/ETI, and TiO_2:HA 1:1 samples, this was attributed to contamination (a peak at approximately 400.0 eV was observed in the N 1s high-resolution spectra (Figure 48) (DIAS et al., 2020; THEILE-RASCHE et al., 2020; LANDOULSI et al., 2008). In other samples, this peak is due to the presence of nitrogen-containing BPs (see Figure 48). It is possible to observe a decrease in the carboxyl groups on the TiO_2 samples, which is consistent with previous results and indicates competitive adsorption (DIAS et al., 2022). Pure HA samples did not exhibit a decrease in carboxyl groups, similar to pure TiO_2. This is consistent with the adsorption mechanism of BPs on HA surfaces because BPs adsorb on HA mainly through the coordination of Ca^{2+} ions and $–PO_2^{3-}$ moieties [20].

The O 1s high-resolution spectra of the prepared films are displayed in Figure 27. All the spectra show a peak centered at approximately 530 eV from TiO_2 (MOULDER, 1993). The spectra of molecules adsorbed on TiO_2 were fitted based on the bulk octadecylphosphonic acid and etidronate contributions (DIAS et al., 2022; DIAS et al., 2020). For the

Figure 26 – C 1s high-resolution XPS spectra of prepared films. BP (4 mM) was employed for functionalization.

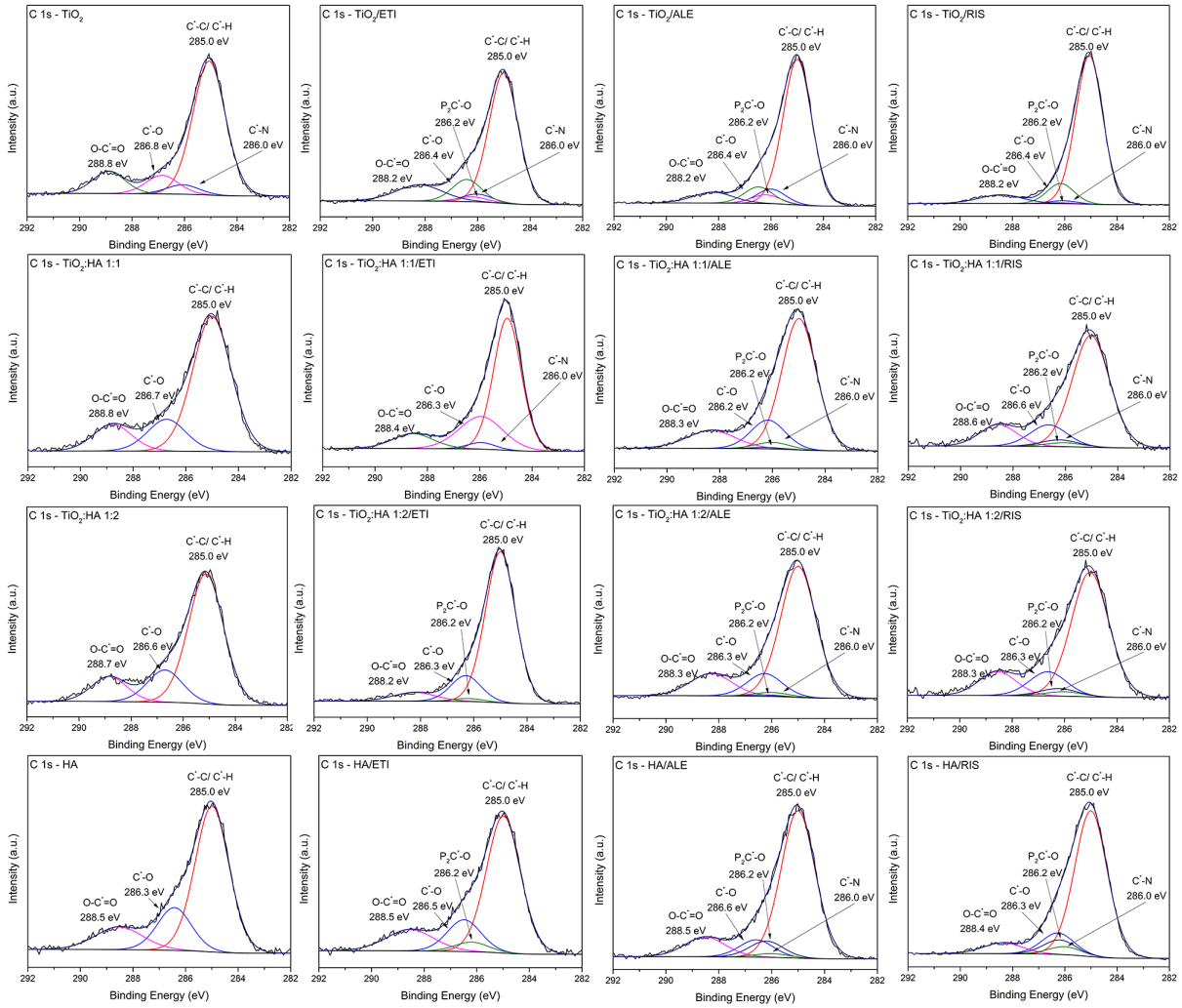

Source: Developed by the author

three adsorbents on TiO_2, we detected contributions at approximately 531.2 eV from organic oxygen, P=O, and Ti–O–P, and at approximately 532.7 eV from P–OH from free phosphonic acid moieties (PETROVIć et al., 2020; THEILE-RASCHE et al., 2020; ZOULALIAN et al., 2010). These results suggest that BPs adsorb equally on rough and smooth titania through the condensation of phosphonates and Ti–OH groups.

Without BPs, samples of pure or containing HA present three peaks. The peaks-additional to TiO_2—are centered at approximately 531.0 eV, from organic oxygen, phosphates, and hydroxyl groups (JERDIOUI et al., 2022; BOLLI et al., 2021; BAI; NAGASHIMA; YAJIMA, 2015); the third peak, centered at approximately 532.7 eV was attributed to free P–OH groups from HA (BAI; NAGASHIMA; YAJIMA, 2015). In the presence of BPs, the same peaks were observed; however, in some samples, there was an increase in the peak centered at 531.0 eV, which was attributed to an increase in the number of -PO_3^{-2} groups due to BP adsorption and the formation of Ti-O-P bonds. The Ca 2p and P 2p spectra

were omitted. Figure 48 shows the N 1s high-resolution spectra of the nitrogen-containing samples. We observed a contribution at approximately 400 eV from C-N contributions, and a contribution from positively charged nitrogen at approximately 401.4 eV (BEAMSON, 1993).

Figure 27 – O 1s high-resolution XPS spectra of prepared films. BP (4 mM) was employed for functionalization.

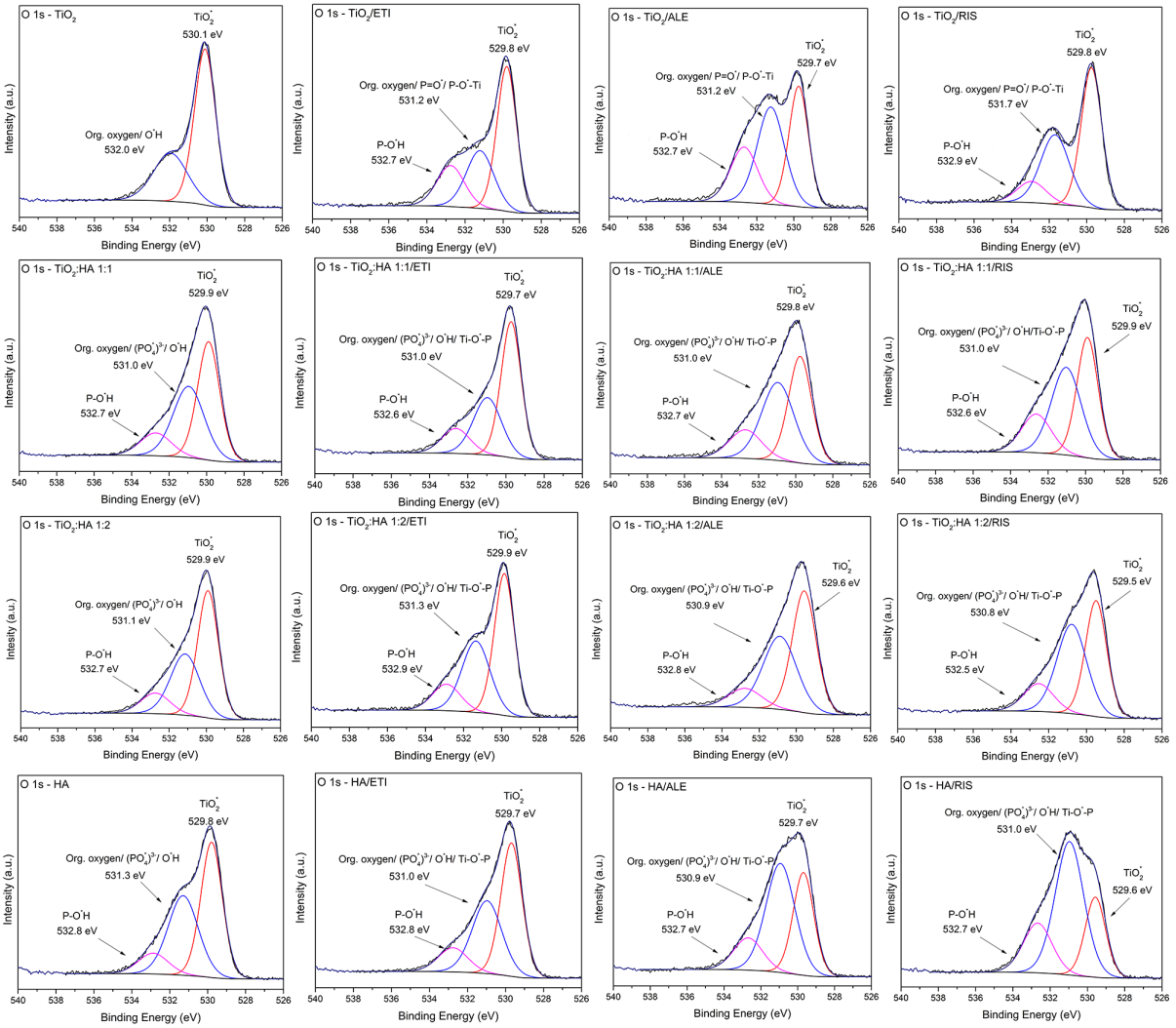

Source: Developed by the author

We accessed the surface nano topography using AFM, and the results are displayed in Figure 28, together with the RMS roughness. For smooth TiO_2, no increase in surface roughness was observed, which is different from the reported results (BRONZE-UHLE et al., 2019a; DIAS et al., 2022; ZHENG; NEOH; KANG, 2017). Except for TiO_2:HA 1:1/ETI, no increase in surface roughness followed by BP adsorption was observed. Even a small increase was expected since it has been reported to increase on HA (OTHMANI et al., 2013).

Previously, we hypothesized that on a smooth surface, BPs follow the surface topography, while rough surfaces approximate the molecules, increasing localized adsorption (DIAS et al., 2022). Because we did not notice an increase in TiO_2 roughness, our hypothesis must be reformulated. Thus, we infer that, in general, BPs may adsorb following TiO_2

topography, while HA surfaces approximate molecules, increasing adsorption through charge interactions.

Figure 28 – AFM images of prepared samples. BP (4 mM) was used for functionalization.

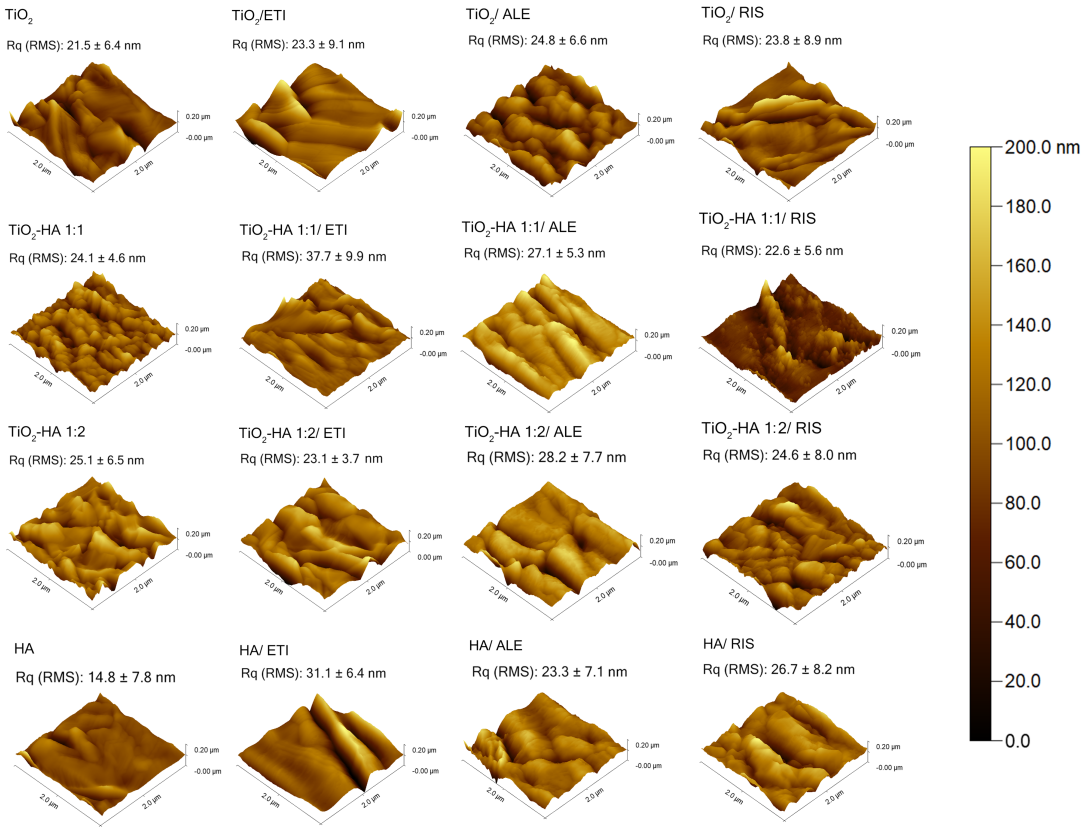

Source: Developed by the author

5.4 Conclusions

In this study, we investigated the adsorption of BPs on TiO_2 particles, TiO_2, HA, and TiO_2+HA films. The adsorption of BPs on TiO_2 particles follows the Freundlich model. The affinity constant of etidronate for anatase was higher than that for rutile, and the opposite was observed for alendronate. Hydroxylation of titania increases the amount adsorbed on the surface of the particle and changes its affinity. We hypothesized that the increase in OH would increase the deprotonation of BPs, leading to higher levels of adsorption. This was also responsible for the preferential adsorption of BPs on titania.

We also investigated the adsorption on TiO_2, HA, and TiO_2+HA films using XRD, confocal microscopy, SEM, water contact angle, XPS, and AFM. The XRD results demonstrated the successful formation of TiO_2, HA, and TiO_2+HA. The film roughness obtained from confocal microscopy was in the range of 27.8–41.7 μm. The water contact angle showed a complete spread of the drop on the surface after BPs adsorption, and the pristine TiO_2:HA

1:1 sample showed the same behavior. XPS showed that molecules were successfully adsorbed by the increase in phosphorus and by the presence of nitrogen in a few samples. AFM showed that surface roughness increased only for HA surfaces, which may be due to charge effects on the surface. To obtain a better understanding of the influence of hydroxylation on adsorption, theoretical studies need to be conducted along with a biological evaluation of similar systems.

5.5 Acknowledgments

This work was financially supported by the São Paulo Research Foundation FAPESP through grants 2018/07520-3, and 2013/07296-2. The authors acknowledge Marina Honorato for her helpful comments and study critique, Giseli Sina for designing the graphical abstract, and LaPTec for water-contact-angle measurements.

6 Microbiological activity of bisphosphonates on titania, hydroxyapatite and composite surfaces

This chapter presents partial results of microbiological assays from samples prepared in Chapter 5. The experiments were performed in collaboration with Raphael Cavalcante Costa, in the group of Prof. Valentim Adelino Ricardo Barão in School of Dentistry at University of Campinas.

6.1 Introduction

Due to their ability to bind to calcium ions and decrease bone resorption bisphosphonates are employed for the treatment of bone diseases (MENEZES et al., 2005). Different researchers investigate their ability to promote bone growth in different ways, such as adsorbed on implant surfaces (BRONZE-UHLE et al., 2019a; MENEZES et al., 2005; PETROVIć et al., 2020; XU et al., 2020).

Surfaces and/or cell culture-containing bisphosphonates demonstrated an increase in osteoblast function (BRONZE-UHLE et al., 2019a; CORRADO; SANPAOLO; CANTATORE, 2017). Further studies presented that bisphosphonate can decrease osteoclast activity (BIGI; BOANINI, 2018). The mechanism of action is still in discussion in literature, however, the studies suggest different mechanisms occurring at once: bisphosphonates produce a cytotoxic ATP analog in contact with osteoclasts; increase of biomarkers such as Col-I, ALP, and osteocalcin on osteoblast; increase differentiation of bone marrow stromal cell in osteoblasts (BIGI; BOANINI, 2018; CUI et al., 2019; ROGERS; MöNKKöNEN; MUNOZ, 2020).

As antibacterial agent results showed that alendronate inhibited the growth of bacteria such as *F. nucleatum* and Gram-negative pigmented bacilli, related to periodontal disease (MENEZES et al., 2005). Risedronate at a concentration of 300-400 μM decrease the biofilm formation of *E. coli* and *Salmonella pullorum* (RESHAMWALA et al., 2016). In other works, bisphosphonates demonstrated antimicrobial activity when allied with other drugs such as vancomycin and zinc ions (PARK et al., 2017; XU et al., 2020). Such activity is important once bisphosphonates alone or allied with other drugs can avoid biofilm formation and promote bone growth increasing biocompatibility.

Here, we evaluated the antibacterial activity and viability of human bone mesenchymal

cells in contact with alendronate and risedronate adsorbed on titania, hydroxyapatite, and composite surfaces. Results demonstrated a tendency of risedronate to decrease *S. aureus* growth and no cytotoxicity effect was observed.

6.2 Materials an methods

Samples were prepared as described in Chapter 5.

6.2.1 Antibacterial activity

Staphylococcus aureus (*S. aureus*, ATCC 14458), a Gram-positive bacteria related to implant infections (ARCIOLA; CAMPOCCIA; MONTANARO, 2018), was used as a model strain to test the antibacterial activity of the bisphosphonate-based coatings. Briefly, loopful of Brain Heart Infusion (BHI)-grown colonies were inoculated into a tube containing 5 mL of sterilized Tryptic Soy Broth (TSB, BD Difco) and grown aerobically overnight at 37℃. In sequence, 1 mL of overnight culture was transferred to 5 mL of fresh TSB and incubated until it had reached the exponential growth phase (4 h; aerobic condition). *S. aureus* bacteria were adjusted to OD_{550nm}= 0.30 ($\pm$ 0.01), which corresponds to 1 × 10^7 colonies forming units-CFU/mL (ASTANEH et al., 2022). The samples (n = 4/group), previously sterilized by UV-light (4 W; 280 nm, Osram Ltd., Berlin, Germany) (COSTA et al., 2020), were placed in a 24-well microplate and aerobically incubated with the bacteria inoculum in TSB (1:10 v/v) for 24 h at 37℃ to form biofilm. Finally, biofilm-coated discs were gently washed in 0.9% NaCl, and a serial dilution of a sonicated suspension was plated in duplicate on BHI agar (Kasvi) for CFU counts (reported as log10 CFU/mL) (AVILA et al., 2019). Data were also expressed as a percentage (%) of bacterial reduction for bisphosphonates-based coatings compared to their respective control group using the following equation:

$$R\% = (B - A).100/B \tag{1}$$

Where R is the ratio of *S. aureus* reduction (%), A is the mean number of viable bacterial colonies after contacting with the control group, and B is the mean number of viable bacterial colonies after contacting with bisphosphonates-based coatings (ASTANEH et al., 2022). This experiment was performed in duplicate but repeated twice as technical repetition.

6.2.2 Minimum inhibitory concentration (MIC)

To examine the possible antibacterial effect of the risedronate isolated, the Minimum Inhibitory Concentration (MIC) was determined by the broth microdilution method based on the Clinical and Laboratory Standards Institute guidelines [M07-A9] (ALEXANDER; CLINICAL; INSTITUTE,). Briefly, risedronate solution (Sigma-Aldrich) starting at 1 mg/mL

(in purified water) was placed into the first well of the plate and serially diluted (ratio 1:2). *S. aureus* colonies from BHI agar plates were suspended in BHI broth to an optical density of 10^7 CFU/mL (OD = 0.30 at 550nm). Then, 100 μL from the final inoculum was added to each microplate well with 100 μL of the serially diluted risedronate sample, totaling a final volume per well of 200 μL and a final cell count of 10^6 CFU/mL. The plates were incubated at 37℃ for 24 h. *S. aureus* culture inoculated onto the plate served as the negative control, and a culture medium free of any other agent was included to check for sterility. The MIC was defined as the lowest concentration of the drug that did not produce detectable OD_{550} until the end of the incubation period. Moreover, the effect of risedronate on *S. aureus* was also tested by agar diffusion test (KRANZ et al., 2019). The correspondent inhibition zones were analyzed after incubation for 24 h at 37℃. Chlorhexidine (Sigma-Aldrich) was used as a standard drug. All assays were carried out in triplicate in two independent experiments.

6.2.3 Cell culture experiments

Human bone mesenchymal cells (hBMSC) that have been extensively investigated for their role in the regenerative and wound healing properties were used to assess the cytocompatibility of bisphosphonate-based coatings. Firstly, hBMSCs (Sigma-Aldrich) were cultured in minimum essential medium eagle–alpha modification (Alpha MEM; Gibco™) supplemented with 10% fetal bovine serum (FBS; Gibco™) and 1% penicillin/streptomycin. Cells were kept in a humidified incubator at 37℃ and 5% CO_2 atmosphere. After reaching confluence, trypsin-ethylenediaminetetraacetic acid (Gibco™) was used to detach the cells. Next, the cells were re-suspended in a culture medium for seeding onto the samples at 2 × 10^4 cells/mL (CORDEIRO et al., 2021).

6.2.4 MTT assay

Cellular metabolic activity was determined at 3 and 7 days by MTT 3-(4,5-dimethylthiazol-2-yl)-2,5-diphenyltetrazolium bromide analysis (BORGES et al., 2022). After the experimental periods, the culture medium was replaced by α-MEM with MTT (5 mg/mL) (Gibco™) at 37℃ and 5% CO_2 atmosphere conditions for 4 h following the manufacturer's recommendation. Subsequently, dimethyl sulfoxide (Sigma-Aldrich) was used to dissolve the formazan crystals. Next, the optical density was verified (VersaMax; Molecular Devices, USA) at a 570 nm wavelength. The tests were performed in triplicate to guarantee reproducibility.

6.2.5 Statistical analysis

GraphPad Prism 8 software was used to perform statistical analyses and graphics. After checking the normality with the Shapiro-Wilk test, the number of CFUs was assessed using one-way ANOVA followed by Tukey's HSD test as a post-hoc technique for multiple

comparisons. Differences from % bacterial reduction were performed using a Bonferroni t-test. All data are plotted as the mean ± standard deviation (SD), and $p < 0.05$ was considered statistically significant.

6.3 Results and discussion

To evaluate the antibacterial activity of bisphosphonate-based coatings on *S. aureus* biofilm viability, an in vitro assay was performed (Figure 29A). *S. aureus* is one of the dominant bacteria in bone infections, causing the majority of osteomyelitis cases by the colonization of the bone and expression of a vast array of virulence factors (JOSSE et al., 2004). The aspects affecting bacterial adhesion to an implant surface are complex and depend on both surface and bacterial properties (COSTA et al., 2020). Herein, it is evident the progressive reduction of CFU from *S. aureus* biofilm is initially dependent on the deposition process, such as 1:1 or 1:2 groups (Figure 29B). Alendronate and risedronate-loaded coatings (1:2 group) significantly reduced almost 2 logs of CFU counts after 24 h of biofilm formation ($p < 0.05$) when compared to HA and TiO_2 surfaces alone. Compared to their controls, bisphosphonate-based coatings showed a higher % of bacterial reduction (Figure 29b'). Apart from the deposition process, the risedronate-containing surface had a noticeable effect compared to the alendronate-containing surface ($p < 0.05$). Quantitatively, the *S. aureus* CFU content was reduced up to 15% on the risedronate-containing surface vs. alendronate–containing surface (e.g., 1:2 steps). Altogether, there seems to be a trend influencing bacterial colonization related to surface chemistry (type of bisphosphonate), surface properties (roughness, charge, wettability, and so), and deposition process (1:1 or 1:2 steps).

Prompted by the effect of risedronate-loaded coating to reduce *S. aureus* colonization, we explored the isolated potential of this bisphosphonate to promote bacterial killing. For this, a MIC assay was conducted to validate this hypothesis. The results demonstrated that regardless of the concentration tested, risedronate did not have bacteriostatic and bactericidal activity against *S. aureus* (Figure 30A). A biofilm reduction higher than 60% was found against *E.coli* (gram-negative bacteria) at a concentration of 300-400 μM of risedronate (RESHAMWALA et al., 2016).

These findings follow the images from the agar diffusion test, in which inhibition zones in the presence of risedronate were not found after 24 h (Figure 30B). Oppositely, chlorhexidine exhibited an evident inhibition zona with 17 mm ($\pm$0.2). This validates the possible effect of risedronate depending on the material's topography and surface properties. Our previous study (DIAS et al., 2022) demonstrated that it is possible to incorporate bisphosphonates on titanium surfaces without changing surface roughness and wettability. For the risedronate, the deprotonation of phosphonates was observed through XPS, which

Figure 29 – *In vitro* antibacterial activity of bisphosphonate-based coatings. (A) Schematic representation of *Staphylococcus aureus* biofilm model used (B) Colony-forming units count (Log10 CFU/mL) of *S. aureus* after 24 h of biofilm formation. (b') Percentage of bacterial reduction (%) of treated surfaces to control. Data are expressed as mean ± standard deviation. Statistically, significant differences are indicated as *p < 0.05 (HSD Tukey and Bonferroni t-test).

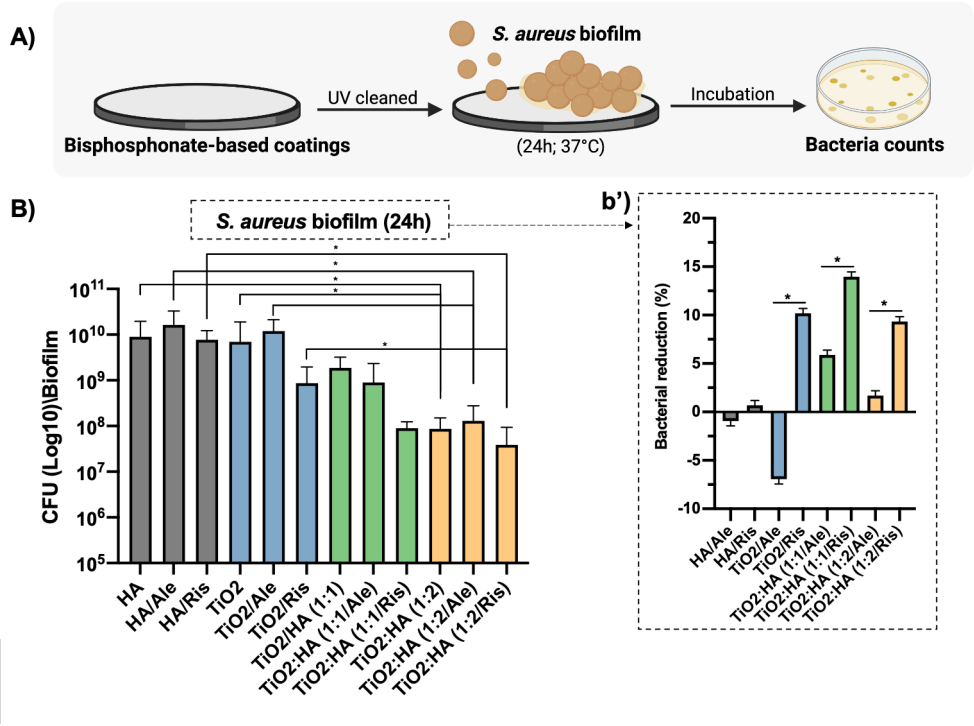

Source: Developed by Raphael cavalcante Costa

promotes positive values for zeta potential at pH from 5.0 to 6.5 (similar values found in bacteria culture medium). In Gram-positive bacteria, such as *S. aureus*, there is no outer membrane, the peptidoglycan cell wall is thick (20–50 nm), and the chains of teichoic acid cross the cell wall with a negatively-charged membrane. Previous studies (HENNINGSEN et al., 2018) have reported that positively charged coatings could inhibit the growth of bacteria due to strong electrostatic interaction and ionic displacement in the bacterial membrane. Therefore, this improved antimicrobial effect for risedronate might be partially associated with its positively charged mechanism. The understanding of how these coatings work, with a non-releasing antibacterial mechanism, still needs to be addressed in future studies.

An appropriate cellular response to implanted surfaces is crucial for tissue integration (BORGES et al., 2022). Therefore, in the current study, we carried out the MTT assay to determine the impact of bisphosphonate-based coatings on cell metabolism. In general, data analysis showed that both bisphosphonate (alendronate and risedronate) presented an increased mitochondrial metabolism over time, suggesting a non-cytotoxic effect, with the risedronate-loaded coating featuring an increased metabolism of hBMSC at day 7. The sample named TiO_2/HA 1:2/RIS demonstrated higher growth on cellular viability after 7 days.

Figure 30 – Determination of the minimum inhibitory concentration of risedronate. (A) MIC of risedronate from 1 mg/mL to 0.001 mg/mL. (B) Agar diffusion test with *S. aureus*. NS = no statistically significant differences among the groups.

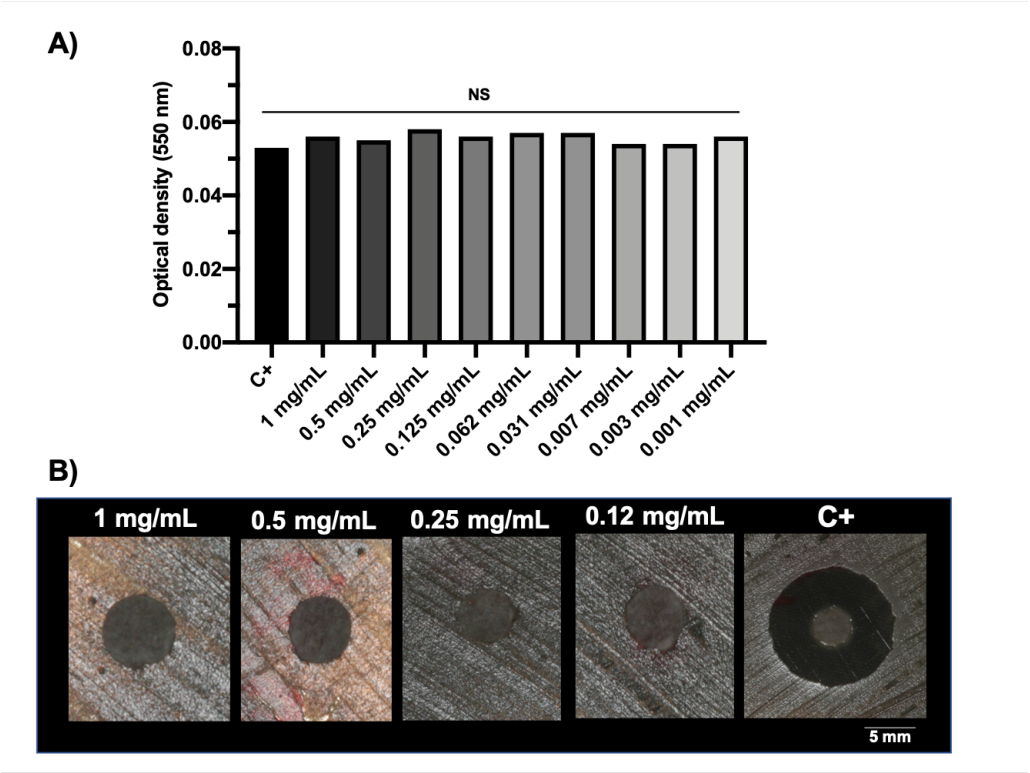

Source: Developed by Raphael cavalcante Costa

Further assays, such as alkaline phosphate are currently being evaluated. These results will complement the cell viability, and indicate differentiation and mineralization induced by the samples.

Figure 31 – MTT assay. Absorbance is expressed as a measure of cell metabolism for hBMSC cells cultured on control and bisphosphonate-based coatings for each deposition process (different colors) in 3 (A) and 7 (B) days of culture. *p < 0.05 (HSD Tukey and Bonferroni t-test).

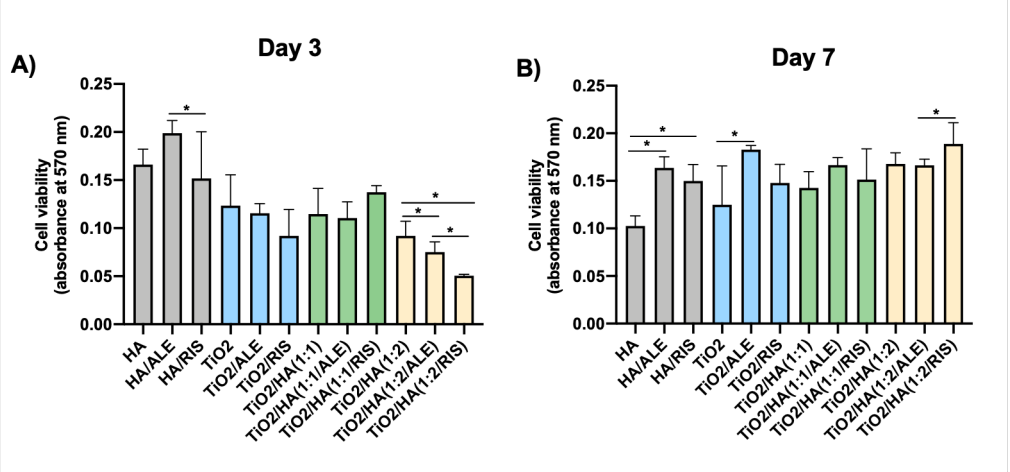

Source: Developed by Raphael cavalcante Costa

6.4 Conclusions

Surface modification using bisphosphonates is a suitable strategy to promote bone growth around implants. Here, we evaluated the antimicrobial activity and cell viability of titanium cp IV with different films functionalized with bisphosphonates. There is a tendency of risedronate to decrease *S. aureus* growth in studied samples, however, this effect was not observed in the MIC assay. This indicates that risedronate can inhibit only gram-negative bacteria, and suggest a synergetic effect between surface roughness and the adsorbed layer. MTT assay with hBMSC demonstrated no cytotoxic effect of prepared samples and a high increase in metabolic activity caused by risedronate. Further investigations to evaluate the cell differentiation and deposition of calcium and phosphorous are under progress.

7 CONCLUSIONS

In the next paragraphs is presented a discussion of the presented articles.

A well-performed characterization is crucial in understanding the physicochemical aspects of surfaces. Although a protocol of necessary techniques is not available since each surface and application demands specific characterization (RATNER; CASTNER, 2020), the first step of this work (see Chapter 3) established a protocol to be applied on the bisphosphonates layers.

Octadecylphosphonic acid (ODPA) and dimethyloctadecyl (3-trimethoxysilylpropyl) ammonium chloride (DMOAP) were immobilized on a smooth titania surface; furthermore, although DMOAP is not similar to bisphosphonates, the results showed a relationship between the layer structure and biological activity. This finding can also be used for BP layers. in other words, the conformation of bisphosphonates on titania and hydroxyapatite surfaces may affect the biological performance.

The characterization of bulk and ODPA layers is a starting point for data interpretation of the BP layers. The XPS results indicated the presence of unbounded phosphonates, even in a monolayer regime. Since there is no evidence in the literature of bisphosphonates monolayer, free phosphonates groups will always be observed. As demonstrated in the zeta potential for ODPA and bisphosphonates layers, free phosphonates play a crucial role in the surface charge. This interpretation can be assured by the measurements of ODPA and etidronate, which are the simplest structures of phosphonic acids. The same is true for water contact angle, as surfaces are hydrophilic mainly due to the exposed P-OH groups, in the case of BP layers.

Bisphosphonate layers were studied through the XPS and zeta potential characterization in Chapter 4, through experimental and theoretical approaches. We evaluated the influence of deprotonation on BPs, our results demonstrated that the reactivity around oxygen increases with the increase of deprotonation. The XPS results demonstrated that the presence of P-OH groups on the surface, as expected. Additionally, -N^+ species were detected, indicating that nitrogen-containing moieties of alendronate and risedronate interact with the hydroxyl groups of titania surfaces. Zeta potential measurements, the first of this type for BPs layers, demonstrated an influence of the phosphonates groups for all bisphosphonates, mainly etidronate, which is only composed of P-OH and CH_3. Owing to the protonated nitrogen-containing groups, alendronate and risedronate exhibited a reduced shift for negative value compared to etidronate.

In Chapter 5 we presented an adsorption curve of bisphosphonates on titania, and characterization of BPs on TiO_2, HA, and composite surfaces. The results showed that

the UV irradiation increases the adsorption of BPs on titania, possibly to an increment in bisphosphonate deprotonation caused by the OH groups. The molecules were successfully adsorbed on the thin films. The positions obtained by the XPS are consistent with the previous investigations. Additionally, we observed a synergistic effect between the adsorbed layer and roughness. Rough samples containing bisphosphonates are more hydrophilic than smooth samples.

Chapter 6 presented a microbiological evaluation of the prepared samples. Furthermore, there is a relationship between the roughness and adsorbed layer. We observed that the adsorbed risedronate can partially inhibit the growth of *S. aureus*; but pure risedronate cannot. Additionally, we did not observe any cytotoxic effect caused by the prepared samples. The presented results are aligned with the general and specific goals, providing a deeper understanding of the bisphosphonates layers.

As conclusions, this thesis presented a detailed characterization of the bisphosphonates layers on different surfaces. Starting from the adsorption of octadecyl phosphonic acid on smooth titania, we evaluated the bisphosphonates on smooth titania, and finally on rough titania. Additionally, we investigated the BPs layers on the hydroxyapatite and mixed films of TiO_2 and HA. Furthermore, we verified the influence of hydroxylation on the BPs adsorption on anatase and rutile.

Bisphosphonates adsorption on the oxide surface is characterized by the presence of free P-OH groups. In addition to promoting hydrophilic behavior, these groups lead to the negative values of zeta potential. The theoretical investigation demonstrated that bisphosphonates are strongly affected by deprotonation. Together with the adsorption curves, we hypothesized that bisphosphonates increase their adsorption on the hydroxylated titania due to the increase of deprotonation, which is caused by the higher number of hydroxyl groups on the surface.

On mixed films, we observed that the addition of hydroxyapatite on titania film leads to more hydrophilic surfaces. As confirmed by the XPS measurements , bisphosphonates were successfully adsorbed on all the prepared surfaces. Concerning topography, we observed that the hydroxyapatite roughness is strongly affected by the bisphosphonates adsorption, unlike titania. The wettability of the rough surfaces is more affected by the presence of bisphosphonates than smooth surfaces. Samples containing risedronate can partially inhibit *S. aureus* growth when immobilized on a film. This suggests that roughness plays a role in antibacterial activity because pure risedronate did not show this effect.

The presented results help to deepen the understanding of the properties of bisphosphonates layers, mainly on the titania surfaces, and provide the basis for the comprehension of the biological performance of such layers. The methodology applied in this study can be used to investigate other bioactive molecules, such as silane and thiol-based molecules. We recommend an investigation of protein adsorption on BP layers. Due to the negative charge,

the BP layers can induce preferential adsorption of proteins. This information can be useful in understanding the bioactivity during *in vivo* investigations. Additionally, we recommend a theoretical investigation of the influence of hydroxylation on bisphosphonates adsorption on oxidized surfaces.

Bibliography

ABTAHI, J.; AGHOLME, F.; SANDBERG, O.; ASPENBERG, P. Effect of local vs. systemic bisphosphonate delivery on dental implant fixation in a model of osteonecrosis of the jaw. *Journal of Dental Research*, v. 92, p. 279–283, 2013. ISSN 00220345.

ADELL, R.; LEKHOLM, U.; ROCKLER, B.; BRANEMARK, P. Review article a i5-year study of osseointegrated implants in the treatment of the edentulous jaw. v. 416, 1981.

ADLHART, C.; VERRAN, J.; AZEVEDO, N. F.; OLMEZ, H.; KEINäNEN-TOIVOLA, M. M.; GOUVEIA, I.; MELO, L. F.; CRIJNS, F. Surface modifications for antimicrobial effects in the healthcare setting: a critical overview. *Journal of Hospital Infection*, v. 99, p. 239–249, 2018. ISSN 15322939.

AGHABOZORG, H.; SOHRABI, B.; MASHKOURI, S.; AGHABOZORG, H. R. Ab initio dft study of bisphosphonate derivatives as a drug for inhibition of cancer: Nmr and nqr parameters. *Journal of Molecular Modeling*, v. 18, p. 929–936, 2012. ISSN 16102940.

AGHALOO, T.; PI-ANFRUNS, J.; MOSHAVERINIA, A.; SIM, D.; GROGAN, T.; HADAYA, D. The effects of systemic diseases and medications on implant osseointegration: A systematic review. *The International Journal of Oral Maxillofacial Implants*, v. 34, p. s35–s49, 2019. ISSN 08822786.

AGUIAR, K. M. R. de; ALVES, V. S.; NOESKE, P.-L. M.; RISCHKA, K.; PORTELA, M. B.; FERREIRA-PEREIRA, A.; RODRIGUES-FILHO, U. P. *Hybrid films based on nonisocyanate polyurethanes with antimicrobial activity*. [S.l.: s.n.], 2019. 77-116 p. ISBN 9780128184356.

AL-ZAIDI, E.; FAN, X. Effect of aqueous electrolyte concentration and valency on contact angle on flat glass surfaces and inside capillary glass tubes. *Colloids and Surfaces A: Physicochemical and Engineering Aspects*, Elsevier, v. 543, p. 1–8, 2018. ISSN 18734359. Disponível em: <https://doi.org/10.1016/j.colsurfa.2018.01.045>.

ALBANO, C. S.; GOMES, A. M.; FELTRAN, G. da S.; FERNANDES, C. J. da C.; TRINO, L. D.; ZAMBUZZI, W. F.; LISBOA-FILHO, P. N. Biofunctionalization of titanium surfaces with alendronate and albumin modulates osteoblast performance. *Heliyon*, v. 6, p. e04455, 2020. ISSN 24058440.

ALEXANDER, B. D.; CLINICAL; INSTITUTE, L. S. *Reference method for broth dilution antifungal susceptibility testing of yeasts*. [S.l.: s.n.]. 34 p. ISBN 1562388266.

ALMUQRIN, A. H.; WJIHI, S.; AOUAINI, F.; LAMINE, A. B. New insights on physico-chemical investigation of bisphosphonate adsorption isotherm into apatite substrate using statistical physics treatment. *Journal of Molecular Liquids*, Elsevier B.V., v. 310, p. 113230, 2020. ISSN 01677322. Disponível em: <https://doi.org/10.1016/j.molliq.2020.113230>.

ALVES, G. G.; LAVARDA, F. C.; GRAEFF, C. F.; BATAGIN-NETO, A. Reactivity of eumelanin building blocks: A dft study of monomers and dimers. *Journal of Molecular Graphics and Modelling*, Elsevier Ltd, v. 98, p. 107609, 2020. ISSN 18734243. Disponível em: <https://doi.org/10.1016/j.jmgm.2020.107609>.

ANGELIS, F. D.; PAPI, P.; MENCIO, F.; ROSELLA, D.; CARLO, S. D.; POMPA, G. Implant survival and success rates in patients with risk factors: Results from a long-term retrospective study with a 10 to 18 years follow-up. *European Review for Medical and Pharmacological Sciences*, v. 21, p. 433–437, 2017. ISSN 11283602.

ANTONUCCI, J. M.; ZEIGER, D. N.; TANG, K.; LIN-GIBSON, S.; FOWLER, B. O.; LIN, N. J. Synthesis and characterization of dimethacrylates containing quaternary ammonium functionalities for dental applications. *Dental Materials*, v. 28, p. 219–228, 2 2012. ISSN 01095641. Disponível em: <https://www.ncbi.nlm.nih.gov/pmc/articles/PMC3624763/pdf/nihms412728.pdfhttps://linkinghub.elsevier.com/retrieve/pii/S0109564111008670>.

ARCIOLA, C. R.; CAMPOCCIA, D.; MONTANARO, L. *Implant infections: Adhesion, biofilm formation and immune evasion*. [S.l.]: Nature Publishing Group, 2018. 397-409 p.

ARIFIN, A.; SULONG, A. B.; MUHAMAD, N.; SYARIF, J.; RAMLI, M. I. Material processing of hydroxyapatite and titanium alloy (ha/ti) composite as implant materials using powder metallurgy: A review. *Materials and Design*, Elsevier Ltd, v. 55, p. 165–175, 2014. ISSN 18734197. Disponível em: <http://dx.doi.org/10.1016/j.matdes.2013.09.045>.

ASRI, L. A.; CRISMARU, M.; ROEST, S.; CHEN, Y.; IVASHENKO, O.; RUDOLF, P.; TILLER, J. C.; MEI, H. C. V. D.; LOONTJENS, T. J.; BUSSCHER, H. J. A shape-adaptive, antibacterial-coating of immobilized quaternary-ammonium compounds tethered on hyperbranched polyurea and its mechanism of action. *Advanced Functional Materials*, v. 24, p. 346–355, 2014. ISSN 1616301X.

ASTANEH, S. H.; BHATIA, H.; NAGAY, B. E.; BARãO, V. A. R.; JURSICH, G.; SUKOTJO, C.; TAKOUDIS, C. G. Is atomic layer deposition of silver possible on n95 masks? *Applied Surface Science*, v. 591, p. 153195, 7 2022. ISSN 01694332. Disponível em: <https://linkinghub.elsevier.com/retrieve/pii/S0169433222007565>.

AVILA, E. D. de; CASTRO, A. G.; TAGIT, O.; KROM, B. P.; LöWIK, D.; WELL, A. A. van; BANNENBERG, L. J.; VERGANI, C. E.; BEUCKEN, J. J. van den. Anti-bacterial efficacy via drug-delivery system from layer-by-layer coating for percutaneous dental implant components. *Applied Surface Science*, Elsevier B.V., v. 488, p. 194–204, 9 2019. ISSN 01694332.

BAI, J.; NAGASHIMA, T.; YAJIMA, T. Xps study of apatite formed from simulated body fluid on a titanium substrate surface nitrided by an atmospheric pressure nitrogen microwave plasma. *Journal of Photopolymer Science and Technology*, The Society of Photopolymer Science and Technology (SPST), v. 28, n. 3, p. 455–459, 2015.

BEAMSON, D. B. G. High resolution xps of organic polymers, the scienta esca300 database. WILEY, v. 5, p. 778–778, 10 1993. ISSN 0935-9648. Disponível em: <http://doi.wiley.com/10.1002/adma.19930051035>.

BECKE, A. D. Density-functional thermochemistry. iii. the role of exact exchange. *The Journal of Chemical Physics*, v. 98, p. 5648–5652, 1993. ISSN 00219606.

BEDOYA, D. A.; VASTI, C.; ROJAS, R.; GIACOMELLI, C. E. Risedronate functionalized layered double hydroxides nanoparticles with bone targeting capabilities. *Applied Clay Science*, Elsevier B.V., v. 141, p. 257–264, 2017. ISSN 01691317. Disponível em: <http://dx.doi.org/10.1016/j.clay.2017.03.001>.

BELKHIR, K.; LACROIX, M.; JAMSHIDIAN, M.; SALMIERI, S.; JEGAT, C.; TAHA, M. Evaluation of antibacterial activity of branched quaternary ammonium grafted green polymers. *Food Packaging and Shelf Life*, v. 12, p. 28–41, 2017. ISSN 22142894.

BEN-ARFA, B. A.; SALVADO, I. M.; FERREIRA, J. M.; PULLAR, R. C. Novel route for rapid sol-gel synthesis of hydroxyapatite, avoiding ageing and using fast drying with a 50-fold to 200-fold reduction in process time. *Materials Science and Engineering C*, Elsevier B.V., v. 70, p. 796–804, 2017. ISSN 09284931. Disponível em: <http://dx.doi.org/10.1016/j.msec.2016.09.054>.

BIGI, A.; BOANINI, E. Calcium phosphates as delivery systems for bisphosphonates. *Journal of Functional Biomaterials*, v. 9, 2018. ISSN 20794983.

BLOCK, M. S.; CHRISTENSEN, B. J.; MERCANTE, D. E.; CHAPPLE, A. G. What factors are associated with implant failure? *Journal of Oral and Maxillofacial Surgery*, American Association of Oral and Maxillofacial Surgeons, v. 79, p. 91–97, 2021. ISSN 15315053. Disponível em: <https://doi.org/10.1016/j.joms.2020.08.023>.

BOETHLING, R. S. Environmental fate and toxicity in wastewater treatment of quaternary ammonium surfactants. *Water Research*, v. 18, p. 1061–1076, 1984. ISSN 00431354.

BOLLI, E.; KACIULIS, S.; MEZZI, A.; AMBROGI, V.; NOCCHETTI, M.; LATTERINI, L.; MICHELE, A. D.; PADELETTI, G. Hydroxyapatite functionalized calcium carbonate composites with ag nanoparticles: An integrated characterization study. *Nanomaterials*, MDPI, v. 11, 9 2021. ISSN 20794991.

BORCHERDING, K.; MARX, D.; GäTJEN, L.; BORMANN, N.; WILDEMANN, B.; SPECHT, U.; SALZ, D.; THIEL, K.; GRUNWALD, I. Burst release of antibiotics combined with long-term release of silver targeting implant-associated infections: Design, characterization and in vitro evaluation of novel implant hybrid surface. *Materials*, v. 12, p. 1–13, 2019. ISSN 19961944.

BORGES, M. H.; NAGAY, B. E.; COSTA, R. C.; SACRAMENTO, C. M.; RUIZ, K. G.; LANDERS, R.; BEUCKEN, J. J. van den; FORTULAN, C. A.; RANGEL, E. C.; CRUZ, N. C. da; BARãO, V. A. A tattoo-inspired electrosynthesized polypyrrole film: crossing the line toward a highly adherent film for biomedical implant applications. *Materials Today Chemistry*, Elsevier Ltd, v. 26, 12 2022. ISSN 24685194.

BORGHI, F.; VYAS, V.; PODESTà, A.; MILANI, P. Nanoscale roughness and morphology affect the isoelectric point of titania surfaces. *PLoS ONE*, v. 8, p. 1–14, 2013. ISSN 19326203.

BOSCO, R.; IAFISCO, M.; TAMPIERI, A.; JANSEN, J. A.; LEEUWENBURGH, S. C.; BEUCKEN, J. J. V. D. Hydroxyapatite nanocrystals functionalized with alendronate as bioactive components for bone implant coatings to decrease osteoclastic activity. *Applied Surface Science*, Elsevier B.V., v. 328, p. 516–524, 2015. ISSN 01694332. Disponível em: <http://dx.doi.org/10.1016/j.apsusc.2014.12.072>.

BRAUNWARTH, H.; BRILL, F. H. Antimicrobial efficacy of modern wound dressings: Oligodynamic bactericidal versus hydrophobic adsorption effect. *Wound Medicine*, Elsevier B.V., v. 5, p. 16–20, 2014. ISSN 22139095. Disponível em: <http://dx.doi.org/10.1016/j.wndm.2014.04.003>.

BRONZE-UHLE, E. S.; DIAS, L. F.; TRINO, L. D.; MATOS, A. A.; OLIVEIRA, R. C. de; LISBOA-FILHO, P. N. Physicochemical bisphosphonate immobilization on titanium dioxide thin films surface by uv radiation for bio-application. *Surface and Coatings Technology*, Elsevier, v. 357, p. 36–47, 2019. ISSN 02578972. Disponível em: <https://doi.org/10.1016/j.surfcoat.2018.09.038>.

BRONZE-UHLE, E. S.; DIAS, L. F.; TRINO, L. D.; MATOS, A. A.; OLIVEIRA, R. C. de; LISBOA-FILHO, P. N. *Physicochemical characterization of albumin immobilized on different TiO2 surfaces for use in implant materials*. 2019. 39-50 p.

BRUNETTE, D. M.; TENGVALL, P.; TEXTOR, M.; THOMSEN, P. *Titanium in Medicine*. [s.n.], 2001. ISSN 0954-4119. ISBN 978-3-642-63119-1. Disponível em: <http://link.springer.com/10.1007/978-3-642-56486-4>.

CAMPOSEO, A.; MARAGò, O. M.; FAZIO, B.; KLöTER, B.; MESCHEDE, D.; RASBACH, U.; WEBER, C.; ARIMONDO, E. Resist-assisted atom lithography with group iii elements. *Applied Physics B: Lasers and Optics*, v. 85, p. 487–491, 2006. ISSN 09462171.

CAVALCANTI, W. L.; MOUTSOMPEGKA, E.; TSERPES, K.; MALINOWSKI, P. H.; OSTACHOWICZ, W. M.; ECAULT, R.; GRUNDMANN, N.; TORNOW, C.; NOESKE, M.; SCHIFFELS, P.; MAYER, B. *Adhesive Bonding of Aircraft Composite Structures*. Springer International Publishing, 2021. 331-350 p. ISBN 9783319928104. Disponível em: <http://dx.doi.org/10.1007/978-3-319-92810-4_6>.

CHA, M.; LEE, K. M.; LEE, J. H. Positive effects of bisphosphonates on osteogenic differentiation in patient-derived mesenchymal stem cells for the treatment of osteoporosis. *Tissue Engineering and Regenerative Medicine*, v. 15, p. 467–475, 2018. ISSN 22125469.

CHEN, C.; XIA, M.; WU, L.; ZHOU, C.; WANG, F. Modeling the interaction of seven bisphosphonates with the hydroxyapatite(100) face. *Journal of Molecular Modeling*, v. 18, p. 4007–4012, 2012. ISSN 16102940.

CHEN, D.; WU, H. K. Y.; NADERI-GOHAR, S.; WU, Y.; HUANG, Y.; NIE, H. Y. An extremely rapid dip-coating method for self-assembly of octadecylphosphonic acid and its thermal stability on an aluminum film. *Journal of Materials Chemistry C*, Royal Society of Chemistry, v. 2, p. 9941–9948, 2014. ISSN 20507526.

CHEN, S.; GUO, R.; XIE, C.; LIANG, Q.; XIAO, X. Biomimetic mineralization of nanocrystalline hydroxyapatites on aminated modified polylactic acid microspheres to develop a novel drug delivery system for alendronate. *Materials Science and Engineering C*, Elsevier Ltd, v. 110, 5 2020. ISSN 18730191.

CHEN, W.; OH, S.; ONG, A. P.; OH, N.; LIU, Y.; COURTNEY, H. S.; APPLEFORD, M.; ONG, J. L. Antibacterial and osteogenic properties of silver-containing hydroxyapatite coatings produced using a sol gel process. *Journal of Biomedical Materials Research - Part A*, v. 82, p. 899–906, 9 2007. ISSN 15493296.

CHIRLIAN, L. E.; FRANCL, M. M. Atomic charges derived from electrostatic potentials: A detailed study. *Journal of Computational Chemistry*, v. 8, p. 894–905, 1987. ISSN 1096987X.

CHOUIRFA, H.; BOULOUSSA, H.; MIGONNEY, V.; FALENTIN-DAUDRé, C. Review of titanium surface modification techniques and coatings for antibacterial applications. *Acta*

Biomaterialia, Acta Materialia Inc., v. 83, p. 37–54, 2019. ISSN 18787568. Disponível em: <https://doi.org/10.1016/j.actbio.2018.10.036>.

CICCO, S. R.; VONA, D.; LEONE, G.; GIGLIO, E. D.; BONIFACIO, M. A.; COMETA, S.; FIORE, S.; PALUMBO, F.; RAGNI, R.; FARINOLA, G. M. In vivo functionalization of diatom biosilica with sodium alendronate as osteoactive material. *Materials Science and Engineering C*, Elsevier, v. 104, p. 109897, 2019. ISSN 18730191. Disponível em: <https://doi.org/10.1016/j.msec.2019.109897>.

CORDEIRO, J. M.; NAGAY, B. E.; DINI, C.; SOUZA, J. G.; RANGEL, E. C.; CRUZ, N. C. da; YANG, F.; BEUCKEN, J. J. van den; BARãO, V. A. Copper source determines chemistry and topography of implant coatings to optimally couple cellular responses and antibacterial activity. *Materials Science and Engineering C*, Elsevier Ltd, 2021. ISSN 18730191.

CORRADO, A.; SANPAOLO, E. R.; CANTATORE, F. P. Bisphosphonates and osteoblast function. *Journal of Gerontology and Geriatrics*, v. 65, p. 150–151, 2017. ISSN 24996564.

CORRALES-UREñA, Y. R.; SOUZA-SCHIABER, Z.; LISBOA-FILHO, P. N.; MARQUENET, F.; NOESKE, P.-L. M.; GäTJEN, L.; RISCHKA, K. Functionalization of hydrophobic surfaces with antimicrobial peptides immobilized on a bio-interfactant layer. *RSC Advances*, v. 10, p. 376–386, 2020. ISSN 2046-2069. Disponível em: <http://xlink.rsc.org/?DOI=C9RA07380A>.

COSTA, R. C.; SOUZA, J. G.; CORDEIRO, J. M.; BERTOLINI, M.; AVILA, E. D. de; LANDERS, R.; RANGEL, E. C.; FORTULAN, C. A.; RETAMAL-VALDES, B.; CRUZ, N. C. da; FERES, M.; BARãO, V. A. Synthesis of bioactive glass-based coating by plasma electrolytic oxidation: Untangling a new deposition pathway toward titanium implant surfaces. *Journal of Colloid and Interface Science*, Academic Press Inc., v. 579, p. 680–698, 11 2020. ISSN 10957103.

CUI, Y.; ZHU, T.; LI, D.; LI, Z.; LENG, Y.; JI, X.; LIU, H.; WU, D.; DING, J. Bisphosphonate-functionalized scaffolds for enhanced bone regeneration. *Advanced Healthcare Materials*, v. 8, p. 1–21, 2019. ISSN 21922659.

DAI, C.; LIU, N.; CAO, Y.; CHEN, Y.; LU, F.; FENG, L. Fast formation of superhydrophobic octadecylphosphonic acid (odpa) coating for self-cleaning and oil/water separation. *Soft Matter*, Royal Society of Chemistry, v. 10, p. 8116–8121, 2014. ISSN 17446848. Disponível em: <http://dx.doi.org/10.1039/C4SM01616E>.

D'ELIA, S.; BARNA, V.; SCARAMUZZA, N.; STRANGI, G.; BARTOLINO, R. The influence of drying temperature on the close packed structure of silanized monolayers deposited on indium tin oxide (ito) substrates. *Journal of Materials Research*, v. 24, p. 2784–2794, 2009. ISSN 08842914.

DENNINGTON, R.; KEITH, T. A.; MILLAM, J. M. *GaussView Version 6*. 2019. Semichem Inc. Shawnee Mission KS.

DIAS, L. F. G.; RHEINHEIMER, J. P. C.; GOMES, O. P.; NOESKE, M.; STAMBOROSKI, S.; BRONZE-UHLE, E. S.; MAINARDI, M. C.; CAVALCANTI, W. L.; NETO, A. B.; LISBOA-FILHO, P. N. Bisphosphonates on smooth tio ₂ : modeling and characterization. *ChemistrySelect*, v. 7, 5 2022. ISSN 2365-6549. Disponível em: <https://onlinelibrary.wiley.com/doi/10.1002/slct.202200286>.

DIAS, L. F. G.; STAMBOROSKI, S.; NOESKE, M.; SALZ, D.; RISCHKA, K.; PEREIRA, R.; MAINARDI, M. do C.; CARDOSO, M. H.; WIESING, M.; BRONZE-UHLE, E. S.; LINS, R. B. E.; LISBOA-FILHO, P. N. New details of assembling bioactive films from dispersions of amphiphilic molecules on titania surfaces. *RSC Advances*, Royal Society of Chemistry, v. 10, p. 39854–39869, 2020. ISSN 2046-2069. Disponível em: <http://xlink.rsc.org/?DOI=D0RA06511K>.

DIEBOLD, U. Structure and properties of tio2 surfaces: a brief review. *Applied physics A*, Springer, v. 76, n. 5, p. 681–687, 2003.

DIETRICH, P. M.; GLAMSCH, S.; EHLERT, C.; LIPPITZ, A.; KULAK, N.; UNGER, W. E. Synchrotron-radiation xps analysis of ultra-thin silane films: Specifying the organic silicon. *Applied Surface Science*, Elsevier B.V., v. 363, p. 406–411, 2016. ISSN 01694332. Disponível em: <http://dx.doi.org/10.1016/j.apsusc.2015.12.052>.

DOGRA, P.; DHARELA, R.; CHAUHAN, G.; GUPTA, R.; AZMI, W. Structure-property relationship in antimicrobial polymers synthesized by chemo-enzymatic route. *Procedia Chemistry*, v. 4, p. 208–215, 2012. ISSN 18766196. Disponível em: <http://dx.doi.org/10.1016/j.proche.2012.06.029>.

DOLCI, L. S.; PANZAVOLTA, S.; TORRICELLI, P.; ALBERTINI, B.; SICURO, L.; FINI, M.; BIGI, A.; PASSERINI, N. *Modulation of Alendronate release from a calcium phosphate bone cement: An in vitro osteoblast-osteoclast co-culture study*. 2019. 245-255 p.

DRAKE, M. T.; CLARKE, B. L.; KHOSLA, S. Bisphosphonates: Mechanism of action and role in clinical practice. *Mayo Clinic Proceedings*, v. 83, p. 1032–1045, 2008. ISSN 00256196.

ELENA, P.; MIRI, K. Formation of contact active antimicrobial surfaces by covalent grafting of quaternary ammonium compounds. *Colloids and Surfaces B: Biointerfaces*, Elsevier, v. 169, p. 195–205, 2018. ISSN 18734367. Disponível em: <https://doi.org/10.1016/j.colsurfb.2018.04.065>.

ELIAZ, N.; SHMUELI, S.; SHUR, I.; BENAYAHU, D.; ARONOV, D.; ROSENMAN, G. The effect of surface treatment on the surface texture and contact angle of electrochemically deposited hydroxyapatite coating and on its interaction with bone-forming cells. *Acta Biomaterialia*, Elsevier Ltd, v. 5, p. 3178–3191, 2009. ISSN 17427061.

FABRE, H.; MERCIER, D.; GALTAYRIES, A.; PORTET, D.; DELORME, N.; BARDEAU, J. F. Impact of hydrophilic and hydrophobic functionalization of flat tio 2 /ti surfaces on proteins adsorption. *Applied Surface Science*, v. 432, p. 15–21, 2018. ISSN 01694332.

FERNáNDEZ, D.; ORTEGA-CASTRO, J.; FRAU, J. Theoretical study of the deposition and adsorption of bisphosphonates on the 001 hydroxyapatite surface: Implications in the pathological crystallization inhibition and the bone antiresorptive action. *Applied Surface Science*, Elsevier B.V., v. 392, p. 204–214, 2017. ISSN 01694332. Disponível em: <http://dx.doi.org/10.1016/j.apsusc.2016.09.029>.

FERNáNDEZ, D.; ORTEGA-CASTRO, J.; FRAU, J. Theoretical study of the deposition and adsorption of bisphosphonates on the 001 hydroxyapatite surface : Implications in the pathological crystallization inhibition and the bone antiresorptive action. *Applied Surface Science*, v. 392, p. 204–214, 2018.

FERRARIS, S.; CAZZOLA, M.; PERETTI, V.; STELLA, B.; SPRIANO, S. Zeta potential measurements on solid surfaces for in vitro biomaterials testing: Surface charge, reactivity upon contact with fluids and protein absorption. *Frontiers in Bioengineering and Biotechnology*, v. 6, p. 1–7, 2018. ISSN 22964185.

FERREIRA-NETO, E. P.; ULLAH, S.; SIMõES, M. B.; PERISSINOTTO, A. P.; VICENTE, F. S. de; NOESKE, P. L. M.; RIBEIRO, S. J.; RODRIGUES-FILHO, U. P. Solvent-controlled deposition of titania on silica spheres for the preparation of sio 2 @tio 2 core@shell nanoparticles with enhanced photocatalytic activity. *Colloids and Surfaces A: Physicochemical and Engineering Aspects*, Elsevier, v. 570, p. 293–305, 2019. ISSN 18734359.

FORMAN, M. E.; JENNINGS, M. C.; WUEST, W. M.; MINBIOLE, K. P. Building a better quaternary ammonium compound (qac): Branched tetracationic antiseptic amphiphiles. *ChemMedChem*, v. 11, p. 1401–1405, 2016. ISSN 18607187.

FORTE, L.; SARDA, S.; COMBES, C.; BROUILLET, F.; GAZZANO, M.; MARSAN, O.; BOANINI, E.; BIGI, A. Hydroxyapatite functionalization to trigger adsorption and release of risedronate. *Colloids and Surfaces B: Biointerfaces*, Elsevier, v. 160, p. 493–499, 12 2017. ISSN 0927-7765. Disponível em: <https://www.sciencedirect.com/science/article/pii/S0927776517306331>.

FORTE, L.; SARDA, S.; TORRICELLI, P.; COMBES, C.; BROUILLET, F.; MARSAN, O.; SALAMANNA, F.; FINI, M.; BOANINI, E.; BIGI, A. Multifunctionalization modulates hydroxyapatite surface interaction with bisphosphonate: antiosteoporotic and antioxidative stress materials. *ACS Biomaterials Science and Engineering*, v. 5, p. 3429–3439, 2019. ISSN 23739878.

FRISCH, M. J.; TRUCKS, G. W.; SCHLEGEL, H. B.; SCUSERIA, G. E.; ROBB, M. a.; CHEESEMAN, J. R.; SCALMANI, G.; BARONE, V.; PETERSSON, G. a.; NAKATSUJI, H.; LI, X.; CARICATO, M.; MARENICH a. V.; BLOINO, J.; JANESKO, B. G.; GOMPERTS, R.; MENNUCCI, B.; HRATCHIAN, H. P.; ORTIZ, J. V.; IZMAYLOV a. F.; SONNENBERG, J. L.; WILLIAMS; DING, F.; LIPPARINI, F.; EGIDI, F.; GOINGS, J.; PENG, B.; PETRONE, A.; HENDERSON, T.; RANASINGHE, D.; ZAKRZEWSKI, V. G.; GAO, J.; REGA, N.; ZHENG, G.; LIANG, W.; HADA, M.; EHARA, M.; TOYOTA, K.; FUKUDA, R.; HASEGAWA, J.; ISHIDA, M.; NAKAJIMA, T.; HONDA, Y.; KITAO, O.; NAKAI, H.; VREVEN, T.; THROSSELL, K.; JR., J. a. M.; PERALTA, J. E.; OGLIARO, F.; BEARPARK, M. J.; HEYD, J. J.; BROTHERS, E. N.; KUDIN, K. N.; STAROVEROV, V. N.; KEITH, T. a.; KOBAYASHI, R.; NORMAND, J.; RAGHAVACHARI, K.; RENDELL a. P.; BURANT, J. C.; IYENGAR, S. S.; TOMASI, J.; COSSI, M.; MILLAM, J. M.; KLENE, M.; ADAMO, C.; CAMMI, R.; OCHTERSKI, J. W.; MARTIN, R. L.; MOROKUMA, K.; FARKAS, O.; FORESMAN, J. B.; FOX, D. J. *Gaussian 16*. 2016. Gaussian 16, Revision C.01, Gaussian, Inc., Wallin p.

GAO, F.; SHERWOOD, P. M. Photoelectron spectroscopic studies of the formation of hydroxyapatite films on titanium pretreated with etidronic acid. *Surface and Interface Analysis*, v. 45, p. 742–750, 2013. ISSN 01422421.

GEETHA, M.; SINGH, A. K.; ASOKAMANI, R.; GOGIA, A. K. Ti based biomaterials, the ultimate choice for orthopaedic implants - a review. *Progress in Materials Science*, Elsevier Ltd, v. 54, p. 397–425, 2009. ISSN 00796425. Disponível em: <http://dx.doi.org/10.1016/j.pmatsci.2008.06.004>.

GOUZMAN, I.; DUBEY, M.; CAROLUS, M. D.; SCHWARTZ, J.; BERNASEK, S. L. Monolayer vs. multilayer self-assembled alkylphosphonate films: X-ray photoelectron spectroscopy studies. *Surface Science*, v. 600, p. 773–781, 2006. ISSN 00396028.

GRACE, J. L.; HUANG, J. X.; CHEAH, S. E.; TRUONG, N. P.; COOPER, M. A.; LI, J.; DAVIS, T. P.; QUINN, J. F.; VELKOV, T.; WHITTAKER, M. R. Antibacterial low molecular weight cationic polymers: Dissecting the contribution of hydrophobicity, chain length and charge to activity. *RSC Advances*, v. 6, p. 15469–15477, 2016. ISSN 20462069.

GUAZZO, R.; SBRICOLI, L.; RICCI, S.; BRESSAN, E.; PIATTELLI, A.; IACULLI, F. Medication-related osteonecrosis of the jaw and dental implants failures: A systematic review. *Journal of Oral Implantology*, v. 43, p. 51–57, 2017. ISSN 15481336.

GUNJI, T.; KASAHARA, T.; ABE, Y. Crystallization behavior of sich-tich ceramics derived from titanosiloxanes on pyrolysis. *Journal of Sol-Gel Science and Technology*, v. 13, p. 975–979, 1999. ISSN 09280707.

HAN, J. Y.; YU, Z. T.; ZHOU, L. Hydroxyapatite/titania composite bioactivity coating processed by sol-gel method. *Applied Surface Science*, v. 255, p. 455–458, 2008. ISSN 01694332.

HANAWA, T. A comprehensive review of techniques for biofunctionalization of titanium. *Journal of Periodontal and Implant Science*, v. 41, p. 263–272, 2011. ISSN 20932278.

HANAWA, T. Titanium-tissue interface reaction and its control with surface treatment. *Frontiers in Bioengineering and Biotechnology*, v. 7, 2019. ISSN 22964185.

HARUN, W. S.; ASRI, R. I.; ALIAS, J.; ZULKIFLI, F. H.; KADIRGAMA, K.; GHANI, S. A.; SHARIFFUDDIN, J. H. A comprehensive review of hydroxyapatite-based coatings adhesion on metallic biomaterials. *Ceramics International*, v. 44, p. 1250–1268, 2018. ISSN 02728842.

HE, G.; HU, J.; WEI, S. C.; LI, J. H.; LIANG, X. H.; LUO, E. Surface modification of titanium by nano-tio 2 /ha bioceramic coating. *Applied Surface Science*, v. 255, p. 442–445, 2008. ISSN 01694332.

HE, W.; ZHANG, Y.; LI, J.; GAO, Y.; LUO, F.; TAN, H.; WANG, K.; FU, Q. A novel surface structure consisting of contact-active antibacterial upper-layer and antifouling sub-layer derived from gemini quaternary ammonium salt polyurethanes. *Scientific Reports*, Nature Publishing Group, v. 6, p. 1–9, 2016. ISSN 20452322.

HENNINGSEN, A.; SMEETS, R.; HEUBERGER, R.; JUNG, O. T.; HANKEN, H.; HEILAND, M.; CACACI, C.; PRECHT, C. Changes in surface characteristics of titanium and zirconia after surface treatment with ultraviolet light or non-thermal plasma. *European Journal of Oral Sciences*, Blackwell Munksgaard, v. 126, p. 126–134, 4 2018. ISSN 16000722.

HOLSTEIN, S. A.; CERMAK, D. M.; WIEMER, D. F.; LEWIS, K.; HOHL, R. J. Phosphonate and bisphosphonate analogues of farnesyl pyrophosphate as potential inhibitors of farnesyl protein transferase. *Bioorganic and Medicinal Chemistry*, v. 6, p. 687–694, 1998. ISSN 09680896.

HOQUE, E.; DEROSE, J. A.; HOFFMANN, P.; MATHIEU, H. J.; BHUSHAN, B.; CICHOMSKI, M. Phosphonate self-assembled monolayers on aluminum surfaces. *Journal of Chemical Physics*, v. 124, 2006. ISSN 00219606.

HSU, L. H.; KWAśNIEWSKA, D.; WANG, S. C.; SHEN, T. L.; WIECZOREK, D.; CHEN, Y. L. Gemini quaternary ammonium compound pmt12-bf4 inhibits candida albicans via regulating iron homeostasis. *Scientific Reports*, v. 10, p. 1–12, 2020. ISSN 20452322.

JERDIOUI, S.; ELANSARI, L.; JARADAT, N.; JODEH, S.; AZZAOUI, K.; HAMMOUTI, B.; LAKRAT, M.; TAHANI, A.; JAMA, C.; BENTISS, F. Effects of gallic acid on the nanocrystalline hydroxyapatite formation using the neutralization process. *Journal of Trace Elements and Minerals*, v. 2, p. 100009, 12 2022. ISSN 27730506. Disponível em: <https://linkinghub.elsevier.com/retrieve/pii/S2773050622000088>.

JIAO, Y.; NIU, L. na; MA, S.; LI, J.; TAY, F. R.; CHEN, J. hua. Quaternary ammonium-based biomedical materials: State-of-the-art, toxicological aspects and antimicrobial resistance. *Progress in Polymer Science*, v. 71, p. 53–90, 8 2017. ISSN 00796700. Disponível em: <https://linkinghub.elsevier.com/retrieve/pii/S0079670017300667>.

JOHN, A. A.; JAGANATHAN, S. K.; SUPRIYANTO, E.; MANIKANDAN, A. Surface modification of titanium and its alloys for the enhancement of osseointegration in orthopaedics. *Current Science*, v. 111, p. 1003–1015, 2016. ISSN 00113891.

JOHNSEN, S. P.; SøRENSEN, H. T.; PEDERSEN, A. B.; LUCHT, U.; SøBALLE, K.; OVERGAARD, S. Patient-related predictors of implant failure after primary total hip replacement in the initial, short- and long-term: A nationwide danish folow-up study including 36 984 patients. *Journal of Bone and Joint Surgery - Series B*, v. 88, p. 1303–1308, 2006. ISSN 0301620X.

JOSSE, S.; FAUCHEUX, C.; SOUEIDAN, A.; GRIMANDI, G.; MASSIOT, D.; ALONSO, B.; JANVIER, P.; LAïB, S.; GAUTHIER, O.; DACULSI, G.; GUICHEUX, J.; BUJOLI, B.; BOULER, J. M. Chemically modified calcium phosphates as novel materials for bisphosphonate delivery. *Advanced Materials*, v. 16, p. 1423–1427, 2004. ISSN 09359648.

KARLSSON, J.; ATEFYEKTA, S.; ANDERSSON, M. Controlling drug delivery kinetics from mesoporous titania thin films by pore size and surface energy. *International Journal of Nanomedicine*, v. 10, p. 4425–4436, 2015. ISSN 11782013.

KASHI, A.; SAHA, S. *Failure mechanisms of medical implants and their effects on outcomes*. Elsevier Ltd, 2019. 407-432 p. ISBN 9780081026809. Disponível em: <http://dx.doi.org/10.1016/B978-0-08-102680-9.00015-9>.

KAUR, M.; SINGH, K. Review on titanium and titanium based alloys as biomaterials for orthopaedic applications. *Materials Science Engineering C*, Elsevier, v. 102, p. 844–862, 2019. ISSN 0928-4931. Disponível em: <https://doi.org/10.1016/j.msec.2019.04.064>.

KAUR, R.; LIU, S. Antibacterial surface design – contact kill. *Progress in Surface Science*, Elsevier Ltd, v. 91, p. 136–153, 2016. ISSN 00796816. Disponível em: <http://dx.doi.org/10.1016/j.progsurf.2016.09.001>.

KE, J.; DOU, H.; ZHANG, X.; UHAGAZE, D. S.; DING, X.; DONG, Y. Determination of pka values of alendronate sodium in aqueous solution by piecewise linear regression based on acid-base potentiometric titration. *Journal of Pharmaceutical Analysis*, Elsevier, v. 6, p. 404–409, 2016. ISSN 20951779. Disponível em: <http://dx.doi.org/10.1016/j.jpha.2016.07.001>.

KEPELOVá, A.; NEWBERG, J.; HUTHWELKER, T.; BLUHM, H.; AMMANN, M. The nature of nitrate at the ice surface studied by xps and nexafs. *Physical Chemistry Chemical Physics*, v. 12, p. 8870–8880, 2010. ISSN 14639076.

KHAMIS, A. K.; ELSHARKAWY, S. The influence of local delivery of bisphosphonate oosseointegration of dental implants. *Evidence-Based Dentistry*, v. 19, p. 82–83, 2018. ISSN 14765446.

KHONSARY, S. Guyton and hall: Textbook of medical physiology. *Surgical Neurology International*, p. 1038, 2017. ISSN 2152-7806. Disponível em: <https://www.elsevier.com/books/guyton-and-hall-textbook-of-medical-physiology/hall/978-1-4557-7005-2http://surgicalneurologyint.com/surgicalint-articles/guyton-and-hall-textbook-of-medical-physiology/>.

KIM, H. S.; LEE, J. I.; YANG, S. S.; KIM, B. S.; KIM, B. C.; LEE, J. The effect of alendronate soaking and ultraviolet treatment on bone–implant interface. *Clinical Oral Implants Research*, v. 28, p. 1164–1172, 2017. ISSN 16000501.

KLEIN, P.; KONCHAKOVA, N.; HRISTOVA-BOGAERDS, D. G.; NOESKE, M.; SIMPERLER, A.; GOLDBECK, G.; HöCHE, D. Translation in materials modelling – process and progress 1 . executive summary. p. 1–36.

KOSMULSKI, M. The significance of the difference in the point of zero charge between rutile and anatase. *Advances in Colloid and Interface Science*, v. 99, p. 255–264, 2002. ISSN 00018686.

KRANZ, S.; GUELLMAR, A.; VOELPEL, A.; LESSER, T.; TONNDORF-MARTINI, S.; SCHMIDT, J.; SCHRADER, C.; FAUCON, M.; FINGER, U.; PFISTER, W.; DIEFENBECK, M.; SIGUSCH, B. Bactericidal and biocompatible properties of plasma chemical oxidized titanium (tiob®) with antimicrobial surface functionalization. *Materials*, MDPI AG, v. 16, 3 2019. ISSN 19961944.

KULKA, M. W.; DONSKYI, I. S.; WURZLER, N.; SALZ, D.; ÖZCAN Özlem; UNGER, W. E.; HAAG, R. Mussel-inspired multivalent linear polyglycerol coatings outperform monovalent polyethylene glycol coatings in antifouling surface properties. *ACS Applied Bio Materials*, v. 2, p. 5749–5759, 2019. ISSN 25766422.

LANDOULSI, J.; GENET, M. J.; RICHARD, C.; KIRAT, K. E.; PULVIN, S.; ROUXHET, P. G. Evolution of the passive film and organic constituents at the surface of stainless steel immersed in fresh water. *Journal of Colloid and Interface Science*, v. 318, p. 278–289, 2008. ISSN 00219797.

LASCANE, L. G.; OLIVEIRA, E. F.; BATAGIN-NETO, A. Polyfuran-based chemical sensors: reactivity analysis via fukui indexes and reactive molecular dynamics. *MRS Advances*, v. 5, p. 497–503, 4 2020. ISSN 2059-8521. Disponível em: <https://www.cambridge.org/core/product/identifier/S2059852120002030/type/journal_article>.

LEE, C.; YANG, W.; PARR, R. G. Development of the colle-salvetti correlation-energy formula into a functional of the electron density. *Physical Review B*, v. 37, p. 785–789, 1 1988. ISSN 0163-1829. Disponível em: <https://link.aps.org/doi/10.1103/PhysRevB.37.785>.

LI, J.; CUI, X.; HOOPER, G. J.; LIM, K. S.; WOODFIELD, T. B. F. Journal of the mechanical behavior of biomedical materials rational design , bio-functionalization and biological performance of hybrid additive manufactured titanium implants for orthopaedic applications : A review. *Journal of the Mechanical Behavior of Biomedical Materials*, Elsevier Ltd, v. 105, p. 103671, 2020. ISSN 1751-6161. Disponível em: <https://doi.org/10.1016/j.jmbbm.2020.103671>.

LI, N.; SONG, J.; ZHU, G.; SHI, X.; WANG, Y. Alendronate conjugated nanoparticles for calcification targeting. *Colloids and Surfaces B: Biointerfaces*, Elsevier B.V., v. 142, p. 344–350, 2016. ISSN 18734367. Disponível em: <http://dx.doi.org/10.1016/j.colsurfb.2016.03.015>.

LIN, T. J. Predicting binding affinities of nitrogen-containing bisphosphonates on hydroxyapatite surface by molecular dynamics. *Chemical Physics Letters*, Elsevier, v. 716, p. 83–92, 2019. ISSN 00092614. Disponível em: <https://doi.org/10.1016/j.cplett.2018.12.008>.

LIU, J.; DU, C.; BEAMAN, H. T.; MONROE, M. B. B. Characterization of phenolic acid antimicrobial and antioxidant structure–property relationships. *Pharmaceutics*, v. 12, p. 419, 5 2020. ISSN 1999-4923. Disponível em: <https://www.mdpi.com/1999-4923/12/5/419>.

LIU, Z.; TABORA, J.; DAVIS, R. J. *Relationships between microstructure and surface acidity of Ti-Si mixed oxide catalysts*. 1994. 117-126 p.

LUSCHTINETZ, R.; OLIVEIRA, A. F.; DUARTE, H. A.; SEIFERT, G. Self-assembled monolayers of alkylphosphonic acids on aluminum oxide surfaces - a theoretical study. *Zeitschrift fur Anorganische und Allgemeine Chemie*, v. 636, p. 1506–1512, 2010. ISSN 00442313.

LUTTRELL, T.; HALPEGAMAGE, S.; TAO, J.; KRAMER, A.; SUTTER, E.; BATZILL, M. Why is anatase a better photocatalyst than rutile?-model studies on epitaxial tio2 films. *Scientific reports*, Nature Publishing Group, v. 4, n. 1, p. 1–8, 2014.

LóPEZ-HUERTA, F.; CERVANTES, B.; GONZáLEZ, O.; HERNáNDEZ-TORRES, J.; GARCíA-GONZáLEZ, L.; VEGA, R.; HERRERA-MAY, A. L.; SOTO, E. Biocompatibility and surface properties of tio2 thin films deposited by dc magnetron sputtering. *Materials*, MDPI AG, v. 7, p. 4105–4117, 2014. ISSN 19961944.

MAFFULLI, N.; VIA, A. G. *General Orthopaedics and Basic Science*. [s.n.], 2019. 37-49 p. ISSN 2520-1123. ISBN 978-3-319-92191-4. Disponível em: <http://link.springer.com/10.1007/978-3-319-92193-8>.

MAIA, R. A.; VENTORIM, G.; BATAGIN-NETO, A. Reactivity of lignin subunits: the influence of dehydrogenation and formation of dimeric structures. *Journal of Molecular Modeling*, Journal of Molecular Modeling, v. 25, 2019. ISSN 09485023.

MALAVASI, M.; LOURO, R.; BARROS, M. B.; TEIXEIRA, L. N.; PERUZZO, D. C.; JOLY, J. C.; MARTINEZ, E. F.; NAPIMOGA, M. H. *Effects of risedronate on osteoblastic cell cultures*. 2016. 43-47 p.

MANDú, L. O.; BATAGIN-NETO, A. Chemical sensors based on n-substituted polyaniline derivatives: reactivity and adsorption studies via electronic structure calculations. *Journal of Molecular Modeling*, v. 24, 2018. ISSN 09485023.

MANGOLINI, F.; MCCLIMON, J. B.; ROSE, F.; CARPICK, R. W. Accounting for nanometer-thick adventitious carbon contamination in x-ray absorption spectra of carbon-based materials. *Analytical Chemistry*, v. 86, p. 12258–12265, 2014. ISSN 15206882.

MAZóN, P.; GARCíA-BERNAL, D.; MESEGUER-OLMO, L.; CRAGNOLINI, F.; AZA, P. N. D. Human mesenchymal stem cell viability, proliferation and differentiation potential in response to ceramic chemistry and surface roughness. *Ceramics International*, Elsevier Ltd, v. 41, p. 6631–6644, 6 2015. ISSN 02728842.

MCINTYRE, N. S.; NIE, H. Y.; GROSVENOR, A. P.; DAVIDSON, R. D.; BRIGGS, D. Xps studies of octadecylphosphonic acid (opa) monolayer interactions with some metal and mineral surfaces. *Surface and Interface Analysis*, v. 37, p. 749–754, 2005. ISSN 01422421.

MELIN, J.; APARICIO, F.; SUBRAMANIAN, V.; GALVáN, M.; CHATTARAJ, P. K. Is the fukui function a right descriptor of hard-hard interactions? *Journal of Physical Chemistry A*, v. 108, p. 2487–2491, 2004. ISSN 10895639.

MENEZES, A. M.; ROCHA, F. A. C.; CHAVES, H. V.; CARVALHO, C. B.; RIBEIRO, R. A.; BRITO, G. A. C. Effect of sodium alendronate on alveolar bone resorption in experimental periodontitis in rats. *Journal of Periodontology*, Wiley, v. 76, p. 1901–1909, 11 2005. ISSN 0022-3492.

MENG, J.; ZHANG, X.; NI, L.; TANG, Z.; ZHANG, Y.; ZHANG, Y.; ZHANG, W. Antibacterial cellulose membrane via one-step covalent immobilization of ammonium/amine groups. *Desalination*, Elsevier B.V., v. 359, p. 156–166, 2015. ISSN 00119164. Disponível em: <http://dx.doi.org/10.1016/j.desal.2014.12.032>.

MESCHER, A. L. *Junqueira's Basic Histology: Text and Atlas*. Fifteenth. [s.n.], 2018. 186 p. ISBN 978-1-26-002618-4. Disponível em: <https://accessmedicine.mhmedical.com/book.aspx?bookID=2430>.

MILELLA, E.; COSENTINO, F.; LICCIULLI, A.; MASSARO, C. Preparation and characterisation of titania/hydroxyapatite composite coatings obtained by sol-gel process. *Biomaterials*, v. 22, p. 1425–1431, 2001. ISSN 01429612.

MILOšEV, I.; METIKOš-HUKOVIć, M.; PETROVIć Željka. Influence of preparation methods on the properties of self-assembled films of octadecylphosphonate on nitinol: Xps and eis studies. *Materials Science and Engineering C*, v. 32, p. 2604–2616, 2012. ISSN 09284931.

MOULDER, J. F. W. F. S. P. E. B. K. D. *Handbook of X-ray Photoelectron Spectroscopy*. [S.l.: s.n.], 1993. ISBN 9780962702624.

MYRSETH, V.; BOZEK, J. D.; KUKK, E.; SATHRE, L. J.; THOMAS, T. D. Adiabatic and vertical carbon 1s ionization energies in representative small molecules. *Journal of Electron Spectroscopy and Related Phenomena*, v. 122, p. 57–63, 2002. ISSN 03682048.

NANCOLLAS, G. H.; TANG, R.; PHIPPS, R. J.; HENNEMAN, Z.; GULDE, S.; WU, W.; MANGOOD, A.; RUSSELL, R. G.; EBETINO, F. H. Novel insights into actions of bisphosphonates on bone: Differences in interactions with hydroxyapatite. *Bone*, v. 38, p. 617–627, 2006. ISSN 87563282.

NEU, T. R. Significance of bacterial surface-active compounds in interaction of bacteria with interfaces. *Microbiological Reviews*, v. 60, p. 151–166, 1996. ISSN 01460749.

NICHOLSON, J. W. Titanium alloys for dental implants : A review. p. 100–116, 2020.

OOSTERHOF, J. J.; BUIJSSEN, K. J.; BUSSCHER, H. J.; LAAN, B. F. V. D.; MEI, H. C. V. D. Effects of quaternary ammonium silane coatings on mixed fungal and bacterial biofilms on tracheoesophageal shunt prostheses. *Applied and Environmental Microbiology*, v. 72, p. 3673–3677, 2006. ISSN 00992240.

OTHMANI, M.; AISSA, A.; BAC, C. G.; RACHDI, F.; DEBBABI, M. Surface modification of calcium hydroxyapatite by grafting of etidronic acid. *Applied Surface Science*, Elsevier B.V., v. 274, p. 151–157, 2013. ISSN 01694332.

OUEINY, C.; BERLIOZ, S.; PATOUT, L.; PERRIN, F. X. Aqueous dispersion of multiwall carbon nanotubes with phosphonic acid derivatives. *Colloids and Surfaces A: Physicochemical and Engineering Aspects*, Elsevier B.V., v. 493, p. 41–51, 2016. ISSN 18734359. Disponível em: <http://dx.doi.org/10.1016/j.colsurfa.2016.01.028>.

OWENS, G. J.; SINGH, R. K.; FOROUTAN, F.; ALQAYSI, M.; HAN, C. min; MAHAPATRA, C.; KIM, H. won. Progress in materials science sol – gel based materials for biomedical applications. v. 77, p. 1–79, 2016.

PALAZZO, B.; IAFISCO, M.; LAFORGIA, M.; MARGIOTTA, N.; NATILE, G.; BIANCHI, C. L.; WALSH, D.; MANN, S.; ROVERI, N. Biomimetic hydroxyapatite-drug nanocrystals as potential bone substitutes with antitumor drug delivery properties. *Advanced Functional Materials*, v. 17, p. 2180–2188, 9 2007. ISSN 1616301X.

PARFITT, A. M. Misconceptions (2): Turnover is always higher in cancellous than in cortical bone. *Bone*, v. 30, p. 807–809, 2002. ISSN 87563282.

PARK, C. G.; PARK, M.; KIM, B. H.; LEE, S. H.; PARK, J. Y.; PARK, H. H.; LEE, K.; SEOK, H. K.; CHOY, Y. B. Pattern-coated titanium bone fixation plate for dual delivery of vancomycin and alendronate. *Macromolecular Research*, Polymer Society of Korea, v. 25, p. 756–762, 7 2017. ISSN 20927673.

PETER, B.; PIOLETTI, D. P.; LAïB, S.; BUJOLI, B.; PILET, P.; JANVIER, P.; GUICHEUX, J.; ZAMBELLI, P. Y.; BOULER, J. M.; GAUTHIER, O. Calcium phosphate drug delivery system: Influence of local zoledronate release on bone implant osteointegration. *Bone*, v. 36, p. 52–60, 2005. ISSN 87563282.

PETROVIć Željka; ŠARIć, A.; DESPOTOVIć, I.; KATIć, J.; PETER, R.; PETRAVIć, M.; PETKOVIć, M. A new insight into coating's formation mechanism between tio2 and alendronate on titanium dental implant. *Materials*, v. 13, 2020. ISSN 19961944.

PLETINCX, S.; FOCKAERT, L. L. I.; MOL, J. M. C.; HAUFFMAN, T.; TERRYN, H. Probing the formation and degradation of chemical interactions from model molecule/metal oxide to buried polymer/metal oxide interfaces. *npj Materials Degradation*, Springer US, v. 3, p. 1–12, 2019. ISSN 2397-2106. Disponível em: <http://dx.doi.org/10.1038/s41529-019-0085-2>.

PLáCIDO, A.; BUENO, J.; BARBOSA, E. A.; MOREIRA, D. C.; DIAS, N.; CABRAL, W. F.; BESSA, L. J.; BRAND, G. D.; RELVAS, B.; LEITE, R. S. A.; EATON, P. The antioxidant peptide salamandrin-i : First bioactive peptide identified from skin secretion of salamandra genus (salamandra salamandra). *Biomolecules*, v. 10, p. 512, 2020.

PROFT, F. D.; ALSENOY, C. V.; PEETERS, A.; LANGENAEKER, W.; GEERLINGS, P. Atomic charges, dipole moments, and fukui functions using the hirshfeld partitioning of the electron density. *Journal of Computational Chemistry*, v. 23, p. 1198–1209, 2002. ISSN 01928651.

QUIñONES, R.; GARRETSON, S.; BEHNKE, G.; FAGAN, J. W.; MUELLER, K. T.; AGARWAL, S.; GUPTA, R. K. Fabrication of phosphonic acid films on nitinol nanoparticles by dynamic covalent assembly. *Thin Solid Films*, Elsevier, v. 642, p. 195–206, 2017. ISSN 00406090. Disponível em: <http://dx.doi.org/10.1016/j.tsf.2017.09.048>.

QUéRé, D. Wetting and roughness. *Annual Review of Materials Research*, Annual Reviews Inc., v. 38, p. 71–99, 2008. ISSN 15317331.

RAFIEE, K.; NAFFAKH-MOOSAVY, H.; TAMJID, E. The effect of laser frequency on roughness, microstructure, cell viability and attachment of ti6al4v alloy. *Materials Science and Engineering C*, Elsevier Ltd, v. 109, 4 2020. ISSN 18730191.

RAMIRES, P. A.; ROMITO, A.; COSENTINO, F.; MILELLA, E. The influence of titania/hydroxyapatite composite coatings on in vitro osteoblasts behaviour. *Biomaterials*, v. 22, p. 1467–1474, 2001. ISSN 01429612.

RATNER, B. D.; CASTNER, D. G. *Surface Properties and Surface Characterization of Biomaterials*. Fourth edi. Elsevier, 2020. 53-75 p. Disponível em: <http://dx.doi.org/10.1016/B978-0-12-816137-1.00006-4>.

REN, J.; LI, Z.; LIU, S.; XING, Y.; XIE, K. Silica-titania mixed oxides: Si-o-ti connectivity, coordination of titanium, and surface acidic properties. *Catalysis Letters*, v. 124, p. 185–194, 2008. ISSN 1011372X.

RESHAMWALA, S. M.; MAMIDIPALLY, C.; PISSURLENKAR, R. R.; COUTINHO, E. C.; NORONHA, S. B. Evaluation of risedronate as an antibiofilm agent. *Journal of Medical Microbiology*, Microbiology Society, v. 65, p. 9–18, 1 2016. ISSN 00222615.

RI, M. H.; JANG, Y. M.; RI, U. S.; YU, C. J.; KIM, K. I.; KIM, S. U. Ab initio investigation of adsorption characteristics of bisphosphonates on hydroxyapatite (001) surface. *Journal of Materials Science*, Springer US, v. 53, p. 4252–4261, 2018. ISSN 15734803. Disponível em: <https://doi.org/10.1007/s10853-017-1880-1>.

ROGERS, M. J.; MöNKKöNEN, J.; MUNOZ, M. A. Molecular mechanisms of action of bisphosphonates and new insights into their effects outside the skeleton. *Bone*, Elsevier, v. 139, p. 115493, 2020. ISSN 87563282. Disponível em: <https://doi.org/10.1016/j.bone.2020.115493>.

ROJO, L.; GHARIBI, B.; MCLISTER, R.; MEENAN, B. J.; DEB, S. Self-assembled monolayers of alendronate on ti6al4v alloy surfaces enhance osteogenesis in mesenchymal stem cells. *Scientific Reports*, Nature Publishing Group, v. 6, p. 1–10, 2016. ISSN 20452322. Disponível em: <http://dx.doi.org/10.1038/srep30548>.

ROMANOS, N.; KALOGERINI, M.; KOUMOULOS, E. P.; MOROZINIS, A. K.; SEBASTIANI, M.; CHARITIDIS, C. Innovative data management in advanced characterization: Implications for materials design. *Materials Today Communications*, Elsevier, v. 20, 2019. ISSN 23524928.

ROY, R. K.; HIRAO, K.; PAL, S. On non-negativity of fukui function indices. ii. *Journal of Chemical Physics*, v. 113, p. 1372–1379, 2000. ISSN 00219606.

RUSSELL, R. G.; CROUCHER, P. I.; ROGERS, M. J. Bisphosphonates: pharmacology, mechanisms of action and clinical uses. *Osteoporosis International*, v. 9, p. 66–80, 1999. ISSN 0937941X.

RUSSELL, R. G.; WATTS, N. B.; EBETINO, F. H.; ROGERS, M. J. Mechanisms of action of bisphosphonates: similarities and differences and their potential influence on clinical efficacy. *Osteoporosis International*, v. 19, p. 733–759, 2008. ISSN 0937941X.

SADER, J. E.; BORGANI, R.; GIBSON, C. T.; HAVILAND, D. B.; HIGGINS, M. J.; KILPATRICK, J. I.; LU, J.; MULVANEY, P.; SHEARER, C. J.; SLATTERY, A. D.; THORéN, P. A.; TRAN, J.; ZHANG, H.; ZHANG, H.; ZHENG, T. A virtual instrument to standardise the calibration of atomic force microscope cantilevers. *Review of Scientific Instruments*, v. 87, 2016. ISSN 10897623. Disponível em: <10.1063/1.4962866>.

SALON, M. C. B.; BAYLE, P. A.; ABDELMOULEH, M.; BOUFI, S.; BELGACEM, M. N. Kinetics of hydrolysis and self condensation reactions of silanes by nmr spectroscopy. *Colloids and Surfaces A: Physicochemical and Engineering Aspects*, v. 312, p. 83–91, 2008. ISSN 09277757.

SALON, M. C. B.; BELGACEM, M. N. Hydrolysis-condensation kinetics of different silane coupling agents. *Phosphorus, Sulfur and Silicon and the Related Elements*, v. 186, p. 240–254, 2011. ISSN 10426507.

SANTOS, F. C. D.; HARB, S. V.; MENU, M. J.; TURQ, V.; PULCINELLI, S. H.; SANTILLI, C. V.; HAMMER, P. On the structure of high performance anticorrosive pmma-siloxane-silica hybrid coatings. *RSC Advances*, v. 5, p. 106754–106763, 2015. ISSN 20462069.

SHIMOJIMA, A.; SUGAHARA, Y.; KURODA, K. Inorganic – organic layered materials derived via the hydrolysis and polycondensation of trialkoxy(alkyl)silanes. *Bulletin of the Chemical Society of Japan*, v. 70, p. 2847–2853, 11 1997. ISSN 0009-2673. Disponível em: <http://www.journal.csj.jp/doi/10.1246/bcsj.70.2847>.

SIDAMBE, A. T. Biocompatibility of advanced manufactured titanium implants—a review. p. 8168–8188, 2014.

SIDANE, D.; RAMMAL, H.; BELJEBBAR, A.; GANGLOFF, S. C.; CHICOT, D.; VELARD, F.; KHIREDDINE, H.; MONTAGNE, A.; KERDJOUDJ, H. *Biocompatibility of sol-gel hydroxyapatite-titania composite and bilayer coatings*. 2017. 650-658 p.

SPATZ, J. P.; MöLLER, M.; NOESKE, M.; BEHM, R. J.; PIETRALLA, M. Nanomosaic surfaces by lateral phase separation of a diblock copolymer. *Macromolecules*, v. 30, p. 3874–3880, 1997. ISSN 00249297.

SRIPRANG, P.; WONGNAWA, S.; SIRICHOTE, O. Amorphous titanium dioxide as an adsorbent for dye polluted water and its recyclability. *Journal of Sol-Gel Science and Technology*, v. 71, p. 86–95, 2014. ISSN 09280707.

STAPELFELDT, K.; STAMBOROSKI, S.; WALTER, I.; SUTER, N.; KOWALIK, T.; MICHAELIS, M.; BRüGGEMANN, D. Controlling the multiscale structure of nanofibrous fibrinogen scaffolds for wound healing. *Nano Letters*, v. 19, p. 6554–6563, 2019. ISSN 15306992.

STEPHEN, P. J.; DEVLIN, F. J.; CHABALOWSKI, C. F.; FRISCH, M. J. Ab initio calculation of vibrational absorption. *The Journal of Physical Chemistry*, v. 98, p. 11623–11627, 1994.

SUTTIPONPARNIT, K.; JIANG, J.; SAHU, M.; SUVACHITTANONT, S.; CHARINPANITKUL, T.; BISWAS, P. Role of surface area, primary particle size, and crystal phase on titanium dioxide nanoparticle dispersion properties. *Nanoscale Research Letters*, v. 6, p. 1–8, 2011. ISSN 1556276X.

TAHA, E. A.; YOUSSEF, N. F. Spectrophotometric determination of some drugs for osteoporosis. *Chemical and Pharmaceutical Bulletin*, v. 51, p. 1444–1447, 2003. ISSN 00092363.

TANG, R.; ZHANG, Y.; ZHANG, Y.; YU, Z. Synthesis and characterization of chitosan based dye containing quaternary ammonium group. *Carbohydrate Polymers*, Elsevier Ltd., v. 139, p. 191–196, 2016. ISSN 01448617. Disponível em: <http://dx.doi.org/10.1016/j.carbpol.2015.12.047>.

THEILE-RASCHE, C.; WIESING, M.; SCHWIDEREK, S.; NOESKE, M.; GRUNDMEIER, G. How self-assembled organophosphonic acid monolayers on ti0.5al0.5n hard coatings affect the adsorption of polycarbonate melt. *Applied Surface Science*, Elsevier, v. 513, p. 145701, 2020. ISSN 01694332. Disponível em: <https://doi.org/10.1016/j.apsusc.2020.145701>.

TOMASI, J.; MENNUCCI, B.; CAMMI, R. Quantum mechanical continuum solvation models. *Chemical Reviews*, v. 105, p. 2999–3093, 2005. ISSN 00092665.

TORKELSON, A. A.; SILVA, A. K. da; LOVE, D. C.; KIM, J. Y.; ALPER, J. P.; COOX, B.; DAHM, J.; KOZODOY, P.; MABOUDIAN, R.; NELSON, K. L. Investigation of quaternary ammonium silane-coated sand filter for the removal of bacteria and viruses from drinking water. *Journal of Applied Microbiology*, v. 113, p. 1196–1207, 2012. ISSN 13645072.

TORNOW, C.; NOESKE, P. L.; DIECKHOFF, S.; WILKEN, R.; GäRTNER, K. Preparation and characterization of carbonate terminated polycrystalline al 2 o 3 /al films. *Applied Surface Science*, v. 252, p. 1959–1965, 2005. ISSN 01694332.

TORUN, B.; GINER, I.; GRUNDMEIER, G.; OZCAN, O. In situ pm-irras studies of organothiols and organosilane monolayers–zno interfaces at high water activities. *Surface and Interface Analysis*, v. 49, p. 71–74, 2017. ISSN 10969918.

TRINO, L. D.; BRONZE-UHLE, E. S.; GEORGE, A.; MATHEW, M. T.; LISBOA-FILHO, P. N. *Surface physicochemical and structural analysis of functionalized titanium dioxide films*. 2018. 168-178 p.

TRINO, L. D.; DIAS, L. F.; ALBANO, L. G.; BRONZE-UHLE, E. S.; RANGEL, E. C.; GRAEFF, C. F.; LISBOA-FILHO, P. N. Zinc oxide surface functionalization and related effects on corrosion resistance of titanium implants. *Ceramics International*, v. 44, p. 4000–4008, 2018. ISSN 02728842.

UREñA, Y. R. C.; WITTIG, L.; NASCIMENTO, M. V.; FACCIONI, J. L.; FILHO, P. N. L.; RISCHKA, K. Influences of the ph on the adsorption properties of an antimicrobial peptide on titanium surfaces. *Applied Adhesion Science*, v. 3, 2015. ISSN 21964351.

VIDYASAGAR, L.; APSE, P. Dental implant design and biological effects on bone-implant interface. *Baltic Dental and Maxillofacial Journal*, v. 6, p. 51–54, 2004.

VILLARRUBIA, J. S. Morphological estimation of tip geometry for scanned probe microscopy. *Surface Science*, v. 321, p. 287–300, 1994. ISSN 00396028.

WANG, Q.; ZHOU, P.; LIU, S.; ATTARILAR, S.; MA, R. L. W.; ZHONG, Y.; WANG, L. Multi-scale surface treatments of titanium implants for rapid osseointegration: A review. *Nanomaterials*, v. 10, p. 1–27, 2020. ISSN 20794991.

WANG, X.; LI, B.; ZHOU, L.; MA, J.; ZHANG, X.; LI, H.; LIANG, C.; LIU, S.; WANG, H. Influence of surface structures on biocompatibility of tio2/ha coatings prepared by mao. *Materials Chemistry and Physics*, v. 215, p. 339–345, 2018. ISSN 02540584.

WEI, Q.; BECHERER, T.; ANGIOLETTI-UBERTI, S.; DZUBIELLA, J.; WISCHKE, C.; NEFFE, A. T.; LENDLEIN, A.; BALLAUFF, M.; HAAG, R. Protein interactions with polymer coatings and biomaterials. *Angewandte Chemie - International Edition*, v. 53, p. 8004–8031, 2014. ISSN 15213773.

XU, X.; WANG, N.; WU, M.; WANG, J.; WANG, D.; CHEN, Z.; XIE, J.; DING, C.; LI, J. Programmed antibacterial and mineralization therapy for dental caries based on zinc-substituted hydroxyapatite/ alendronate-grafted polyacrylic acid hybrid material. *Colloids and Surfaces B: Biointerfaces*, Elsevier B.V., v. 194, 10 2020. ISSN 18734367.

YANG, W.; MORTIER, W. J. The use of global and local molecular parameters for the analysis of the gas-phase basicity of amines. *Journal of the American Chemical Society*, v. 108, p. 5708–5711, 1986. ISSN 15205126.

YANG, W.; PARR, R. G. Hardness, softness, and the fukui function in the electronic theory of metals and catalysis. *Proceedings of the National Academy of Sciences of the United States of America*, v. 82, p. 6723–6726, 1985. ISSN 00278424.

YANG, Z.; SAEKI, D.; TAKAGI, R.; MATSUYAMA, H. Improved anti-biofouling performance of polyamide reverse osmosis membranes modified with a polyampholyte with effective carboxyl anion and quaternary ammonium cation ratio. *Journal of Membrane Science*, Elsevier B.V., v. 595, p. 117529, 2020. ISSN 18733123. Disponível em: <https://doi.org/10.1016/j.memsci.2019.117529>.

YOSHINARI, M.; MATSUZAKA, K.; INOUE, T.; ODA, Y.; SHIMONO, M. Bio-functionalization of titanium surfaces for dental implants. *Materials Transactions*, v. 43, p. 2494–2501, 2002. ISSN 1345-9678. Disponível em: <https://www.jstage.jst.go.jp/article/matertrans/43/10/43_10_2494/_article>.

YOSHINARI, M.; ODA, Y.; UEKI, H.; YOKOSE, S. Immobilization of bisphosphonates on surface modified titanium. *Biomaterials*, v. 22, p. 709–715, 2001. ISSN 01429612.

ZAREIDOOST, A.; YOUSEFPOUR, M.; GHASEMI, B.; AMANZADEH, A. The relationship of surface roughness and cell response of chemical surface modification of titanium. *Journal of Materials Science: Materials in Medicine*, Kluwer Academic Publishers, v. 23, p. 1479–1488, 6 2012. ISSN 15734838.

ZARRIN, H.; FU, J.; JIANG, G.; YOO, S.; LENOS, J.; FOWLER, M.; CHEN, Z. Quaternized graphene oxide nanocomposites as fast hydroxide conductors. *ACS Nano*, v. 9, p. 2028–2037, 2015. ISSN 1936086X.

ZHAI, Y.; ZHANG, X.; WU, Z.; WANG, Z. Modification of polyvinylidene fluoride membrane by quaternary ammonium compounds loaded on silica nanopollens for mitigating biofouling. *Journal of Membrane Science*, Elsevier B.V., v. 597, p. 117679, 2020. ISSN 18733123. Disponível em: <https://doi.org/10.1016/j.memsci.2019.117679>.

ZHANG, H.; BANFIELD, J. F. Structural characteristics and mechanical and thermodynamic properties of nanocrystalline tio2. *Chemical reviews*, ACS Publications, v. 114, n. 19, p. 9613–9644, 2014.

ZHANG, K.; ZHU, Y.; LIU, X.; CUI, Z.; XIANJIN, Y.; YEUNG, K. W.; PAN, H.; WU, S. Sr/zno doped titania nanotube array: An effective surface system with excellent osteoinductivity and self-antibacterial activity. *Materials and Design*, Elsevier, v. 130, p. 403–412, 2017. ISSN 18734197. Disponível em: <http://dx.doi.org/10.1016/j.matdes.2017.05.085>.

ZHANG, X.; WANG, L.; LEVäNEN, E. Superhydrophobic surfaces for the reduction of bacterial adhesion. *RSC Advances*, v. 3, p. 12003–12020, 2013. ISSN 20462069.

ZHENG, D.; NEOH, K. G.; KANG, E. T. Immobilization of alendronate on titanium via its different functional groups and the subsequent effects on cell functions. *Journal of Colloid and Interface Science*, Elsevier Inc., v. 487, p. 1–11, 2017. ISSN 10957103.

ZOULALIAN, V.; ZüRCHER, S.; TOSATTI, S.; TEXTOR, M.; MONGE, S.; ROBIN, J. J. Self-assembly of poly (ethylene glycol)-poly (alkyl phosphonate) terpolymers on titanium oxide surfaces: synthesis, interface characterization, investigation of nonfouling properties, and long-term stability. *Langmuir*, v. 26, p. 74–82, 2010. ISSN 07437463.

ŠTULAR, D.; VASILJEVIć, J.; ČOLOVIć, M.; MIHELčIč, M.; MEDVED, J.; KOVAč, J.; JERMAN, I.; SIMONčIč, B.; TOMšIč, B. Combining polynipaam/chitosan microgel and bio-barrier polysiloxane matrix to create smart cotton fabric with responsive moisture management and antibacterial properties: influence of the application process. *Journal of Sol-Gel Science and Technology*, v. 83, p. 19–34, 2017. ISSN 15734846.

Appendix

APPENDIX A – *Supplementary information Chapter 3*

For the investigated bulk DMOAP samples, the O 1s spectrum was fitted considering only one contribution, since there is only one oxygen neighbourhood based on DMOAP structure and inspection of the Si 2p region did not reveal signal contributions from the silicon wafer used as a substrate. The detected single peak centered at 532.6 eV is attributed to ester bonds (BEAMSON, 1993; SANTOS et al., 2015). The N 1s signal presented two peaks centered at 402.4 eV and 406.4 eV, attributed to quaternary ammonium cation and to species containing nitrogen-oxygen bonds, moreover, the DMOAP exposed to water did not show the N*-O contribution in the N 1s spectrum, but only the $–N^{+}$ contribution at 402.3 eV (KEPELOVá et al., 2010; ZHANG et al., 2017). As compared to the stoichiometrically expected [O]/[N] concentration ratio of 3.0, for vacuum-dried DMOAP a value of 3.1 was found. The Si 2p signal presented only a centrosymmetric peak at 102.4 eV attributed to alkyltrialkoxysilyl moieties, with the expected binding energy (DIETRICH et al., 2016; ZARRIN et al., 2015). The Cl 2p high resolution spectrum shows only the doublet and the binding energy is coherent with chloride present on DMOAP structure (MOULDER, 1993). In contrast, for the air-dried blot DMOAP a contribution of organic chlorine was detected and attributed to 3-chloropropyl)trimethoxysilane (MOULDER, 1993) (see Figure 33).

Figure 32 – High-resolution spectra a) Si 2p and b) P 2p for investigated bulk ODPA on a silicon wafer

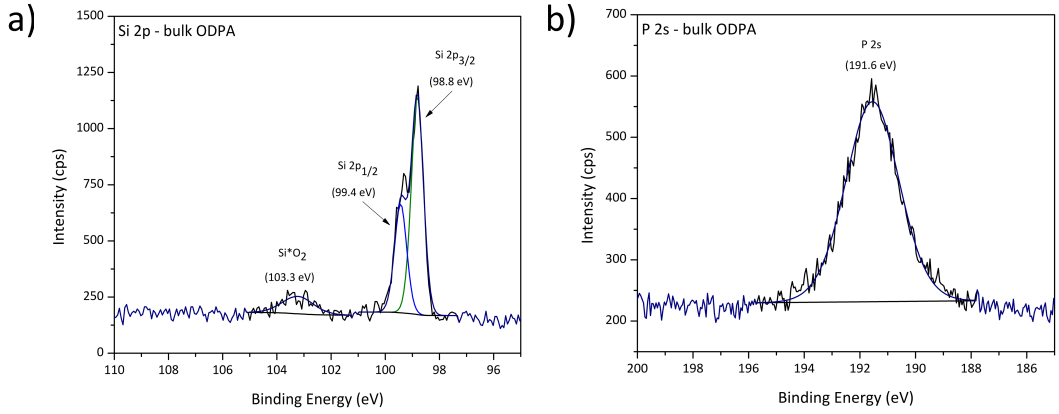

Source: Developed by the author

Figure 33 – O 1s, N 1s, Si 2p and Cl 2p high-resolution spectra for the investigated bulk DMOAP samples

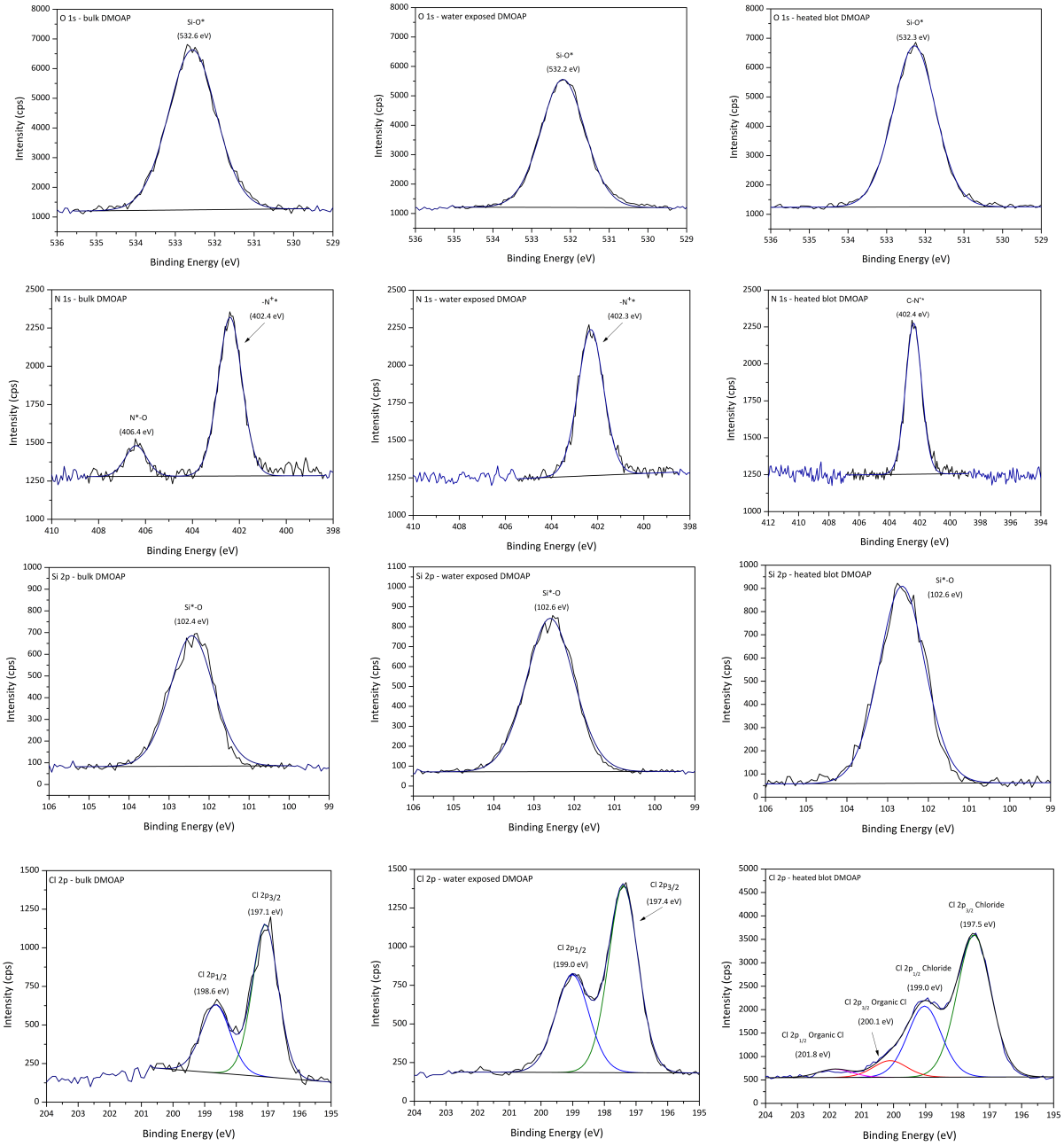

Source: Developed by the author

Figure 34 – C1s and O1s high-resolution spectra for octadecylphosphonic acid adsorbed on titanium dioxide.

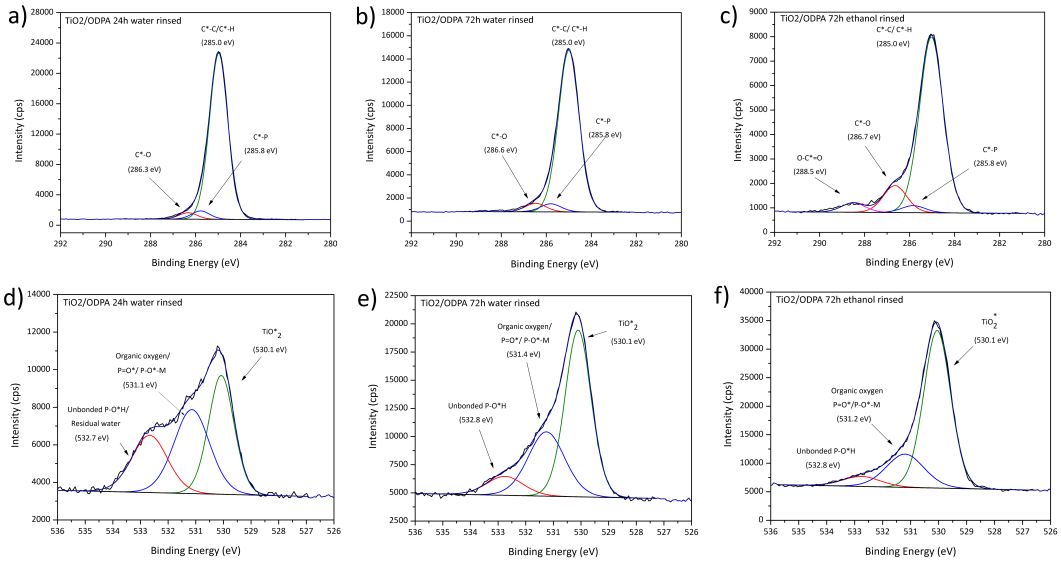

Source: Developed by the author

Figure 35 – P2p high-resolution spectra for octadecylphosphonic acid adsorbed on titanium dioxide.

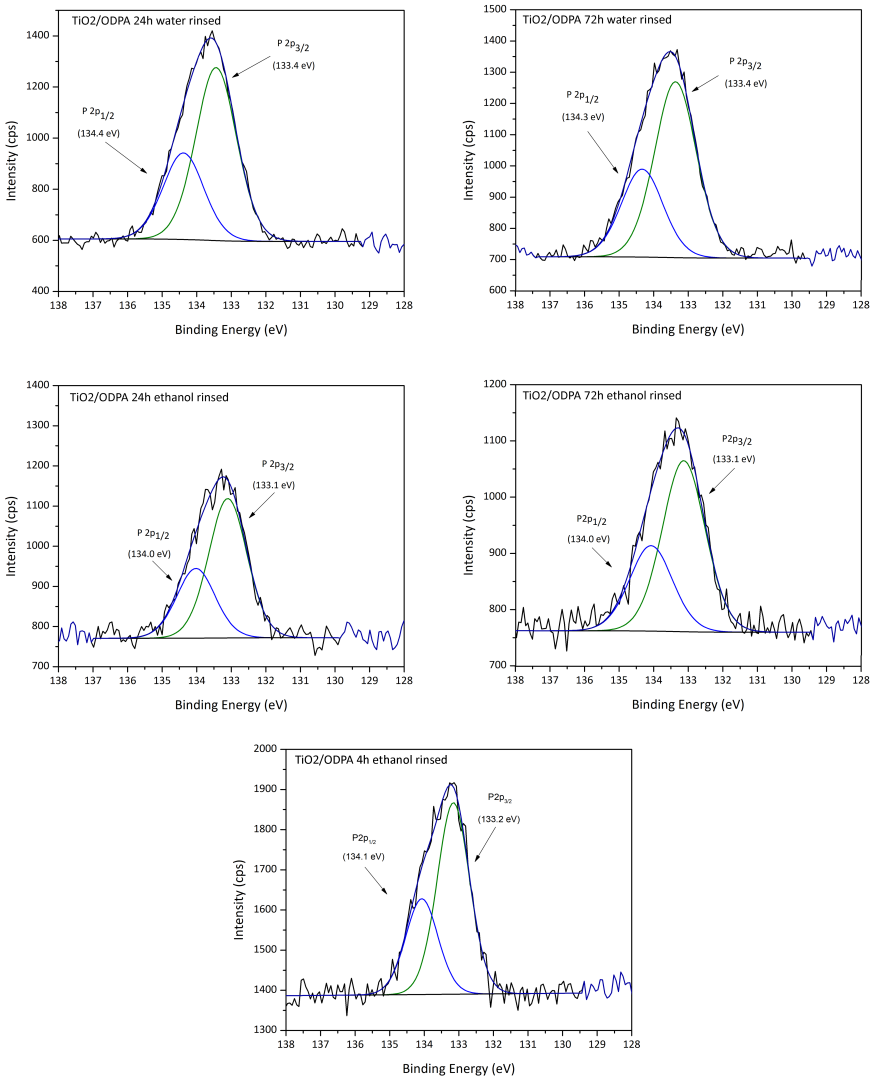

Source: Developed by the author

Figure 36 – Si 2p high-resolution spectra for DMOAP adsorbed on titania. Where "A" represent addition of aqueous HCl on the solution and "N" is the solution without the addition of HCl.

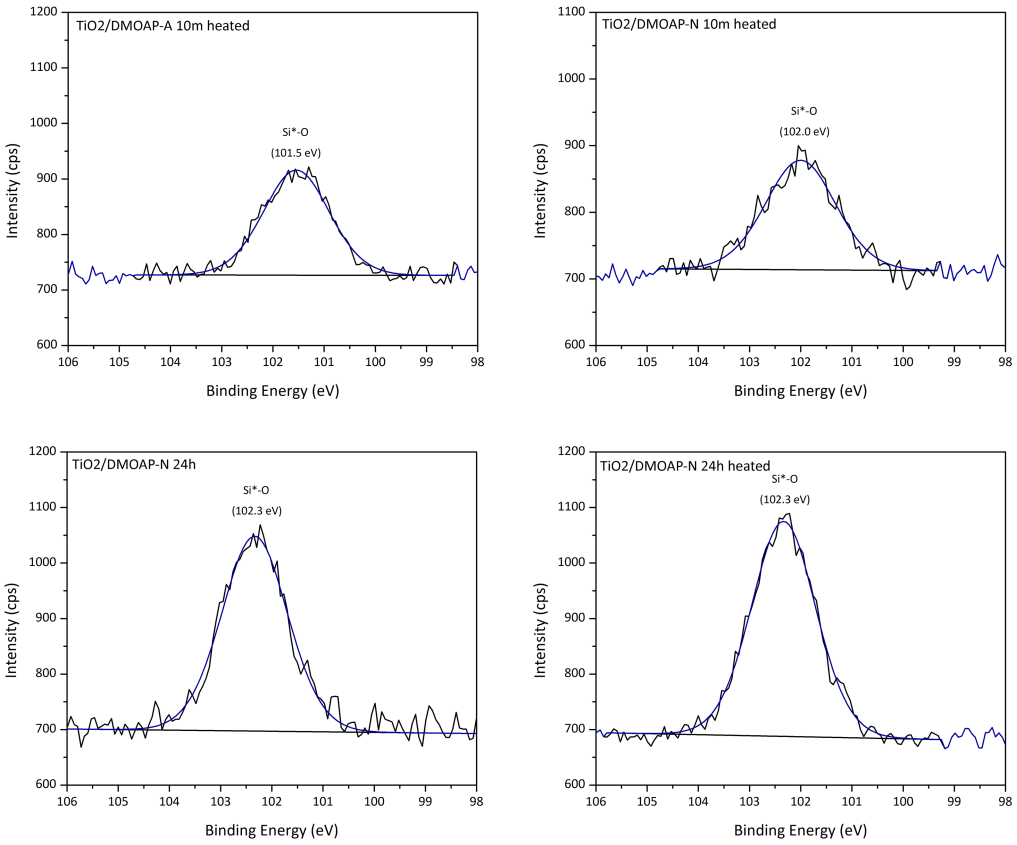

Source: Developed by the author

APPENDIX B – *Supplementary information Chapter 4*

B.1 Materials and Methods

B.1.1 Materials

Silicon wafers from Si-Mat (diameter of 100 mm) were used as substrates along with glass slides from Thermo Scientific® (75 x 25 mm). For titanium dioxide sputter-deposition, a metallic titanium target was employed. Three bisphosphonates were used as adsorptive. Disodium etidronate hydrate (CAS 7414-83-7) and alendronate sodium trihydrate (CAS 121268-17-5) were acquired from TCI® Germany. Risedronate sodium HPLC quality (CAS 115436-72-1) was bought from SIGMA-ALDRICH®. All adsorptives were obtained as powders and used without any further purification. Henceforth, the adsorptive anions will be identified as ETI for etidronate, ALE for alendronate, and RIS for risedronate.

B.1.2 Modeling

A density functional theory (DFT) based study of etidronic acid, alendronic acid, and risedronic acid, electronic structure was carried out to access details about the local reactivities and electrostatic potential of these molecules simulated in a water environment, to predict the behavior of the reactivity of these molecules, what can help in the determination of the most likely interactions of these with the titania surface, improving the comprehension of the results obtained experimentally (XPS and zeta potential). The application of the computational descriptors can elucidate the mechanisms of interaction between bisphosphonates and the substrate surface (LASCANE; OLIVEIRA; BATAGIN-NETO, 2020; ALVES et al., 2020; MANDú; BATAGIN-NETO, 2018; MAIA; VENTORIM; BATAGIN-NETO, 2019; PLáCIDO et al., 2020).

The structures were designed with the aid of the Gaussview computational package (DENNINGTON; KEITH; MILLAM, 2019). The obtained structures were then fully optimized in the density functional theory (DFT) framework using the B3LYP hybrid XC functional and 6-31G(d,p) polarized basis set (LEE; YANG; PARR, 1988; BECKE, 1993; STEPHEN et al., 1994; MYRSETH et al., 2002). To study the conditions of molecules in water, the polarizable continuum model (PCM) was employed (TOMASI; MENNUCCI; CAMMI, 2005).

Local reactions of molecules were evaluated via condensed-to-atoms Fukui indices (CAFIs), which can identify the molecular sites that are prone to interact with electrophilic

(f^-) and nucleophilic (f^+) agents (YANG; PARR, 1985; YANG; MORTIER, 1986). Despite their simplicity, these indices provide significant insights about the reactivity of molecules and polymers (LASCANE; OLIVEIRA; BATAGIN-NETO, 2020; ALVES et al., 2020; MANDú; BATAGIN-NETO, 2018; MAIA; VENTORIM; BATAGIN-NETO, 2019; PLáCIDO et al., 2020; LASCANE; OLIVEIRA; BATAGIN-NETO, 2020). The CAFIs are estimated from finite differences of electronic populations after insertion and removal of electrons to/from the systems. For instance, a system of interest **M** (with N electrons) after the insertion and removal of one electron produces the species $\mathbf{M}^-$ and $\mathbf{M}^+$, respectively (with N+1 and N-1 electrons), and the CAFIs are estimated by f_k^+ and f_k^- :

$$f_k^+ = q_k(N+1) - q_k(N) \tag{2}$$

$$f_k^- = q_k(N) - q_k(N-1) \tag{3}$$

In equations (1) and (2), q_k(N+1), q_k(N), and q_k(N-1) represent the electronic populations on the *k*-th atom in the species $\mathbf{M}^-$, **M**, and $\mathbf{M}^+$. Hirshfield's partition charge was used to obtain the electronic populations to avoid negative CAFI values (PROFT et al., 2002; ROY; HIRAO; PAL, 2000). The mapping of the molecular electrostatic potential (MEP) was obtained via CHelp partition charge scheme (CHIRLIAN; FRANCL, 1987). All the calculations were conducted with the aid of the Gaussian 16 computational package (FRISCH et al., 2016). Figure 37 presents the MODA plot of the theoretical methods applied in the work (KLEIN et al.,).

Figure 37 – MODA plot of the computational methods employed.

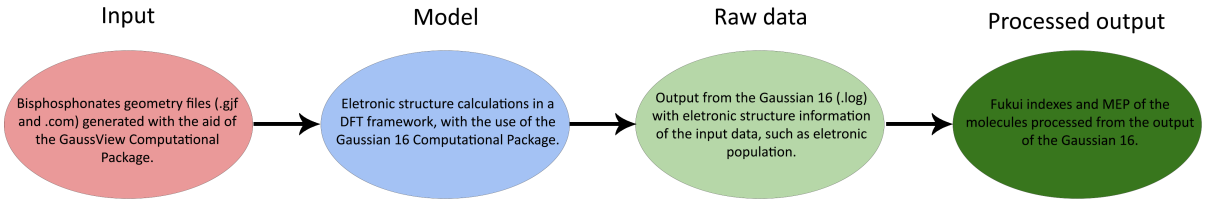

Source: Developed by the author

B.1.3 Sputter deposition

Titanium dioxide was sputter deposited on a silicon wafer and glass substrates as described in previous work (DIAS et al., 2020). Briefly, the deposition started after reaching a pressure of 10^{-5} hPa, then argon was added into the chamber. After 30 seconds of deposition, oxygen was slowly added. The total time of deposition was 900 s.

B.1.4 Layer preparation

Different samples were prepared by varying the time (2 and 24 hours) that titania adsorbents were immersed in BP adsorptive solutions, maintaining a concentration of 1 mM. High-performance liquid chromatography (HPLC) quality water was used as the solvent. After the complete dissolution of the BP salts, the substrate samples were immersed and left for 15 minutes, 2 hours, and 24 hours. After this, they were removed from the solution and rinsed in water for 15 minutes. All samples were gently blown using air applied with a hand bellow. A bulk sample of etidronic acid was prepared from a saturated solution in which HPLC quality water. The solution was dropped in a silicon wafer and left to dry in ambient conditions. After drying, the sample was gently washed using cold HPLC quality water. The sample was analyzed through XPS, and the C1s high-resolution spectrum is available in Figure 39.

B.1.5 Atomic force microscopy measurements (AFM)

Surface topography and roughness of samples immersed for 24 hours were analyzed in non-contact mode through the Park XE7 (from Park Systems, Santa Clara, CA, USA). A silicon cantilever PPP-NCHR from Park Systems Inc. was employed using a constant force of 42.0 N/m and a frequency of 330 kHz. Measurements were taken in the air at room temperature. Images of 1 × 1 μm^2 were taken applying a scan rate of 0.7 Hz. Gwyddion program (v. 2.55, from http://gwyddion.net/) was employed for post-treatment of the raw data. First, a step line correction was applied, then polynomial degree 5 was applied for aligning rows corresponding to one scan line each. Horizontal scars were corrected, and a few dust residuals were removed using the remove grain tool. Finally, the height scale bar was set from 0 to 2 nm and the image was displayed as a 3D view. Roughness (root mean square) was obtained using the function calculate statistical functions considering the whole image.

B.1.6 Contact angle measurements

Contact angle measurements were performed right after the drying procedures of the samples, in the case of BP/titania (immersed for 24 hours) following the preceding BP deposition process. Samples from sputter-deposited titania on glass slides were analyzed. The measurements were performed using the mobile surface analyzer – MSA from KRÜSS (Germany) – at room temperature. HPLC quality water was used as probe liquid, in which 2 μL of the liquid was automatically dropped on the surface. The water contact angle for each drop was recorded using the tangent method. Two distinct regions of each sample were analyzed, and the mean contact angle was calculated.

B.1.7 XPS characterization

XPS characterization of samples immersed for 15 minutes and 2 hours was carried out using a Kratos AXIS Ultra system with a monochromatized Al Kα X-ray source (energy hν=1486.6 eV). The base pressure of the analysis chamber was approximately 6×10^{-8} Pa. Spectra were acquired in the constant analyzer energy mode using pass energies of 160 eV and energy steps of 0.444 eV for survey spectra or, respectively, 20 eV using energy steps of 0.066 eV for detail scans. Spectrum fitting was performed using CasaXPS (v2.3.18, Casa Software Ltd). First, the binding energy scale of the spectra was aligned by centering the C1s signal of the hydrocarbon species at 285.0 eV. The signal area analyzed was set using a Shirley background. Peak components were adjusted with a Gaussian-Lorentzian line shape GL(30). The created areas were fitted using the Marquardt-Levenberg algorithm. Figure 38 presents the CHADA applied for XPS characterization (ROMANOS et al., 2019; CAVALCANTI et al., 2021).

Figure 38 – Characterization data (CHADA) documentation was applied for XPS measurements.

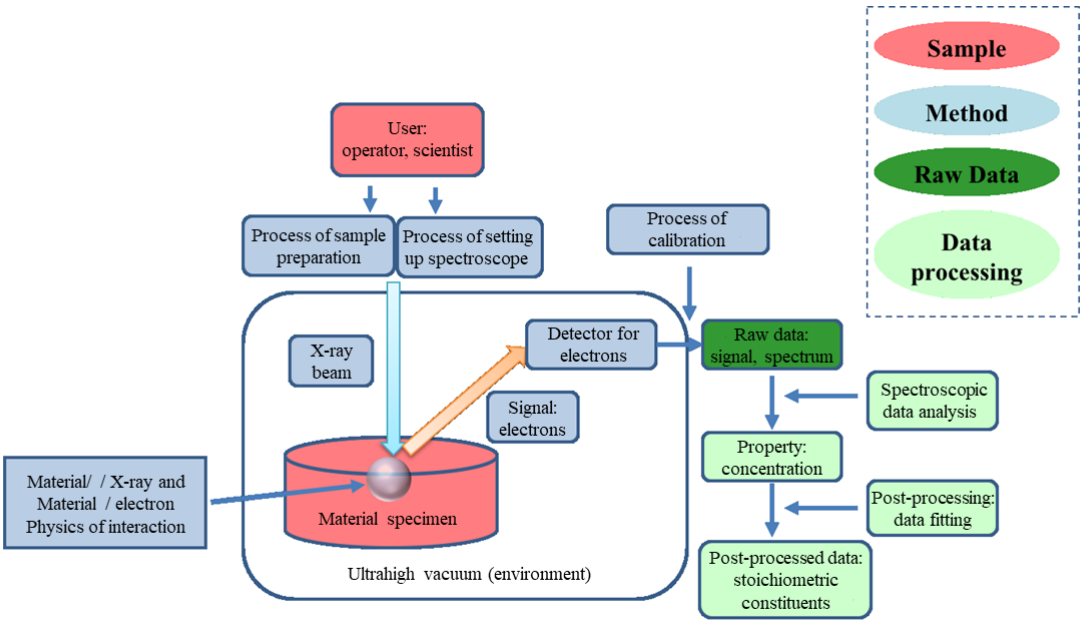

Source: Developed by the author

B.1.8 Zeta potential measurements

Zeta potential measurements were performed with different titania samples deposited on glass slides for 24 hours during immersion in BP solution. The values were recorded using the SurPASS™ 3 device from Anton Paar (Austria) at room temperature. The adjustable gap of the cell used was adjusted to 100 µm. The pH was regulated using a 0.05 M solution of

potassium hydroxide and 0.05 M solution of hydrochloric acid, respectively. The pH step was set to 0.5 for titania and 0.75 for BP/titania samples on a pH scale of 8 to 4 and measured with a pH meter sensor included on the equipment. The error bars were estimated based on three distinct measurements on three different titania samples.

B.2 Results

The computational simulations employed in supplementary information used the same parameters (B3LYP exchange XC functional and 6-31G(d,p) polarizable basis set) presented in the main paper.

Figure 39 indicates the Condensed Atoms Fukui Indexes (CAFIs) and the Map of Electrostatic Potential (MEP) of the structure of the bisphosphonic acid simulated in a vacuum. For etidronic acid (ETI), a strong affinity for nucleophilic attacks in the phosphonate groups, mainly in the –OH groups, indicating that the molecule can go through deprotonations on these sites. The regions more prone to interact with electrophilic agents are the –O group present in the phosphonate and the –OH group at the hydrocarbon chain. The MEP of the molecule shows regions of strong negative electrostatic potential around the oxygen atoms, while the positive electrostatic potential is more intense in the hydrogen atoms.

Figure 39 – Structure, f^+, f^- and the MEP of all the structures simulated in vacuum.

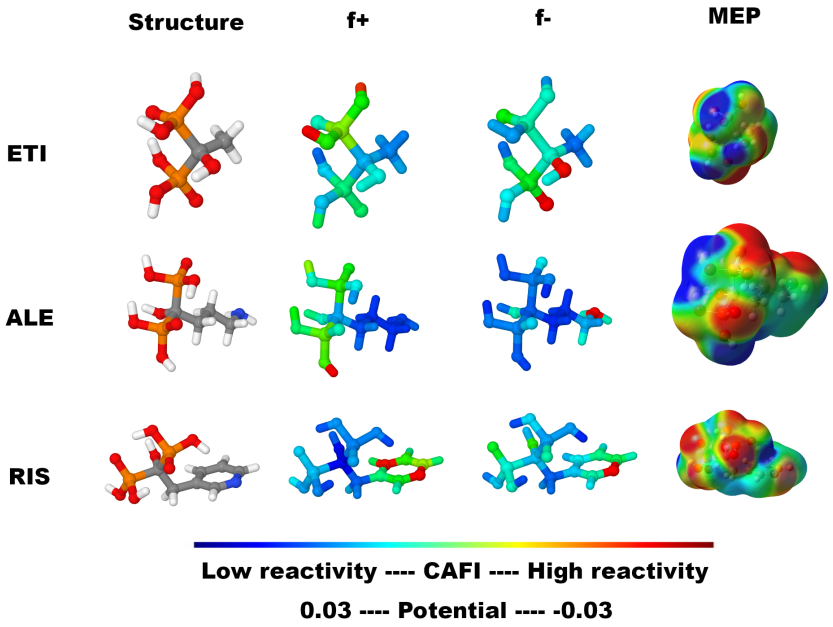

Source: Developed by the author

Figure 40 displays the computational results for bisphosphonates simulated in an aqueous environment. For etidronic acid (ETI), a strong reactivity for nucleophilic attacks in the phosphonate is observed, especially in the –OH groups. The reactivity for electrophilic

attacks is more intense in the –O atoms of the phosphonate groups and the –OH group of the hydrocarbon chain, similar to the structure simulated in a vacuum. The MEP displays regions of strong negative electrostatic potential around the oxygen molecules, while the negative electrostatic potential is more intense in the hydrogen atoms. As observed, regions of negative and positive electrostatic potential are more intense in the structure simulated in an aqueous medium than in a vacuum.

Figure 40 – Structure, f^+, f^- and the MEP of all the structures simulated in aqueous medium.

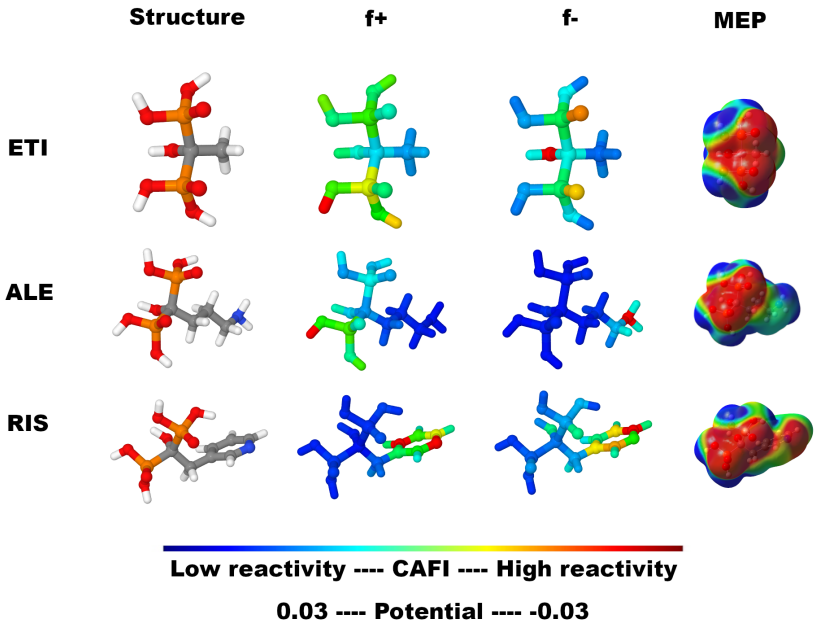

Source: Developed by the author

Alendronic acid (ALE) shows a strong affinity for nucleophilic attacks in the phosphonic acid, principally in the –OH groups. The reactivity for electrophilic attacks is focused on the nitrogen atom. The MEP shows regions of negative electrostatic potential around the oxygen atoms and regions of positive electrostatic potential around the hydrogen atoms and the amino group (also due to the hydrogens). The simulation of the structure in an aqueous medium changed the map of electrostatic potential in comparison to the simulation in a vacuum. The nitrogen atom presented a region of positive electrostatic potential in an aqueous medium, while also presented a region of negative electrostatic potential in a vacuum.

Risedronic acid (RIS) displays a reactivity for nucleophilic attacks almost identical to the one presented for the molecule in a vacuum; however, the whole reactivity is mainly focused on the nitrogen atom of the pyridine ring and in its para position. For electrophilic attacks, the reactivity is focused on the pyridine ring and remains mostly around the carbon atom next to the nitrogen atom. The MEP shows regions of negative electrostatic potential around the nitrogen and oxygen atoms, while the regions of positive electrostatic potential are found around the hydrogen atoms, such as the structure simulated in a vacuum.

B.3 X-ray photoelectron spectroscopy

Positions of C1s high-resolution spectra of bulk etidronate were obtained based on the fitting proposed by Gao and Sherwood and is presented in Figure 41 (GAO; SHERWOOD, 2013). There are four peaks, adventitious carbon at 285.0, 287.6, and 288.8 eV (DIAS et al., 2020). Etidronate moiety was characterized by a peak at 286.1 eV (GAO; SHERWOOD, 2013).

Figure 41 – C 1s high-resolution spectra of bulk etidronate.

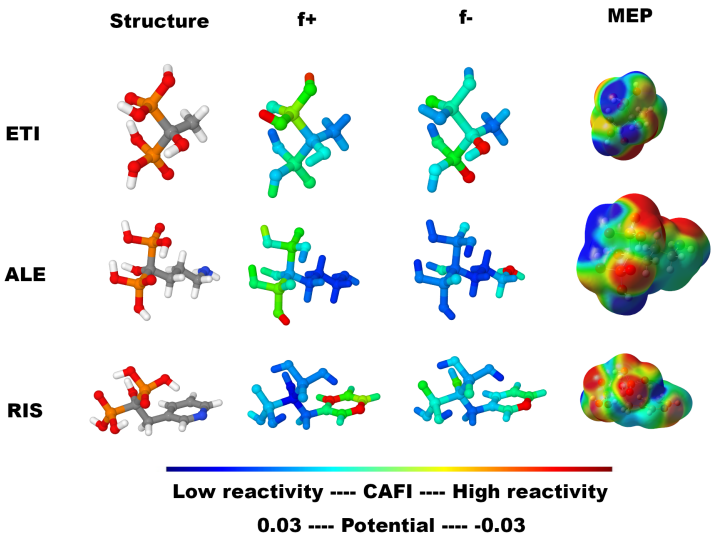

Source: Developed by the author

Information regarding the FWHM of the fitted contributions is displayed in Table 20, the values are displayed starting from the peaks at lower energy.

Table 20 – FWHM for the contributions of XPS analyses.

	C1s signal					O1s signal			N1s signal	
	FWHM (eV)					FWHM (eV)			FWHM (eV)	
Bulk etidronate	1.4	1.4	1.4	1.4						
TiO_2	1.2	1.2	1.2	1.2		1.1	1.6		2.6	
TiO_2/ETI 1mM 2h	1.0	1.0	1.0	1.0	1.0	1.1	1.6	1.6	2.7	
TiO_2/ALE 1mM 2h	1.2	1.2	1.2	1.2	1.2	1.1	1.5	1.5	1.7	1.7
TiO_2/RIS 1mM 2h	1.3	1.3	1.3	1.3	1.3	1.1	1.5	1.5	1.5	1.5

APPENDIX C – *Supplementary information Chapter 5*

Structural characterization through X-ray diffraction is presented in Figure 42. The results show the anatase and rutile was successfully prepared. The most intense peaks are (101) and (110) for anatase and rutile, respectively.

Figure 42 – XRD of TiO_2 particles.

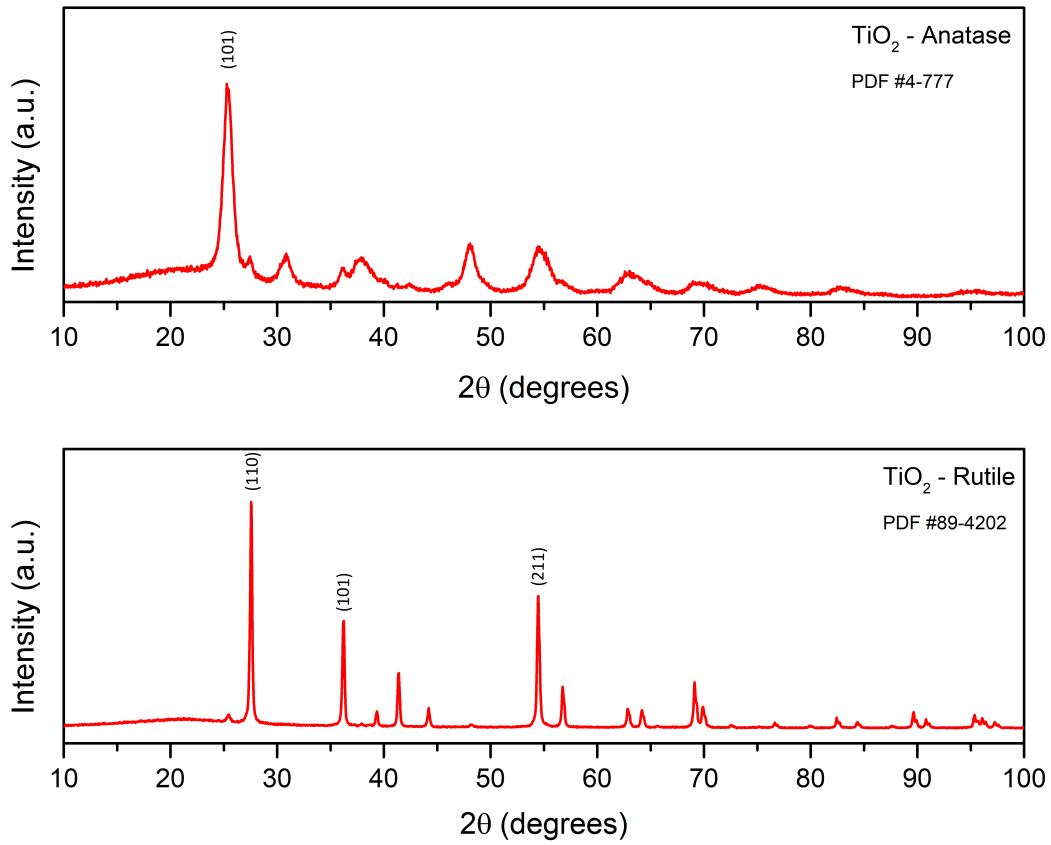

Source: Developed by the author

Figure 43 – Confocal images of prepared samples.

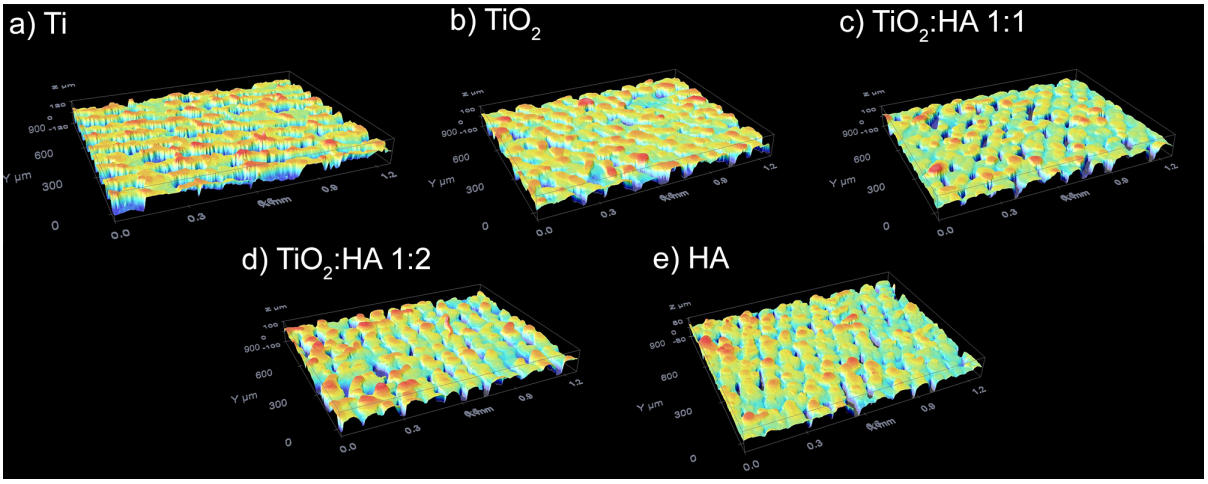

Source: Developed by the author

Figure 44 – Map of chemical composition of TiO_2 film.

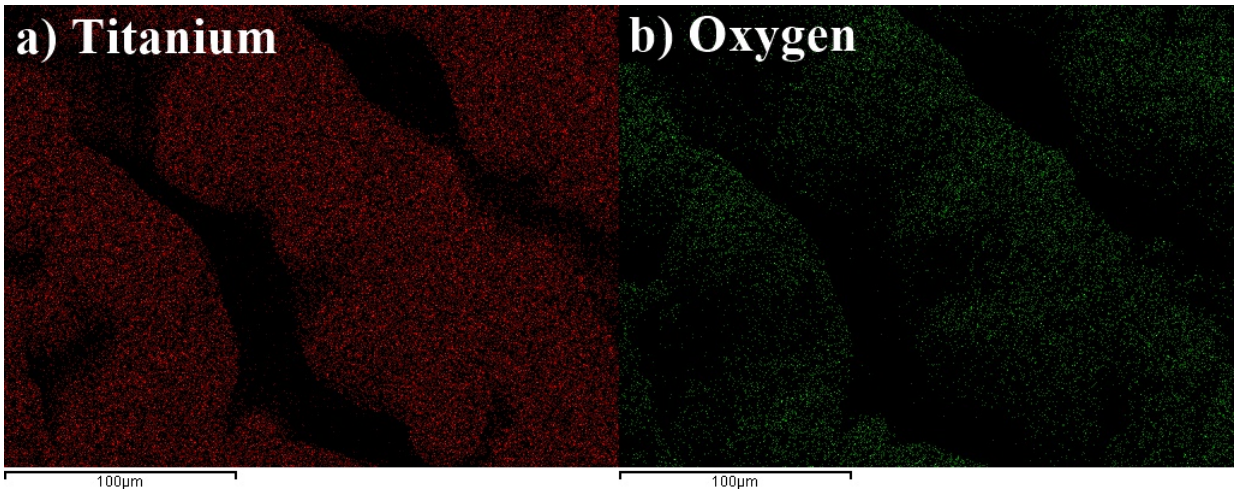

Source: Developed by the author

Table 21 – Water contact angle (WCA) for samples functionalized with 0.2 mM solutions

Sample	WCA (°)
TiO_2/ETI	17.2 ± 0.7
TiO_2/ALE	0*
TiO_2/RIS	0*
TiO_2:HA 1:1/ETI	0*
TiO_2:HA 1:1/ALE	0*
TiO_2:HA 1:1/RIS	0*
TiO_2:HA 1:2/ETI	0*
TiO_2:HA 1:2/ALE	0*
TiO_2:HA 1:2/RIS	0*
HA/ETI	0*
HA/ALE	0*
HA/RIS	0*

*0 means that the water drop was completely spread on surface.

Source: Developed by the author.

Figure 45 – Map of chemical composition of TiO_2:HA 1:1 film.

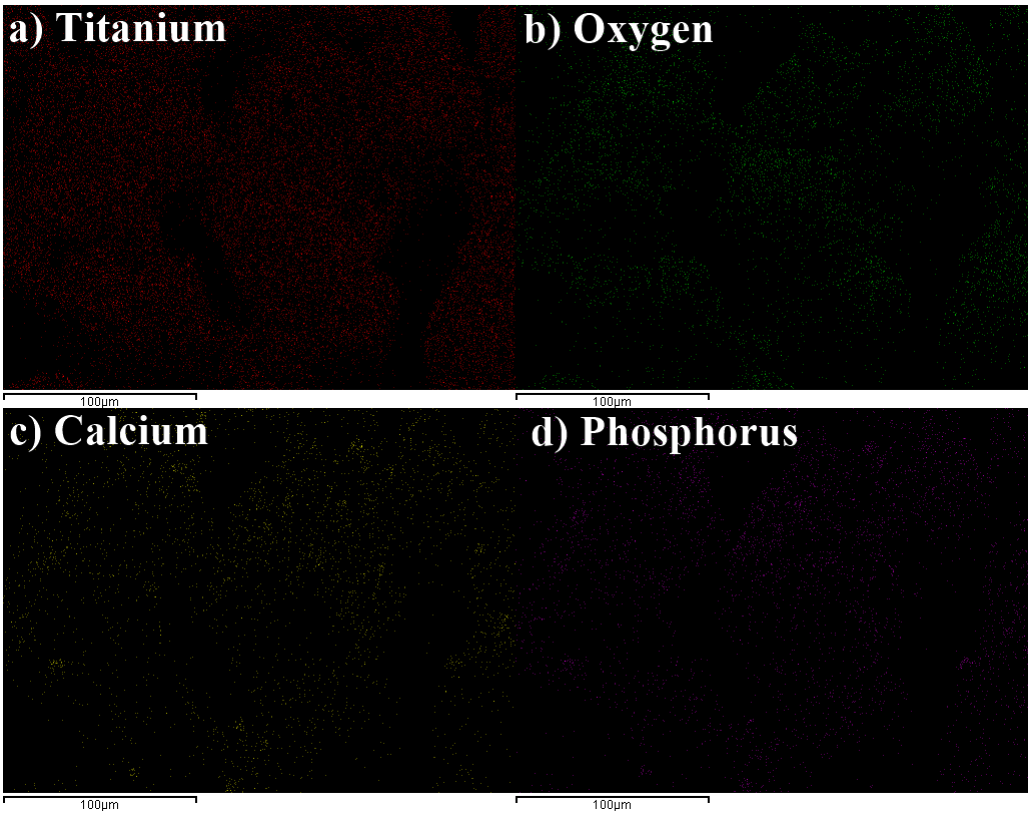

Source: Developed by the author

Figure 46 – Map of chemical composition of TiO_2:HA 1:2 film.

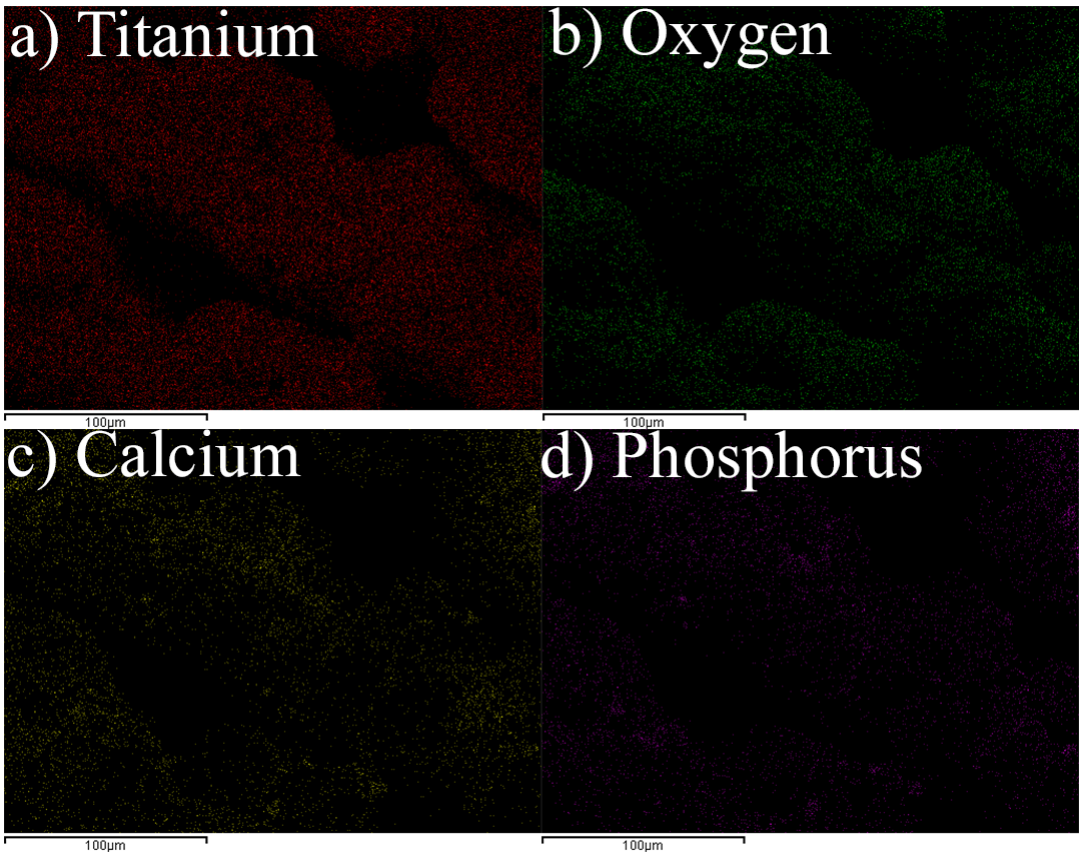

Source: Developed by the author

Figure 47 – Map of chemical composition of HA film.

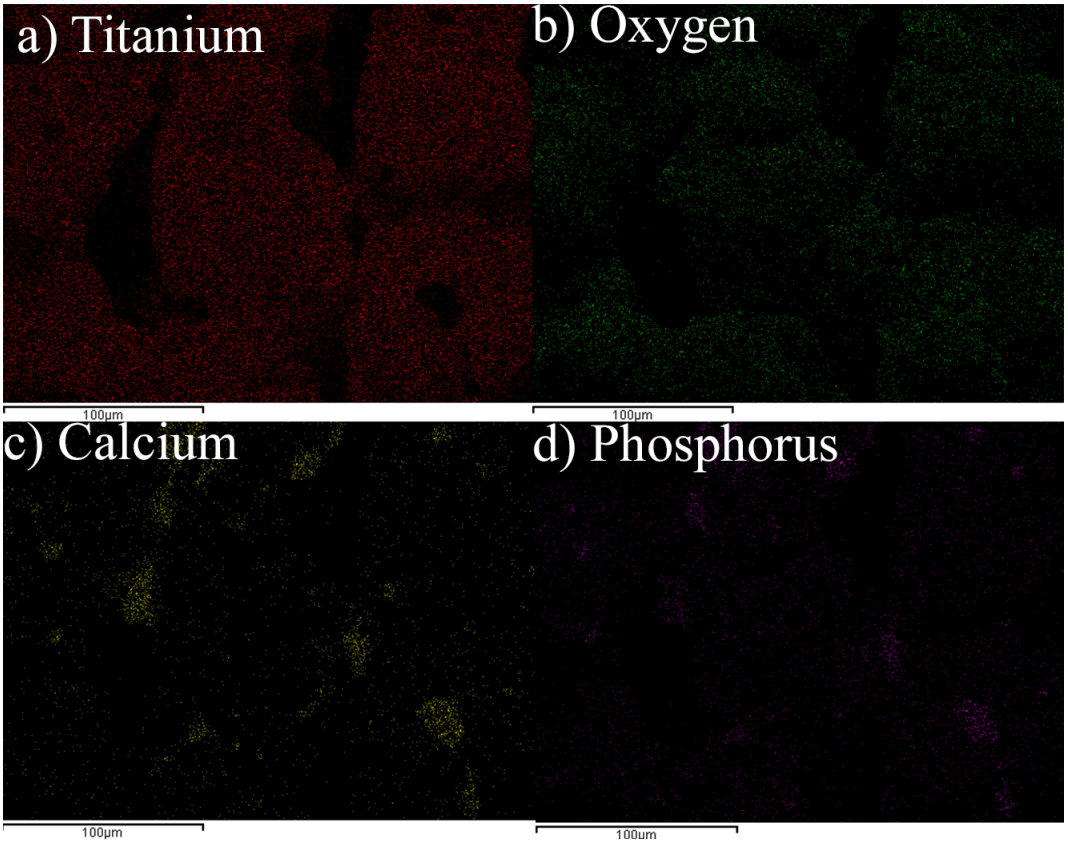

Source: Developed by the author

Figure 48 – N 1s high-resolution spectra of samples containing nitrogen.

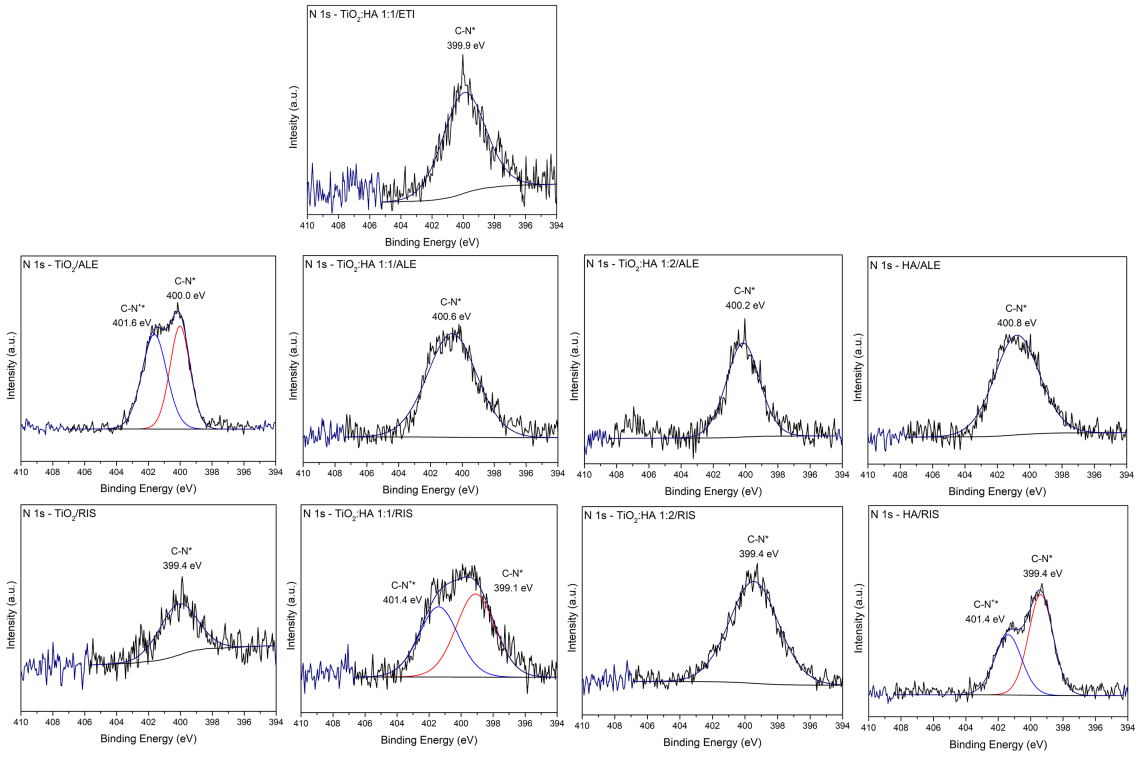

Source: Developed by the author